Doctoral Dissertation

High-Throughput Experimentation and Catalyst Informatics for Oxidative Coupling of Methane

Thanh Nhat Nguyen

Supervisor: Assoc. Prof. Toshiaki Taniike

Graduate School of Advanced Science and Technology

Japan Advanced Institute of Science and Technology

September 2020

Referee-in-chief: Associate Professor Toshiaki Taniike
Japan Advanced Institute of Science and Technology

Referees: Associate Professor Yuki Nagao
Japan Advanced Institute of Science and Technology

Associate Professor Shun Nishimura
Japan Advanced Institute of Science and Technology

Associate Professor Dam Hieu Chi
Japan Advanced Institute of Science and Technology

Associate Professor Keisuke Takahashi
Hokkaido University

High-Throughput Experimentation and Catalyst Informatics

for Oxidative Coupling of Methane

Thanh Nhat Nguyen

1720408

Materials informatics (MI) is one rising area, which applies data-oriented approaches to the research and development of materials science. One of fundamental requirements for MI is the presence of a proper dataset in terms of consistency, distribution, and size. Once such a dataset is prepared, an appropriate learning method is selected from the toolbox. While enormous materials data have been accumulated in literature, they suffer from an insufficient scale, non-uniformity, and anthropogenic biases towards good data with the burial of poor data. Moreover, materials properties such as catalyst performance are highly sensitive to process conditions, while individual research groups have commonly employed their own conditions. In order to overcome the problem of the data scarcity in MI, high-throughput experimentation is considered to be the most promising and effective approach. In this thesis, I attempted to establish complete high-throughput experimentation for the generation of a proper dataset, and implement catalyst informatics to extract knowledge from the obtained dataset. The concept was demonstrated by taking oxidative coupling of methane (OCM) reaction as a case study, which is a long researched reaction toward industrialization.

In **Chapter 2**, a high-throughput screening instrument was successfully developed for automatic performance evaluation of 20 catalysts at a series of predefined conditions in a fixed-bed configuration. The catalytic test was done in steady states at 900 to 850, 800, 775, 750, and 700 °C. At each temperature, the total flow volume, the CH_4/O_2 ratio, and the Ar concentration were stepwise varied, leading to 216 conditions per catalysts and 4320 observations for 20 catalysts in a single automated operation. By only 3 operations, 59 catalysts of a Mn-Na_2WO_4/SiO_2 type were successfully evaluated in OCM, which enabled knowledge extraction using common visualization tools and machine learning techniques. It was found that the OCM reaction is generally sensitive to the process conditions, and catalyst design has a great impact on the process dependence. In particular, the modification of Si-based support affects the performance of Mn-Na_2WO_4 in terms of the low-temperature activation of CH_4 and the selectivity tolerance against high O_2 concentration.

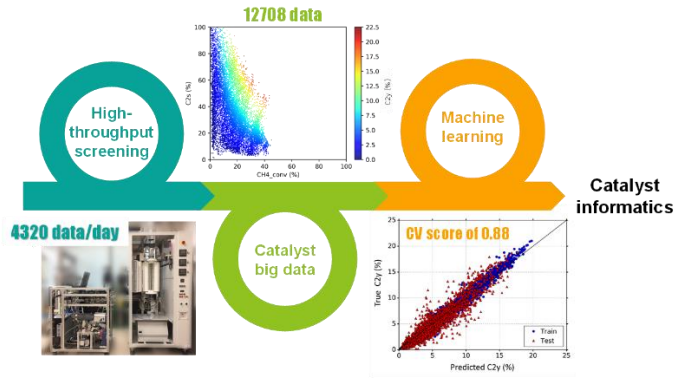

Figure 1. Concept of catalyst informatics achieved in this thesis.

In order to explore the origin of the low-temperature CH_4 activation, in **Chapter 3**, a series of catalysts were prepared by depositing the Mn–Na–W active phase on various Si-based supports which differed in the pore size, the structure, and the amount of foreign elements (Al, Ti). The OCM performance of these catalysts was acquired on the developed HTS instrument

under various reaction conditions. It was found that high-silica supports were good supports in general, while mesoporous silica supports appeared to be superior at low temperature specifically. From the characterization results, it was elucidated that high-silica supports are advantageous in forming the α-cristobalite phase, which is known to stabilize tetrahedral WO_4^{2-} and Mn_2O_3 active species. The mesoporous silica offered the largest accessible surface area to improve the dispersion of the active phase.

In **Chapter 4**, I aim to discover new catalysts by means of random sampling from a vast materials space, HTS, and data analysis. 300 M1–M2–M3/support catalysts were prepared and evaluated, where M1, M2, M3, and support were randomly selected from a given library. By statistical analysis, I successfully identified individual elements and their binary combinations which are positive for the OCM performance. Machine learning was employed to generalize the effective catalytic system for OCM. The results not only rediscovered known catalysts obtained in the past three decades, but also newly discovered novel combinations that have never been explored so far.

Based on all of these results, I successfully demonstrated the implementation and power of the MI in the research and development of OCM catalysts, where the presence of high-throughput experimentation was truly indispensable for obtaining a proper dataset.

Keywords: High-throughput experimentation, Catalysts informatics, Oxidative coupling of methane, Machine learning, Combination effect

Preface

The present thesis is submitted for the Degree of Doctor of Philosophy at Japan Advanced Institute of Science and Technology, Japan. The thesis is consolidation of results of the research work on the topic "High-Throughput Experimentation and Catalyst Informatics for Oxidative Coupling of Methane" under the supervision of Assoc. Prof. Toshiaki Taniike during October 2017– September 2020 at Graduate School of Advanced Science and Technology, Japan Advanced Institute of Science and Technology.

Chapter 1 describes a general introduction and the purpose of this thesis. **Chapter 2** focuses on the development of high-throughput screening instrument and its demonstrative application to catalyst informatics in oxidative coupling of methane. **Chapter 3** pursues the origin of a low-temperature activation ability of Mn-Na-W catalysts supported on different types of silica materials. **Chapter 4** reports a study of combination effects in the design of OCM catalysts on the basis of catalyst informatics. **Chapter 5** describes the general summary and conclusion of this thesis. To the best of my knowledge, the work is original and no part of this thesis has been plagiarized.

Thanh Nhat Nguyen

Graduate School of Advanced Science and Technology

Japan Advanced Institute of Science and Technology

April 2020

Acknowledgements

First of all, I would like to express the deepest sense of gratitude to my supervisor Assoc. Prof. Toshiaki Taniike, Graduate School of Advanced Science and Technology, Japan Advanced Institute of Science and Technology for his continuous support, and enlightening suggestions throughout my Ph.D course. I am thankful to him for his never ending patience, motivation and immense knowledge.

I would also take an opportunity to thank Senior Lecturer Patchanee Chammingkwan, Asst. Prof. Ashutosh Thakur, Asst. Prof. Toru Wada for thier valuable inputs, cooperation and stimulating discussions.

I am also heartily grateful to all other members of Taniike laboratory for their valuable suggestions, cooperation and support.

I am also thankful to Assoc. Prof. Keisuke Takahashi in Hokkaido University, for his valuable suggestions and continuous support related to informatics. My sincere thankfulness is extended to those people who work for a catalysts informatics project.

I would like to thank members of my review committee, Assoc. Prof Yuki Nagao (JAIST), Assoc. Prof. Shun Nishimura (JAIST), Assoc. Prof. Dam Hieu Chi (JAIST), and Assoc. Prof. Keisuke Takahashi (Hokkaido University) for their helpful comments and valuable suggestions.

I would like to thank my second supervisor, Assoc. Prof. Kazuaki Matsumura, and my advisor for minor research, Prof Tatsuo Kaneko for the time they spent for me.

I would like to thank my parents for always encouraging me and supporting my ambitions. And last but not the least; I am particularly grateful to my wife Tran Phuong Nhat Thuy for her unconditional supports in all aspects of my life.

Table of contents

Chapter 1

General introduction

1.1. Material informatics

1.1.1. Overview of material informatics

The evolution in the field of materials science is comparable to the way how sciences and technologies have been developed. Thousand years ago evidenced the growth of purely empirical science, as clearly observed by the metallurgical evolution throughout three periods of "age" (stone, bronze, iron) [1]. After that, the 17th century witnessed the paradigm of theoretical models with the finding out numerous "laws" and mathematical equations (such as laws of thermodynamics in materials science). But in some problems, the theoretical models are not practical or infeasible owing to the difficulty in measurements or no analytical solutions. The last few previous decades saw the rise of computational science, which allowed the simulations of complex real-world phenomena. For example, density functional theory (DFT) and molecular dynamics (MD) simulations are perhaps two greatest progresses which were brought in material science in the third period. Nowadays, the three paradigms of science, which are based on experiments, theories, and computations/simulations, are commonly used in all scientific domains [2,3]. In the last decade, the significant increase in the amount of data being generated by has prompted the emergence of the next paradigm of science, i.e. data science (Figure 1.1) .

Data science has been has been considered as the "fourth paradigm" of science [1]. Machine learning has been continuously studied since the middle of the previous century and used in numerous applications such as data mining, image recognition and, materials discovery [2,3]. The power of machine learning is to mimic the human cognitive functions in decision making [2]. When a new situation is encountered, cognitive systems (including humans) have a tendency to make a decision based on

past similar encounters. Even completely new situations occur, human mind still makes the correct decision based on assumptions and extrapolation of the past experiences [4]. Machine learning aims to mimic this human sense by training algorithms on "prior experiences", made of past data, and then leveraged to make predictions for "future events" such as the performance of unknown materials for a specific purpose. Such application of machine learning to improve the understanding and discovery of materials in materials science is called materials informatics.

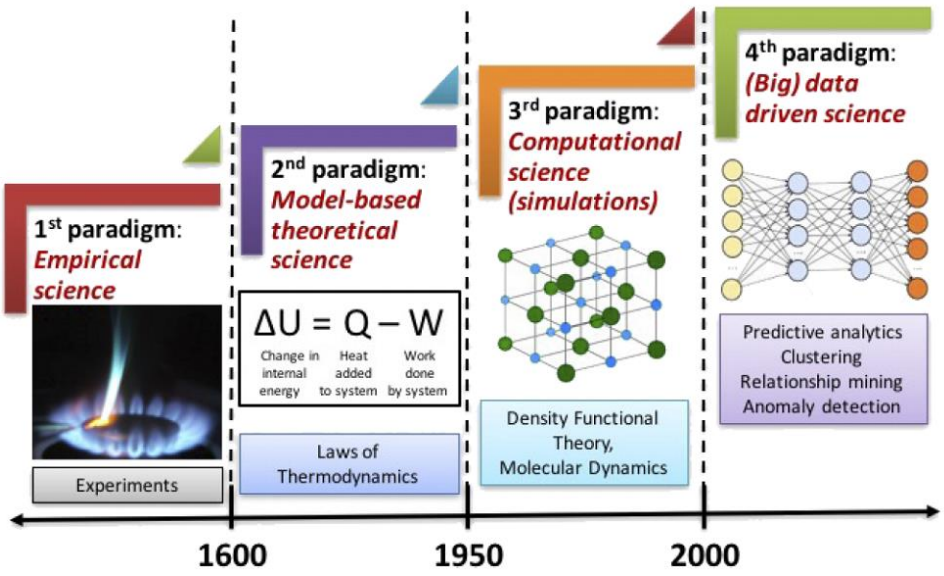

Figure 1.1. The four paradigms of science: empirical, theoretical, computational, and data-driven science. Reproduced from Ref. [1].

A number of algorithms have been applied to create intuition in machines [5,6]. Artificial neural nets and random forest are well-known algorithms, which were developed for modeling the brain functions of animals or handwritten numbers classifications [7]. Both of these algorithms, along with many more not described here, were developed for different applications at different stages of computer technology, and many have since been adopted for application in the materials sciences.

The dawn of materials informatics plausibly came from atomistic calculations. The atomistic calculations have been frequently used in materials science [8]. These calculations describe properties of a solid on the basis of physical interactions among atoms in the solid. In general, atomistic calculation techniques have allowed them to calculate a wide range of materials problems [9]. More recently, the burgeoning of computational infrastructures and algorithms enables ‘‘high-throughput” calculations, which dramatically speed up the prediction up to thousands of materials within single studies [10]. It must be noted that the computational cost intrinsically limits the scale of problems feasible (i.e. the space and time scales for calculations). Even a few calculations containing trillions of atoms or spanning over a millisecond have been reported in some reports; they are not such easy to achieve and only possible with simplified models for the interatomic interactions [11,12]. Besides, more precise prediction generally requires further greater computational cost. One strategy to reduce the computational costs is to predict the properties of new materials based on the previous calculations using data-driven approaches. As stated in the last paragraph, the rise of data-driven technologies such as machine learning may enable to predict properties of new materials from the previously obtained data. Such the research direction gradually became prevalent, and eventually it was called “materials informatics”. The ultimate target of materials informatics is to extract knowledge from the datasets of materials properties. This knowledge can take several views. More specifically, the knowledge could be a predictive model for a complex material property based on simple and easier-to-compute properties of the materials. Or, it could be a small set of previously-unknown factors that help explain materials behaviors. Of course, these could be also goals of conventional scientific practice. The advantage of materials informatics is that creating models and learning descriptors can be done

quickly and sometimes even automatically. Nowadays, much of efforts have been devoted to material informatics, which may be attributed to the Materials Genome Initiative (MGI), a trigger of this paradigm shift towards computational solutions for materials discovery [1]. The ultimate goal of the MGI is to accelerate the speed of materials discovery by combining computational tools, experimental tools, and standardized materials data cataloging [13]. In doing so, databases of experimentally and computationally determined materials properties are leveraged by machine learning algorithms to predict new materials composition with targeted properties. Following the success of MGI, many databases for storage data generated from first-principles calculations are opened for readily using such as the Open Quantum Materials Database (OQMD) [14], Automatic Flow for Materials Discovery (AFLOW) and the Novel Materials Discovery repository (NoMad) [15], and [16]. Recent works have used data-driven approaches for predicting the physical properties of solid, inorganic materials, organic materials [10,17], and Metal Oxide Frameworks (MOFs) [18,19].

1.1.2. Implementation of materials informatics

Generally, implementation of material informatics required requires 3 three fundamental ingredients: A set of target variables (output), a set of materials features (input), and a machine learning algorithm to establish a mapping between the two sets [4]. This architecture of the implementation for materials informatics is shown in Figure 1.2

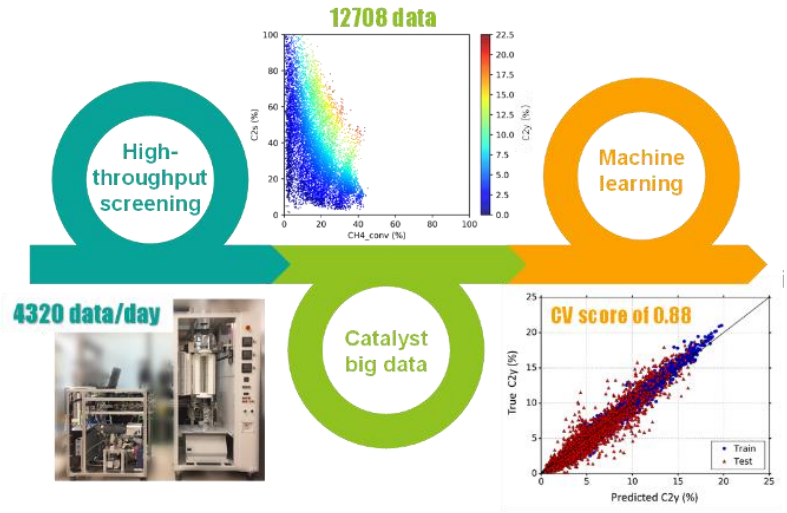

Figure 1.2. Implementation of materials informatics.

The target variable in this example is the measured experimental data. Connection exists between this measured data and the corresponding materials features, such that some features cause positive changes in the measured data and other features cause negative changes. If the amount of data becomes sufficiently large, the connection between the target variable and materials features become challenging for human mind to understand. In such cases, machine learning is powerful to solve this task. The machine learning can then be used to predict the target variable of new materials, or extract knowledge related to the system of materials.

The target variables are usually properties of the materials. The property of interest varies depending on individual applications, which, for example, includes materials hardness, conductivity, band gap, catalytic performance, etc. [20,21]. The prerequisite for the target variable is the presence of a proper dataset in terms of consistency, distribution, and size [22]. The target variables could be obtained either from simulation or experimental data. For simulations/computations, the data are calculated for a variety of materials to create a training dataset, and machine learning

is used to learn from these calculation results, and then drastically speed up materials discovery by bypassing the computational cost of the calculations [23,24]. Through the acquisition of datasets by computations are fast, low cost, and consistent, but these lack of information of processes and their conditions, thus applicable only in simple cases, e.g. band gap of perfectly crystalline materials. For experiments, even the datasets are the best fit to a practical target as it contains material properties under process conditions. However, acquiring a sufficiently large dataset in a short time span is difficult, and using conventional experimental techniques is impractical. For this purpose, high-throughput experimentation techniques can dramatically accelerate the speed of dataset creation [25-27].

The second component of materials informatics is the set of materials features, called descriptors. These features could be any information that relate to the materials. Prevalent features are enumerated by the materials composition or elemental properties, such as electronegativity or atomic radius. These features are easily available and therefore most frequently used in terms of the ease of usage to estimate materials behaviors. Nevertheless, they are usually not good features as they are not directly correlated with fundamental phenomena within the materials. For example, the atomic radius may be a valid predictor to estimate whether a certain phase will be formed or not, since it contributes to the geometry of the material [28]. However, the atomic radius alone would not make accurate predictor, and must be combined with other features in order to achieve any degree of accuracy. In some case, the use of a single feature may be enough for prediction in a simple system such as mono-metallic materials. However, it is not sufficient for the prediction of binary or tertiary metallic systems as there is an interaction among elements. Thus, researchers have developed so-called synthetic descriptors for describing the interaction between elements. For example, Meredig et

al. proposed the weighted average or the maximum difference of atomic masses or electronegativity values of elements present in the system. In some literature, more complex descriptors like the skewedness and kurtosis of *d*-bands were used [29]. More complex operations, such as "the absolute values of sums of differences", have also been proposed [30]. Materials behaviors do not only depend on materials themselves but also depend on the process conditions. In such cases, information related to materials synthesis such as the type of precursors or the preparation methods should be included as features [31]. For some applications, such process-related features such as the pH of a particular environment or a reaction temperature were included [32].

In addition, materials features could be obtained by computation methods, for example, density functional theoretical calculations for adsorption and activation energies, bond distances, molecular geometries, etc. [33,34]. This type of descriptors can be used to provide extremely accurate chemical information as long as models employed in the computations are sufficiently realistic (this requisite is not trivial for solid materials) [4]. Broad descriptors are better for general screening or materials discovery endeavors, while fine descriptors are best suited for high-accuracy understanding of chemical phenomena in a narrow materials space [4]. Since the subject of this thesis is materials, discovery, fine descriptors will not be covered in depth here.

The third component in the implement in material informatics is the machine learning algorithm. There are so many algorithms suited for specific situations; however, there is no such algorithm that always gives the best results [35]. Rather, the performance of machine learning depends on the data structure or the number of descriptors [55]. Therefore, to determine which algorithm has the best performance, many algorithms should be applied and compared for a given dataset. There are,

however, heuristics, which can narrow the range of algorithms considered for an application. Artificial neural networks (ANNs) are frequently used for a wide range of applications, but typically require huge datasets [36]. ANN requires at least 10000 data points, which are usually infeasible in material informatics [22]. Rather, other machine learning methods such as decision tree, random forest and support vector machine are more prevalent till now [37].

1.2. Machine learning

Machine learning has recently received a lot of interests due to its ability to predict materials properties from materials data. There are two categories of machine learning: supervised and unsupervised learning. Unsupervised machine learning algorithms classify the data based on similarity of features. These unsupervised algorithms need a set of materials features in order to perform classification. Unsupervised algorithms are typically utilized in classification (clustering) problems, in which the target is to associate a particular material with a class of materials. There are several unsupervised machine learning algorithms, like k-means clustering, Gaussian mixtures model, and principal component analysis (PCA).

On the other hand, supervised machine learning algorithms could correlate a feature set with materials labels (provided) with the ultimate target of correctly predicting the labels from the feature set. The data features could be any properties that describe a material system, e.g. material compositions, synthesis methods, morphology, or other factors. Materials labels are the conclusion obtained through expert analysis or from the measurements or calculations. Supervised machine learning algorithms are sub-categorized into regression and classification algorithms. Regression algorithms are used to predict continuous variables, while classification is used to assign a category

to each material. The classification algorithms generally work similarly to the unsupervised algorithms. However, the main difference is that supervised classification algorithms have access to the true class labels of materials during the training step, while unsupervised algorithms automatically generate their class labels based on feature similarity. Thus, it is natural that supervised algorithms tend to have better classification accuracy since it adjusts the model to maximize the accuracy of the train set. However, due to the adjustment to the train data, supervised classification also suffers from bias and human error through the misclassification.

Due to the vast number of machine learning algorithms available, detailed explanations will be given only for decision tree and random forest algorithms, which are used in my research. Other, there are many algorithms, which include K-means clustering, hierarchal clustering, and density-based spatial clustering, kernel ridge regression (KRR), and support vector machines (SVM), LASSO, ridge regression.

Random forest and decision tree

The random forest algorithm is a method of supervised machine learning, which was proposed by Tin Kam Ho [7]. This algorithm is based on the decision tree algorithm, which has been known as a very popular classification technique. However, decision tree is suffered from training bias and the model became easily over-learning. In order to avoid this, random forest includes many decision trees and each tree has its own bias, and vote all the tree results. By referring to the results of many trees, the bias problem of decision tree is removed in random forest.

Decision tree is the basic unit of random forest. Decision tree is established from a dataset using a process so-called binary recursive splitting, where a split occurs on a particular feature at a specified value. Each individual location on the decision tree is

called a node, and nodes that do not split are called leaves (Figure 1.3). At the beginning, decision tree selects a feature among all the available features that is best to split at this position by using information entropy or Gini index. However, the exact implementation depends on the variable is discrete (typically in classification problems) or continuous (in regression problems).

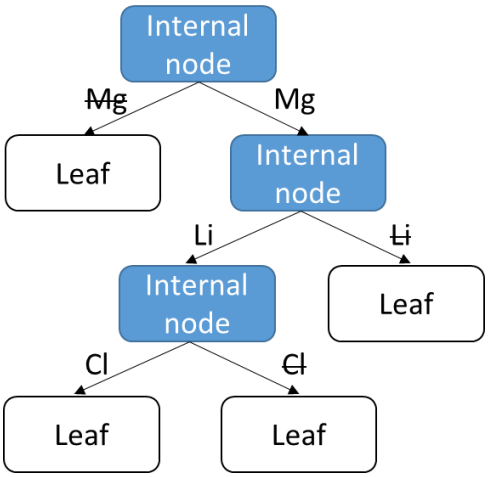

Figure 1.3. A basic structure of decision tree.

For discrete variable, the information entropy of a feature is calculated as: $H(X) = -\sum_{i=1}^{n} P(x_i)\log_2 P(x_i)$, where H(X) is the entropy of feature X, n is the sample number described by feature X, $P(x_i)$ is the probability mass function of x_i, and x_i is the individual feature value for sample i. To select the best feature, the information gain is calculated as: $IG(X) = H(X) - \sum_{i=1}^{n} H(X|\alpha)$, where IG is the information gain of feature X, n is number of categories in feature X, and $H(X|\alpha_i)$ is the information entropy when feature X is used and split along the i^{th} attribute of a. From the equation, feature where obtained maximized information gain is selected to split. In the case of continuous variable, the information entropy along the continuous set of value is calculated by: $H(X) = -\int P(x)\ln(P(x))dx$, where H(X) is the information entropy, x is an individual feature, and P(X) is the probability function for feature x. However,

calculating the information gain for continuous variable is computationally complex unlike discrete variable, because there are infinite split locations, rather than the finite "bins" or categories encountered in the discrete case. To deal with this problem, extremely randomized trees (ERT) algorithm is often utilized to create a set number of equally spaced split locations and calculate the information gain for only these discrete locations.

Next, stopping criteria needs to be consider for build a decision tree. This criteria determines at what point the tree terminates the splitting process. There are several approaches for stopping criteria. First, it is possible to building a full tree, when all leaves node are contain a single sample (totally pure), however, this approach often leads to significant over fitting for the decision tree, since machine memory the connection between features and target variable rather than learning from the trends. Another approach is the threshold tree, which uses a residual sum of squares (RSS) approach to optimize the tree. The RSS, calculated as equation $\sum_{j=1}^{j}\sum_{i\in R_j}(y_i-\hat{y}_i)^2$, is the sum of the differences in each leaf node between the average value and each individual sample value. In the case of building full decision tree, RSS equal to 0, since all leaves nodes are pure so the average value would be the value of the sample. In this approach, a threshold RSS is established, and the tree is constructed until that threshold is reached. This approach generally performs better than the full tree, but threshold have to be chosen carefully to prevent over fitting or under fitting. The third approach (called cost complexity pruning) is frequently used to escape from the need of threshold optimization. This approach initially build a full tree and then systematic evaluate the splitting from the bottom up. Split which do not show the improvement of the accuracy of predictions are pruned. This approach could significantly avoid the over fitting.

All of the implementations above are referred to as a top-down, greedy approach. In other words, a decision tree algorithm does not search for a global optimum; rather, the algorithm searches for the best binary split at each node (local optimum), and uses the collection of local optima to make predictions. This decision tree can suffer dramatically from high variance. Small variation in the training set can result in the large variation in the tree architecture, and consequently, significantly varies in the model predictions. Hence, the decision tree algorithm might not be a strong predictor, but the creation of many decision trees, making prediction from reviewing many decision trees leading to more accurate prediction and robust models. This is the philosophy of random forest algorithm, which make the final predictions from reviewing many decision trees. The idea of random forest is shown in Figure 1.4, where each decision tree have a different results of prediction and the average prediction of each decision tree is contributed to the final conclusion of random forest.

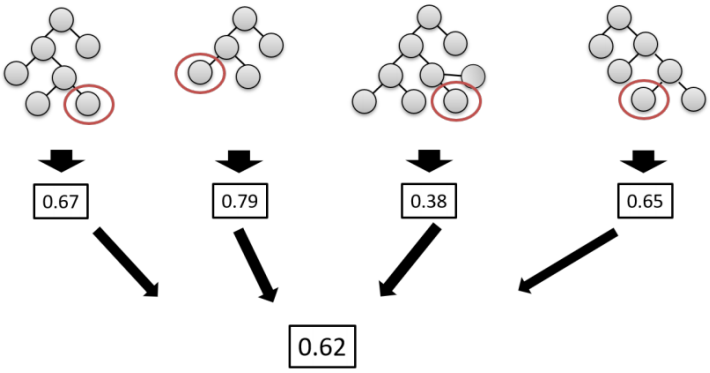

Figure 1.4. Example of the random forest algorithm ensemble approach. An ensemble of decision trees are created and used to generate an overall prediction for the algorithm.

1.3. High-throughput experimentation

Catalysis appears in all aspects of industrially process. Nowadays, even many catalysts have been invented for industrial application; research always motivates themselves to develop a novel catalyst with the ultimate aim reducing of more and more the cost, time, and energy for production. However, catalyst finding has mostly depended on the trial–and–error process, which is time–consuming and relies on serendipity. With the increasing demand for reducing time to release to market, an effective methods for catalyst development need be considered. High–throughput experimentation, which promises to speed up the discovery and development processes, has evolved rapidly during the last decade.

The catalyst preparation is a crucial step for the success for high–throughput screening. Preparation time is a pre-requisite component for HTS. The key for accelerating catalyst synthesis is to use a straightforward method such as impregnation and precipitation. These methods can be scaled up relatively quickly to numerous samples per day. In addition, the introduction of synthetic robots that can contribute greatly for enhancing the catalyst preparation process. The automation could significantly increase the synthesis throughput, otherwise, minimizing the mistake taken by human errors.

Another concern in high–throughput experimentation topics is the bottleneck of catalyst evaluation. While the catalyst preparation could be achieved numerous catalysts per day, the high-throughput screening (HTS) technique must take some effort to catch up that quantity. The common techniques for product evaluation are chromatography and spectroscopy. The key advantage of chromatography is high sensitivity, it is highly time–consuming. For example, if the product can be determined in five minutes using GC, it costs over five hours to analyze all 64 reactors [38]. Conversely, spectroscopic analysis enjoys the high speed screening but requires of

multivariate calibrati,n or deconvolution to obtain the concentrations of individual component. However, despite several weakness, spectroscopic analysis (IR and mass spectrometry) are now mature and frequently applied in HTS [39-41] in the various catalytic reaction such as OCM, coupling of methane with ammonia or aldol condensation of acetone . For example, mass spectrometry enables to obtain catalyst finding with capacity up to 80 catalysts per round. However, they only reported for catalyst information, while a few reaction conditions are measured. As catalyst performance is process dependent, reaction conditions is deemed to as crucial as catalyst information.

1.4. Catalysts informatics

Heterogeneous catalysis plays a vital role over 70% industrial chemical processes and greatly contributes to the global GDP [42]. Consequently, catalyst discovery and optimization greatly help to boost process efficiency, thus reducing the prices of the products and environmental footprints of the production [42]. The discovery and optimization process has been dominantly taken place via an Edisonian trial-and-error approach, which has been most successful yet costly and slow [37,43,44]. The speed of catalyst discovery and optimization could be expedited by more intelligent approaches such as design of experiments (DOE) and high-throughput experimentation [45]. Advances in computer infrastructures resulted in the breakthrough in computational techniques such as density functional theory (DFT), which allows implementation of in-silico catalyst design. Each of these techniques could accelerate catalyst discovery over the traditional Edisonian approach.

Another avenue for catalyst discovery that has gained popularity recently is machine learning [46]. Much similar to materials informatics, the application of machine learning for giving a better understating on a catalyst system or predicting new catalysts is called catalyst informatics. One of the earliest examples of catalysts informatics is related to the application of artificial neural networks (ANN) and genetic algorithms (GA) to experimental catalysis data [47]. Following this, due to the development of computational catalysis, many machine learning algorithms were applied for speeding up the catalyst finding and knowledge extraction from DFT databases. The purposes of these studies are to efficiently identify the most likely reaction mechanisms for CO hydrogenation [48], to discover more selective catalysts for chiral reactions, to learn atomistic potentials, and to predict the performance of catalysts [49]. Till now, most of efforts in the implementation of catalyst informatics have been limited to computational datasets, as they can be obtained in a very quick and consistent manner [37]. However, as stated in 1.1.2, computational datasets lack consideration of process conditions. This is more than critical for predicting catalysts, which are integral components of chemical processes and quite sensitive to process conditions. Therefore, this thesis focuses exclusively on the developments in experimental catalysis.

One of the earliest examples of catalysis informatics was reported in 1994 by Kito et al. [37]. They used an ANN to predict the product yield in oxidative hydrogenation of ethylbenzene when the surface area, the amount of a catalyst, and other catalyst materials information such as ionic radius, electronegativity, and standard heat of formation of oxides were given as the input. They training set contained the data of 18 promoted/unpromoted SnO_2 catalysts. Such severe restriction in the parametric

space was suitable for accurate prediction within interpolation but not adequate for the discovery of new catalyst compositions.

Following these pioneering paper, many research groups tried to explore catalyst informatics in optimizing the experimental conditions, and catalyst compositions, e.g. Sasaki et. al [50], Hou et al. [51]., Holena and Baerns [52-55] for NO decomposition, propane ammoxidation reaction, dehydrogenation of ethane (ODHE) to ethylene. However, these models only memorized the performance of the given compositions (i.e. data interpolation) rather than learned from the data, and thus, the prediction outside the training set gave poor results. The problems may come from the limited data size and the materials diversity.

More recent studies in catalyst informatics have focused on the past literature data to predict new catalysts. The Yildirim group made a statistical analysis of literature data for trans-esterification reactions using an ANN and a decision tree. 1324 data points were collected from 31 experimental publications [56]. Based on the decision tree and ANN analysis, they found that the most important variable for high conversion was the reaction time, and the other descriptors such as the catalyst loading, reactant amount, temperature, and type of supports exhibited only less than 10% relative importance.

Another effort by the same Yildirim group was on the collection of literature data for CO oxidation over Cu- and Au-based catalysts [57,58]. An ANN model well predicted within the data-rich regions, whereas the prediction was unfeasible in the other sparse regions. The Yildirim group also collected 4360 experimental data points on the Pt- or Au-catalyzed water gas shift reaction (WGS), which converts CO and H_2O to CO_2 and H_2 [59]. The dataset was studied using several data mining tools to extract

knowledge: Decision trees, ANNs and support vector machines. In particular, i) decision trees were utilized to comprehend the empirical rules and conditions for high CO conversion, and ii) ANN and support vector machines were used to assess the relative importance of a variety of experimental variables and their effects on the catalytic activity.

1.5. Oxidative coupling of methane

Methane, which is deemed as the major constituent of natural gas, is mostly being used for heating and for the production of electricity [60]. In some aspects, methane is a good fuel because of generating the highest heat of combustion regarded to the amount of CO_2 formed, among a wide ranges of hydrocarbons. Besides, methane is an under-utilized resource for producing chemicals and liquid fuels [39]. Known resources of natural gas are abundant and can be compete with liquid petroleum. Moreover, the known reserves of methane are increasing more rapidly than those of liquid petroleum. Methane are mostly found in located area, which is far away from industrial complexes [61]. This means its high cost for transportation is uneconomical. Transportation issues and the surging oil price have resulted in the great efforts for converting methane into easy transportable (methanol) and value-added products, such as ethylene (feedstock for petrochemicals), aromatics and liquid hydrocarbon fuels. One promising reaction to convert methane into C_2 building blocks is the oxidative coupling of methane (OCM), which was first published by Keller and Bhasin in 1982 [49].

1.5.1. Reaction mechanism of OCM

In the OCM process the following reactions occur simultaneously or sequentially [62,63]:

$2CH_4 + 0.5O_2 \rightarrow C_2H_6 + H_2O$ (1)

$C_2H_6 + 0.5O_2 \rightarrow C_2H_4 + H_2O$ (2)

$C_2H_6 \rightarrow C_2H_4 + H_2$ (3)

$CH_4 + 2O_2 \rightarrow CO_2 + 2H_2O$ (4)

$CH_4 + 1.5O_2 \rightarrow CO + 2H_2\ O$ (5)

$C_2H_6, C_2H_4, H_2 + O_2 \rightarrow CO, CO_2$, water (6)

The reaction starts with the coupling of methane to ethane (1). After that, ethylene is formed by either oxidative or non-oxidative dehydrogenation of ethane (2,3), while the reaction (3) occurs at a much rate than (2). The oxidative reactions (1) and (2) are slightly exothermic, and the combustion reactions (2), (4) and (5) are extremely exothermic, results in the excessive heat formation in the OCM process. Although the gas-phase free radical process plays a crucial role in the overall process, the contribution of a catalyst is significant. According to literature, methane dehydrogenates on surfaces of catalysts to form methyl radicals that can react on the surfaces or in the gas phase. The abstraction of a hydrogen atom is caused by oxygen atoms on the surfaces of the catalyst. Besides the efficient formation of methyl radicals, coupling of the radicals is also a key. It is true that coupling of CH_3• radicals takes place in the gas phase [64]. Several catalyst and reactor designs have been utilized.

1.5.2. Catalyst for OCM

Since the first reports by Keller and Bhasin [65] as well as by Hinsen and Baerns [66] in early 1980s, around 2300 publications have been published about OCM in literature. As reported in Ref. [60], about 50% of the publications was made in the first decade of the 30 years history of OCM, and then quickly lost attention after that. This is because no catalyst was found to meet an industrial target (C_2 yield higher than 30% using non-diluted reaction feeds and single pass reactor) [67]. Nevertheless, from 2000 to 2005, due to the newly discovery of huge reserves shale gas as well as due to the forecasted shortage of oil reserves, the OCM comes again as a hot topic. The Kondratenko group listed the recent progress of OCM catalysts, and depicted the published data on C_2 selectivity against methane conversion obtained over various catalysts under various reaction conditions [47]. They pointed out only four data points could achieve over 30% C_2 yield, however, all the four data points came from either a special reactor or an unstable catalyst, i.e. practically infeasible [60].

A numerous number of catalysts with and without supports have been evaluated for the OCM reaction with the target to explore active and stable catalysts. Table 1.1 shows the overview of the best-known performant catalysts, together with the reported values of the C_2 yield, the C_2 selectivity, temperature, CH_4/O_2, and lifetime. Note that direct comparison among the catalysts is not straightforward because various reactor configurations and reaction conditions were used among different research groups [68-71].

Table 1.1. List of best-known OCM catalysts.

Catalyst	Temperature (°C)	CH_4/O_2/diluent (mol/mol/mol)	C_2 yield (%)	C_2 selectivity (%)	Lifetime (h)
Eu_2O_3 [69]	725	6.7:1:0	17.7	72.4	n.d.
Ce/La_2O_3 [69]	775	4–5:1:0	22.3	66	n.d.
Li/MgO [70]	750	4:01:00	19	65	<100
La–Ce/MgO [69]	850	4–5:1:0	16.1	72.4	>10

$Mn–Na_2WO_4/SiO_2$ [71,72]	800/850	various	20	80	>100

The $Mn–Na_2WO_4/SiO_2$ system was an excellent catalyst in terms of high activity and good stability. It was also called the highest effective catalyst in literature from a review of Lunsford [62]. Other systems that have comparable activity show the lack of stability, or not reported. The optimum temperature is about 800°C is for most of the catalysts. Diluting reactant with an inert gas (He, Ar, or N_2) show better performance as gas-phase reactions are contributed less.

1.5.3. Catalysts informatics studies for OCM

Following the rise of catalysts informatics, Zavyalova et al. made statistical analysis of literature OCM data collected from 343 references and amounting to 1800 data points. Their aim was to find out optimal compositions of catalysts in terms of the C_2 yield [68]. Statistics analysis using various parameters such as the composition, process conditions, and the fabrication method withdrew hints for catalyst design, like "combining Mg or La with Cl positively affects the C_2 yield". This study was next followed by the report by Kondratenko et al., which was based on a neural network of a radial basis function (RBF) type and a traditional quadratic response surface to find out the optimum OCM catalysts [72]. They found that the RBF model provided higher accuracy more often than the quadratic response surface model. They also encountered a great difficulty in predicting catalysts from literature data due to the sparsity of the data: The catalysts were prepared based on different methods, and their performance was evaluated in different reaction conditions. To deal with these problems, the authors decided to ignore variation in the reaction and synthesis conditions, and instead to

consider only the catalyst composition. Another efforts on the implementation of catalyst informatics were reported by Takahashi et al. Based on the 1800 literature data and random forest classification, they predicted 56 undiscovered OCM catalysts expected to achieve the C_2 yield over 30% at their respective optimum conditions (yet not experimentally validated) [32]. They also noted that the literature data is quite noisy and not consistent in terms of the exerimental setup and its methodology, the type of catalysts, etc. Hence the implementation of regression was found to be nearly impossible.

The above-reviewed works are regarded the best representatives of the studies of the catalysts informatics for practical catalysis, such as OCM. It is seen that most of such catalyst informatics studies employed datasets acquired from literature: They suffer from severe scarcity, inconsistency, and human biases, which prevent the implementation of catalyst informatics as well as the prediction of breakthrough catalysts thereby. Thus, I conclude that the creation of systematic and bias-free datasets is the most important first step for the implementation of catalysts informatics.

1.6. Purpose of the Present Research

Catalyst informatics has emerged as an attractive field, which expects to bring irreversible change in the research and development of materials science. While the data mining and analysis tools have been well-developed, the implementation of catalysts informatics is bottlenecked by the lack of systematic and bias datasets. In this thesis, I set my focus on breaking-through this bottleneck and exploiting the true potential of catalyst informatics based on the acquisition of a systematic and bias-free dataset with high-throughput experimentation. The concept was proven by taking the

OCM reaction as a case study, which is a long researched reaction toward yet unsuccessful industrialization.

The first step to achieve my ultimate purpose is to develop the high-throughput screening (HTS) instrument for the evaluation of OCM catalysts. In Chapter 2, I successfully developed such a instrument, which enables to produce a systematic dataset with the capacity up to 4300 data/day under a parametric space of materials and process conditions in a fully automated fashion. It was proven that the HTS instrument can provide a machine-learnable dataset consisting of over 12,000 data points in a few days, and such a dataset is indeed very powerful to extract the knowledge about catalysis and performance improvement.

In Chapter 3, I investigated a hypothesis that was derived from catalyst informatics in Chapter 2. In detail, factors affecting the OCM performance of supported Mn–Na_2WO_4 were clarified based on the high-throughput screening and multilateral characterization.

In Chapter 4, I demonstrated a non-empirical exploration of new catalysts for OCM reaction with the aid of random sampling of a huge materials space and catalyst informatics. Here, 300 M1–M2–M3/Support catalysts were prepared and evaluated for the OCM reaction. Thus obtained bias-free dataset was deeply analyzed to successfully extract generalized rules of combinatorial catalyst design.

Based on all of the above-explained researches and achievements, I believe the thesis made a critical progress in the field of catalyst informatics.

References

[1] A. Agrawal, A. Choudhary, Perspective: Materials informatics and big data: Realization of the “fourth paradigm” of science in materials science, APL Mater., 4 (2016) 053208.

[2] M.I. Jordan, T.M.J.S. Mitchell, Machine learning: Trends, perspectives, and prospects, 349 (2015) 255-260.

[3] Y. Liu, T. Zhao, W. Ju, S. Shi, Materials discovery and design using machine learning, J Materiomics, 3 (2017) 159-177.

[4] R. Ramprasad, R. Batra, G. Pilania, A. Mannodi-Kanakkithodi, C. Kim, Machine learning in materials informatics: recent applications and prospects, Npj Comput. Mater., 3 (2017) 1-13.

[5] F. Oviedo, Z. Ren, S. Sun, C. Settens, Z. Liu, N.T.P. Hartono, S. Ramasamy, B.L. DeCost, S.I.P. Tian, G. Romano, A. Gilad Kusne, T. Buonassisi, Fast and interpretable classification of small X-ray diffraction datasets using data augmentation and deep neural networks, Npj Comput. Mater., 5 (2019) 60.

[6] H. Ding, I. Takigawa, H. Mamitsuka, S. Zhu, Similarity-based machine learning methods for predicting drug–target interactions: a brief review, Brief. Bioinform., 15 (2014) 734-747.

[7] T.K. Ho, Random decision forests, Proceedings of 3rd international conference on document analysis and recognition, IEEE, 1995, pp. 278-282.

[8] L. Ward, C. Wolverton, Atomistic calculations and materials informatics: A review, Curr. Opin. Solid State Mater. Sci., 21 (2017) 167-176.

[9] R.O. Jones, Density functional theory: Its origins, rise to prominence, and future, Rev. Mod. Phys., 87 (2015) 897-923.

[10] W. Setyawan, S. Curtarolo, High-throughput electronic band structure calculations: Challenges and tools, Comput. Mater. Sci., 49 (2010) 299-312.

[11] P.L. Freddolino, F. Liu, M. Gruebele, K. Schulten, Ten-microsecond molecular dynamics simulation of a fast-folding WW domain, Biophys. J., 94 (2008) L75-L77.

[12] T.C. Germann, K. Kadau, Trillion-atom molecular dynamics becomes a reality, Int. J. Mod. Phys. C, 19 (2008) 1315-1319.

[13] J.J. de Pablo, N.E. Jackson, M.A. Webb, L.-Q. Chen, J.E. Moore, D. Morgan, R. Jacobs, T. Pollock, D.G. Schlom, E.S. Toberer, New frontiers for the materials genome initiative, Npj Comput. Mater., 5 (2019) 41.

[14] S. Kirklin, J.E. Saal, B. Meredig, A. Thompson, J.W. Doak, M. Aykol, S. Rühl, C. Wolverton, The Open Quantum Materials Database (OQMD): assessing the accuracy of DFT formation energies, Npj Comput. Mater., 1 (2015) 1-15.

[15] C. Draxl, M. Scheffler, NOMAD: The FAIR concept for big data-driven materials science, MRS Bull., 43 (2018) 676-682.

[16] S. Curtarolo, W. Setyawan, G.L.W. Hart, M. Jahnatek, R.V. Chepulskii, R.H. Taylor, S. Wang, J. Xue, K. Yang, O. Levy, AFLOW: an automatic framework for high-throughput materials discovery, Comput. Mater. Sci., 58 (2012) 218-226.

[17] T.D. Huan, A. Mannodi-Kanakkithodi, R. Ramprasad, Accelerated materials property predictions and design using motif-based fingerprints, Phys. Rev. B, 92 (2015) 014106(014101)- 014106(014109).

[18] M. Fernandez, N.R. Trefiak, T.K. Woo, Atomic property weighted radial distribution functions descriptors of metal–organic frameworks for the prediction of gas uptake capacity, J. Phys. Chem. C, 117 (2013) 14095-14105.

[19] M. Fernandez, P.G. Boyd, T.D. Daff, M.Z. Aghaji, T.K. Woo, Rapid and accurate machine learning recognition of high performing metal organic frameworks for CO2 capture, J. Phys. Chem, 5 (2014) 3056-3060.

[20] Y.M. Arisoy, T. Özel, Machine learning based predictive modeling of machining induced microhardness and grain size in Ti–6Al–4V alloy, Mater. Manuf., 30 (2015) 425-433.

[21] K. Kim, L. Ward, J. He, A. Krishna, A. Agrawal, C. Wolverton, Machine-learning-accelerated high-throughput materials screening: Discovery of novel quaternary Heusler compounds, Phys. Rev. Mater., 2 (2018) 123801.

[22] K. Takahashi, L. Takahashi, I. Miyazato, J. Fujima, Y. Tanaka, T. Uno, H. Satoh, K. Ohno, M. Nishida, K. Hirai, J. Ohyama, T.N. Nguyen, S. Nishimura, T. Taniike, The rise of catalyst informatics: Towards catalyst genomics, ChemCatChem, 11 (2019) 1146-1152.

[23] Z.W. Ulissi, M.T. Tang, J. Xiao, X. Liu, D.A. Torelli, M. Karamad, K. Cummins, C. Hahn, N.S. Lewis, T.F. Jaramillo, K. Chan, J.K. Nørskov, Machine-Learning Methods Enable Exhaustive Searches for Active Bimetallic Facets and Reveal Active Site Motifs for CO2 Reduction, ACS Catal., 7 (2017) 6600-6608.

[24] Z. Li, X. Ma, H. Xin, Feature engineering of machine-learning chemisorption models for catalyst design, Catal. Today, 280 (2017) 232-238.

[25] J. Hattrick-Simpers, C. Wen, J. Lauterbach, The Materials Super Highway: Integrating High-Throughput Experimentation into Mapping the Catalysis Materials Genome, Catal. Lett., 145 (2015) 290-298.

[26] M.L. Green, C.L. Choi, J.R. Hattrick-Simpers, A.M. Joshi, I. Takeuchi, S.C. Barron, E. Campo, T. Chiang, S. Empedocles, J.M. Gregoire, Fulfilling the promise of the materials genome initiative with high-throughput experimental methodologies, Appl. Phys. Rev., 4 (2017) 011105.

[27] A. Zakutayev, N. Wunder, M. Schwarting, J.D. Perkins, R. White, K. Munch, W. Tumas, C. Phillips, An open experimental database for exploring inorganic materials, Sci. Data, 5 (2018) 180053.

[28] B. Meredig, C. Wolverton, Dissolving the periodic table in cubic zirconia: Data mining to discover chemical trends, Chem. Mater., 26 (2014) 1985-1991.

[29] L. Ward, A. Agrawal, A. Choudhary, C. Wolverton, A general-purpose machine learning framework for predicting properties of inorganic materials, Npj Comput. Mater., 2 (2016) 16028.

[30] X. Ma, Z. Li, L.E.K. Achenie, H. Xin, Machine-learning-augmented chemisorption model for CO2 electroreduction catalyst screening, J. Phys. Chem, 6 (2015) 3528-3533.

[31] J.M. Serra, A. Chica, A. Corma, Development of a low temperature light paraffin isomerization catalysts with improved resistance to water and sulphur by combinatorial methods, Appl. Catal., A, 239 (2003) 35-42.

[32] K. Takahashi, I. Miyazato, S. Nishimura, J. Ohyama, Unveiling hidden catalysts for the oxidative coupling of methane based on combining machine learning with literature data, ChemCatChem, 10 (2018) 3223-3228.

[33] A.J. Medford, A. Vojvodic, J.S. Hummelshøj, J. Voss, F. Abild-Pedersen, F. Studt, T. Bligaard, A. Nilsson, J.K. Nørskov, From the Sabatier principle to a predictive theory of transition-metal heterogeneous catalysis, J. Catal., 328 (2015) 36-42.

[34] A.J. Chowdhury, W. Yang, E. Walker, O. Mamun, A. Heyden, G.A. Terejanu, Prediction of adsorption energies for chemical species on metal catalyst surfaces using machine learning, J. Phys. Chem. C, 122 (2018) 28142-28150.

[35] D.H. Wolpert, W.G. Macready, No free lunch theorems for optimization, IEEE Trans. Evol. Comput., 1 (1997) 67-82.

[36] R. Kozma, C. Alippi, Y. Choe, F.C. Morabito, Artificial Intelligence in the Age of Neural networks and Brain computing, Academic Press2018.

[37] A.J. Medford, M.R. Kunz, S.M. Ewing, T. Borders, R. Fushimi, Extracting knowledge from data through catalysis informatics, ACS Catal., 8 (2018) 7403-7429.

[38] H.F.M. Boelens, D. Iron, J.A. Westerhuis, G. Rothenberg, Tracking chemical kinetics in high-throughput systems, Chem. Eur. J., 9 (2003) 3876-3881.

[39] L. Olivier, S. Haag, H. Pennemann, C. Hofmann, C. Mirodatos, A.C. van Veen, High-temperature parallel screening of catalysts for the oxidative coupling of methane, Catal. Today, 137 (2008) 80-89.

[40] S. Moehmel, N. Steinfeldt, S. Engelschalt, M. Holena, S. Kolf, M. Baerns, U. Dingerdissen, D. Wolf, R. Weber, M. Bewersdorf, New catalytic materials for the high-temperature synthesis of hydrocyanic acid from methane and ammonia by high-throughput approach, Appl. Catal., A, 334 (2008) 73-83.

[41] H. Wang, Z. Liu, J. Shen, Quantified MS analysis applied to combinatorial heterogeneous catalyst libraries, J. Comb. Chem., 5 (2003) 802-808.

[42] M. Boudart, Heterogeneous catalysis by metals, J. Mol. Catal., 30 (1985) 27-38.

[43] D. Xue, P.V. Balachandran, J. Hogden, J. Theiler, D. Xue, T. Lookman, Accelerated search for materials with targeted properties by adaptive design, Nat. Commun., 7 (2016) 1-9.

[44] B. Cao, L.A. Adutwum, A.O. Oliynyk, E.J. Luber, B.C. Olsen, A. Mar, J.M. Buriak, How to optimize materials and devices via design of experiments and machine learning: Demonstration using organic photovoltaics, ACS nano, 12 (2018) 7434-7444.

[45] R.J. Hendershot, C.M. Snively, J. Lauterbach, High-Throughput Heterogeneous Catalytic Science, Chem. Eur. J., 11 (2005) 806-814.

[46] Z. Li, S. Wang, H. Xin, Toward artificial intelligence in catalysis, Nat. Catal., 1 (2018) 641-642.

[47] T. Williams, K. McCullough, J.A. Lauterbach, Enabling catalyst discovery through machine learning and high-throughput experimentation, Chem. Mater., (2019).

[48] Z.W. Ulissi, A.J. Medford, T. Bligaard, J.K. Nørskov, To address surface reaction network complexity using scaling relations machine learning and DFT calculations, Nat. Commun., 8 (2017) 1-7.

[49] Z. Li, S. Wang, W.S. Chin, L.E. Achenie, H. Xin, High-throughput screening of bimetallic catalysts enabled by machine learning, J. Mater. Chem. A, 5 (2017) 24131-24138.

[50] M. Sasaki, H. Hamada, Y. Kintaichi, T. Ito, Application of a neural network to the analysis of catalytic reactions Analysis of NO decomposition over Cu/ZSM-5 zeolite, Appl. Catal., A, 132 (1995) 261-270.

[51] Z.Y. Hou, Q. Dai, X.Q. Wu, G.T. Chen, Artificial neural network aided design of catalyst for propane ammoxidation, Appl. Catal., A, 161 (1997) 183-190.

[52] U. Rodemerck, D. Wolf, O.V. Buyevskaya, P. Claus, S. Senkan, M. Baerns, High-throughput synthesis and screening of catalytic materials: Case study on the search for a low-temperature catalyst for the oxidation of low-concentration propane, Chem. Eng. J., 82 (2001) 3-11.

[53] D. Wolf, O.V. Buyevskaya, M. Baerns, An evolutionary approach in the combinatorial selection and optimization of catalytic materials, Appl. Catal., A, 200 (2000) 63-77.

[54] M. Holeňa, M. Baerns, Feedforward neural networks in catalysis: a tool for the approximation of the dependency of yield on catalyst composition, and for knowledge extraction, Catal. Today, 81 (2003) 485-494.

[55] U. Rodemerck, M. Baerns, M. Holena, D. Wolf, Application of a genetic algorithm and a neural network for the discovery and optimization of new solid catalytic materials, Appl. Surf. Sci., 223 (2004) 168-174.

[56] N. Alper Tapan, R. Yıldırım, M. Erdem Günay, Analysis of past experimental data in literature to determine conditions for high performance in biodiesel production, Biofuels, Bioproducts and Biorefining, 10 (2016) 422-434.

[57] M.E. Günay, R. Yildirim, Knowledge extraction from catalysis of the past: a case of selective CO oxidation over noble metal catalysts between 2000 and 2012, ChemCatChem, 5 (2013) 1395-1406.

[58] M.E. Gunay, R. Yildirim, Neural network analysis of selective CO oxidation over copper-based catalysts for knowledge extraction from published data in the literature, Ind. Eng. Chem. Res., 50 (2011) 12488-12500.

[59] Ç. Odabaşı, M.E. Günay, R. Yıldırım, Knowledge extraction for water gas shift reaction over noble metal catalysts from publications in the literature between 2002 and 2012, Int. J. Hydrog. Energy, 39 (2014) 5733-5746.

[60] E.V. Kondratenko, T. Peppel, D. Seeburg, V.A. Kondratenko, N. Kalevaru, A. Martin, S. Wohlrab, Methane conversion into different hydrocarbons or oxygenates: current status and future perspectives in catalyst development and reactor operation, Catal. Sci. Technol., 7 (2017) 366-381.

[61] H. Liu, X. Wang, D. Yang, R. Gao, Z. Wang, J. Yang, Scale up and stability test for oxidative coupling of methane over Na_2WO_4-Mn/SiO_2 catalyst in a 200 mL fixed-bed reactor, J. Nat. Gas Chem., 17 (2008) 59-63.

[62] J.H. Lunsford, Catalytic conversion of methane to more useful chemicals and fuels: a challenge for the 21st century, Catal. Today, 63 (2000) 165-174.

[63] R. Spinicci, P. Marini, S. De Rossi, M. Faticanti, P. Porta, Oxidative coupling of methane on LaAlO3 perovskites partially substituted with alkali or alkali-earth ions, J. Mol. Catal. A: Chem., 176 (2001) 253-265.

[64] J. Sun, J.W. Thybaut, G.B. Marin, Microkinetics of methane oxidative coupling, Catal. Today, 137 (2008) 90-102.

[65] G.E. Keller, M.M. Bhasin, Synthesis of ethylene via oxidative coupling of methane: I. Determination of active catalysts, J. Catal., 73 (1982) 9-19.

[66] W. Hinsen, M. Baerns, Oxidative coupling of methane to C2 hydrocarbons in the presence of different catalysts, Chem. Inform., 14 (1983).

[67] B.L. Farrell, V.O. Igenegbai, S. Linic, A Viewpoint on Direct Methane Conversion to Ethane and Ethylene Using Oxidative Coupling on Solid Catalysts, ACS Catal., 6 (2016) 4340-4346.

[68] U. Zavyalova, M. Holena, R. Schlögl, M. Baerns, Statistical analysis of past catalytic data on oxidative methane coupling for new insights into the composition of high-performance catalysts, ChemCatChem, 3 (2011) 1935-1947.

[69] T.V. Choudhary, D.W. Goodman, CO-free fuel processing for fuel cell applications, Catal. Today, 77 (2002) 65-78.

[70] S. Arndt, T. Otremba, U. Simon, M. Yildiz, H. Schubert, R. Schomäcker, Mn-Na_2WO_4/SiO_2 as catalyst for the oxidative coupling of methane. What is really known?, Appl. Catal., A, 425-426 (2012) 53-61.

[71] M. Yildiz, Y. Aksu, U. Simon, T. Otremba, K. Kailasam, C. Göbel, F. Girgsdies, O. Görke, F. Rosowski, A. Thomas, R. Schomäcker, S. Arndt, Silica material variation for the Mn_xO_y-Na_2WO_4/SiO_2, Appl. Catal., A, 525 (2016) 168-179.

[72] E.V. Kondratenko, M. Schlüter, M. Baerns, D. Linke, M. Holena, Developing catalytic materials for the oxidative coupling of methane through statistical analysis of literature data, Catal. Sci. Technol., 5 (2015) 1668-1677.

Chapter 2

High-throughput experimentation and catalyst informatics for oxidative coupling of methane

Abstract: The presence of a dataset that covers a parametric space of materials and process conditions in a process-consistent manner is essential for the realization of catalyst informatics. Here, an important piece of progress is demonstrated for oxidative coupling of methane. A high-throughput screening instrument is developed for enabling an automatic performance evaluation of 20 catalysts in 216 reaction conditions. This affords an OCM dataset comprised of 12708 data points for 59 catalysts in three successive operations. Based on a variety of data visualization analysis, important insights on catalysis and catalyst design are successfully extracted. In particular, simultaneous optimization of the catalyst and reactor design is found to be essential for improving the C_2 yield. The consistent dataset allows the accurate prediction of the C_2 yield with the aid of non-linear supervised machine learning.

Keywords: High-throughput experimentation, Catalyst informatics, Oxidative coupling of methane, Machine learning, Data visualization

2.1. Introduction

Materials informatics (MI) is one rising area of materials science. It applies data-oriented approaches with expectation to bring irreversible change in the research and development of materials science [1–3]. The prerequisite of MI is the presence of a proper dataset in terms of consistency, distribution, and size [2]. Once such a dataset is prepared, an appropriate learning method is selected from the toolbox [4,5]. Tremendous efforts made in this emerging field of study have highlighted key challenges specific to materials. In particular, the most important challenge is on the data themselves [6]. Despite the growing accumulation of materials data in literature, the availability of proper datasets is often limited. This is partly because many materials properties are process dependent (e.g. mechanical properties of polymers, activities of catalysts), while researchers employ their own protocols and conditions. Another difficulty derives from the complicated structures of materials [7]. Properties of solid materials depend not only on their chemical structure but also on structures/morphology of different scales such as higher-order structures of polymers, grain boundaries, pores of inorganic materials, etc [8]. This multivariate dependence has been often neglected in conventional x,y structure-performance studies, where potentially important but un-focused features are even un-reported. These problems likely do not affect conclusions in individual literature, but when collected, can result in an inconsistent and sparse dataset.

The problem of process dependence is maximized when MI is employed in the development of catalysts, i.e. integral component of chemical processes. Here, the problem is briefly illustrated by taking oxidative coupling of methane (OCM) as an example. The OCM is an important class of reactions in terms of the abundance of methane and its direct upgrading without mediating syngas. A wide variety of catalysts

have been explored to address a conversion-selectivity tradeoff that arises from the poor reactivity of methane with respect to desired products [9,10]. In 2011, Zavyalova et al. collected 1870 OCM literature data of the past three decades [11], which assessed both positive and negative aspects of catalyst informatics. The negative aspects are seen to relate to the dataset directly. First, the dataset size is insufficient with respect to the parametric space (a multidimensional space spanned by catalyst features and process conditions). Second, past research has more or less focused on a few to several catalyst systems such as Mn-Na_2WO_4/SiO_2, Li/MgO, and La-Sr/CaO. This concentration, together with the deviation of process windows among different catalyst systems, leads to heavily biased sampling [12]. Third, differences in reactor design and temperature protocol among literature can introduce deviation in the resultant performance even when the same catalyst is employed. The total heat balance becomes impactful for largely exothermic/endothermic reactions and when a few-percentage improvement is regarded significant. For example, the best-of-literature C_2 yield of the Mn-Na_2WO_4/SiO_2 OCM catalyst varied from 16.0 to 26.4% in a typical fixed-bed reactor configuration [11,13,14]. Lastly, desire for positive data has resulted in the burial of an enormous quantity of so-called poor data, which can potentially provide good insights for researchers as well as machines [12,15]. In a recent publication, a negative impact of such anthropogenic biases is discussed. The anthropogenic biases make data distribution highly disproportionate, and this leads to the prediction outcome inferior to random sampling in the amine-templated synthesis of crystalline metal oxides [16]. To be important, the research field of OCM is regarded rather saturated and therefore the dataset problem is believed to be common in other catalysis. On the basis of the above discussions, high-throughput experimentation is proposed as a key issue of catalyst informatics to produce a proper catalyst dataset on-demand under unified process

conditions [17,18]. In this chapter, I report an important piece of progress for the implementation of catalyst informatics, which includes:

i) Development of a high-throughput screening (HTS) instrument: The instrument realizes automatic performance evaluation of 20 catalysts at a series of predefined conditions in fixed-bed reactors. This affords a few thousand catalyst data per day in a process-consistent manner.

ii) Creation of an OCM dataset: A consistent OCM dataset (12708 data) was produced for Mn-Na_2WO_4/SiO_2-type catalysts. The catalysts varied in the elements of active phases, support type, and chemical composition. The performance of 59 catalysts (including reference materials) was evaluated at different feed compositions, contact times, and temperatures.

iii) Open database: The above-mentioned dataset is uploaded in a web platform "Catalyst Acquisition by Data Science (CADS)" for shared usage [19].

iv) Machine learning: It signified the importance of a consistent dataset for achieving reliable prediction. A model based on random forest regression accurately described the dependence of the C_2 yield on reaction conditions via interpolation filling

.

2.2. Experimental and analytical details

2.2.1. Catalyst library

Table 2.1 shows the catalyst library used in this chapter. Among the 59 entries, 40 were derived from Mn-Na_2WO_4/SiO_2, one of the most effective catalysts for OCM. They are represented in the form of M1-$M2_{1\text{-}2}M3O_4$/support. M1 was picked up from a wide range of transition metal and lanthanide elements; M2 and M3 came from commercially available tungstates or molybdates; supports were selected from commonly used materials. The metal loadings to a unit gram of a support were fixed at 0.371 mmol for M1, 0.370 or 0.185 mmol for M2 (depending on the valence), and 0.185 mmol for M3. These correspond to the optimum composition for Mn-Na_2WO_4/SiO_2 in literature [20–22]. The remaining 19 entries are reference samples, which include blank (no catalyst material), bare supports, and samples that lack one or two metallic components from Mn-Na_2WO_4/SiO_2.

The catalysts were prepared based on a co-impregnation method [20,21]. 1.0 g of a support was impregnated with 4–5 mL of an aqueous solution of specified metal precursors at 50 °C for 6 hours. After vacuum drying at 110 °C, the product was calcined at 1000 °C under air for 3 hours to yield a catalyst. When a water-sensitive metal alkoxide was employed, the impregnation was sequentially performed in the order of an aqueous solution of a tungstate and an ethanol solution of a metal alkoxide. The obtained catalysts were thoroughly ground before any usage. The catalyst preparation was appropriately parallelized with the aids of a parallel hot stirrer (Reacti-Therm, Thermo Scientific) and a centrifugal evaporator (CVE-3100, Eyela). 20 catalysts were produced in one batch. The samples were characterized by X-ray

diffraction (XRD) and scanning electron microscopy (SEM). These results are shown in Figures 2.1 and 2.2.

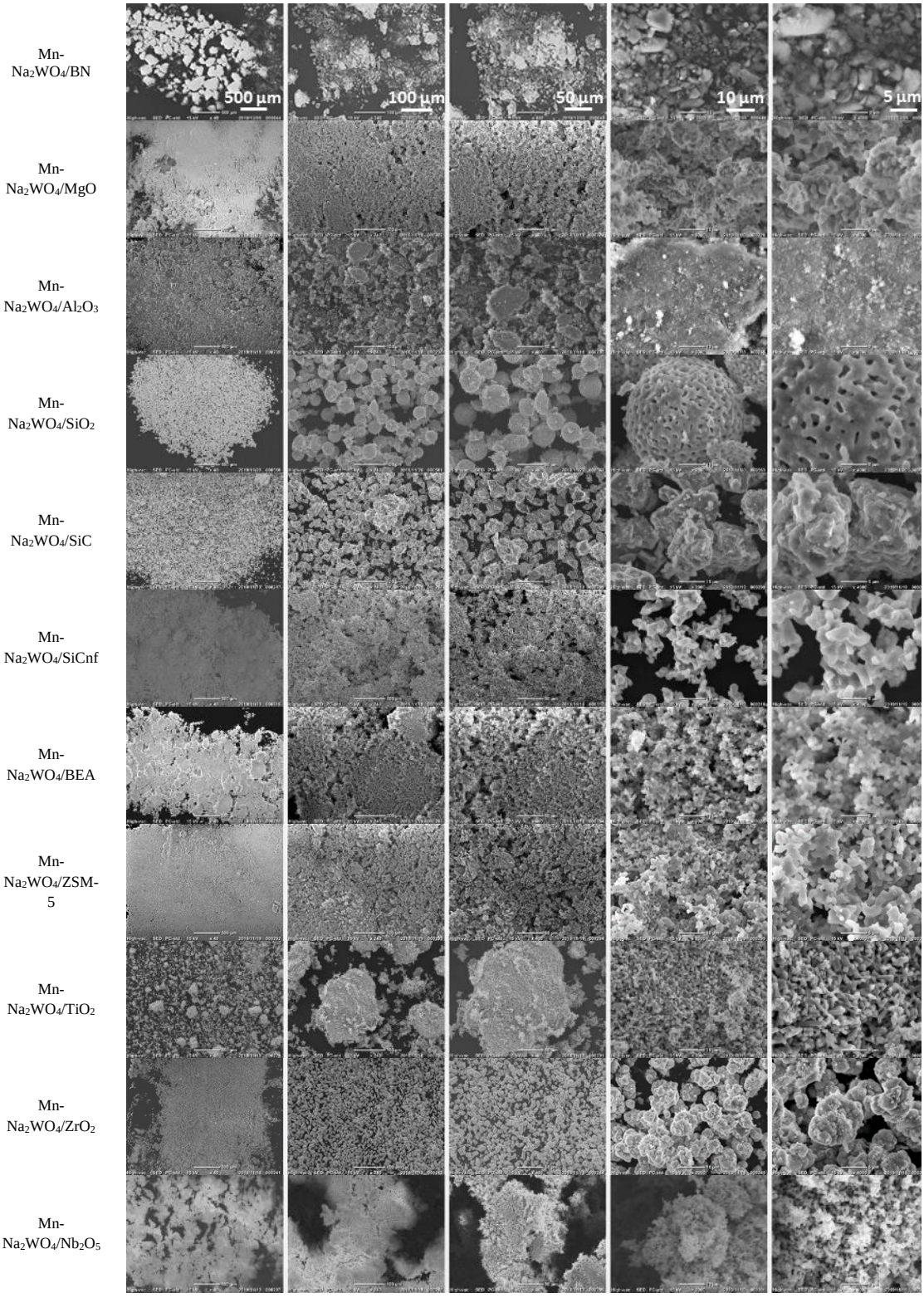

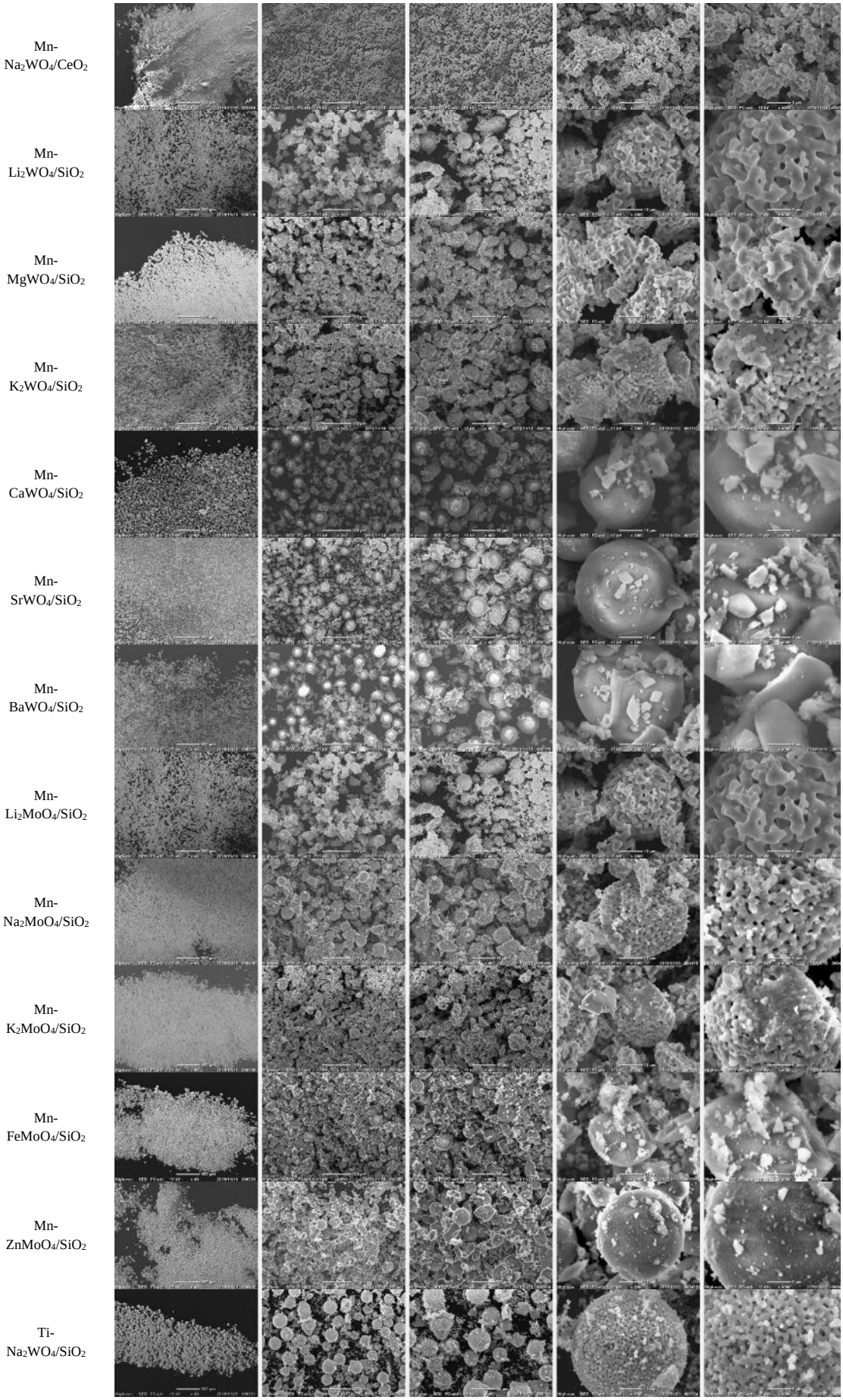
Mn-Na2WO4/CeO2
Mn-Li2WO4/SiO2
Mn-MgWO4/SiO2
Mn-K2WO4/SiO2
Mn-CaWO4/SiO2
Mn-SrWO4/SiO2
Mn-BaWO4/SiO2
Mn-Li2MoO4/SiO2
Mn-Na2MoO4/SiO2
Mn-K2MoO4/SiO2
Mn-FeMoO4/SiO2
Mn-ZnMoO4/SiO2
Ti-Na2WO4/SiO2

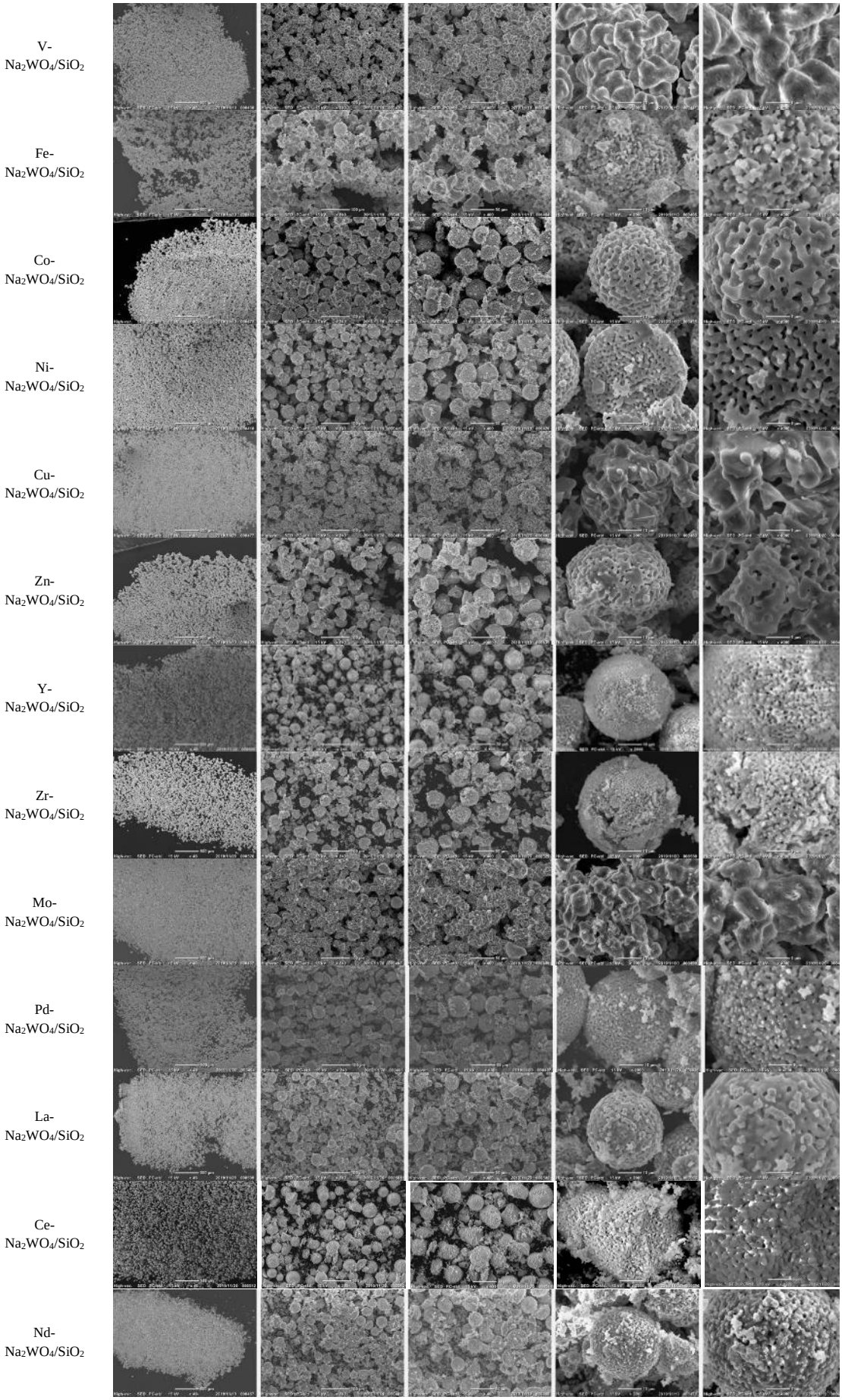
V-Na2WO4/SiO2
Fe-Na2WO4/SiO2
Co-Na2WO4/SiO2
Ni-Na2WO4/SiO2
Cu-Na2WO4/SiO2
Zn-Na2WO4/SiO2
Y-Na2WO4/SiO2
Zr-Na2WO4/SiO2
Mo-Na2WO4/SiO2
Pd-Na2WO4/SiO2
La-Na2WO4/SiO2
Ce-Na2WO4/SiO2
Nd-Na2WO4/SiO2

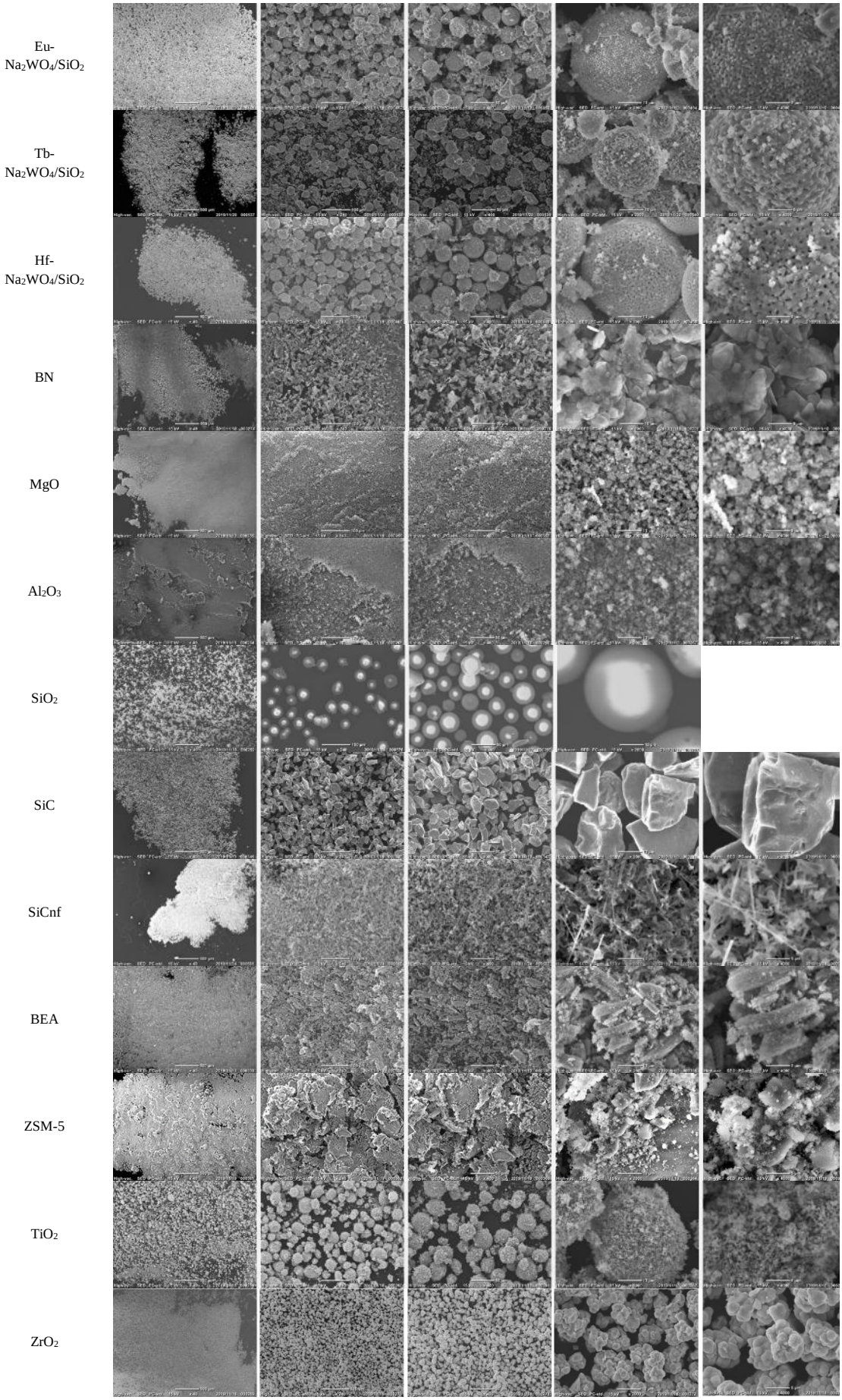
Eu-Na2WO4/SiO2
Tb-Na2WO4/SiO2
Hf-Na2WO4/SiO2
BN
MgO
Al2O3
SiO2
SiC
SiCnf
BEA
ZSM-5
TiO2
ZrO2

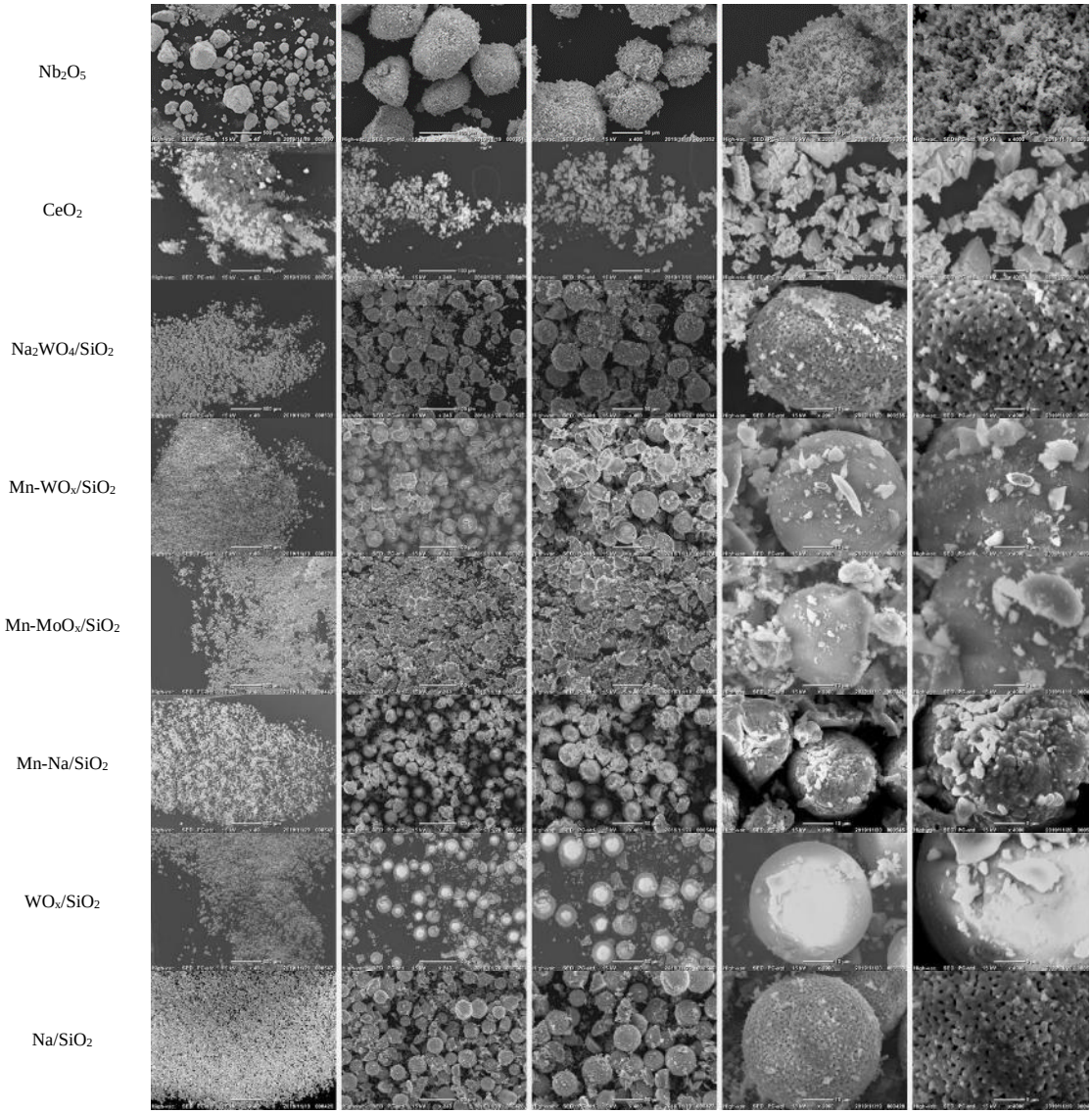

Figure 2.1. SEM images of catalyst samples. The scale bars are applied to individual columns. Micrographs were acquired on JCM-6000Plus NeoScope operated at an acceleration voltage of 15 kV.

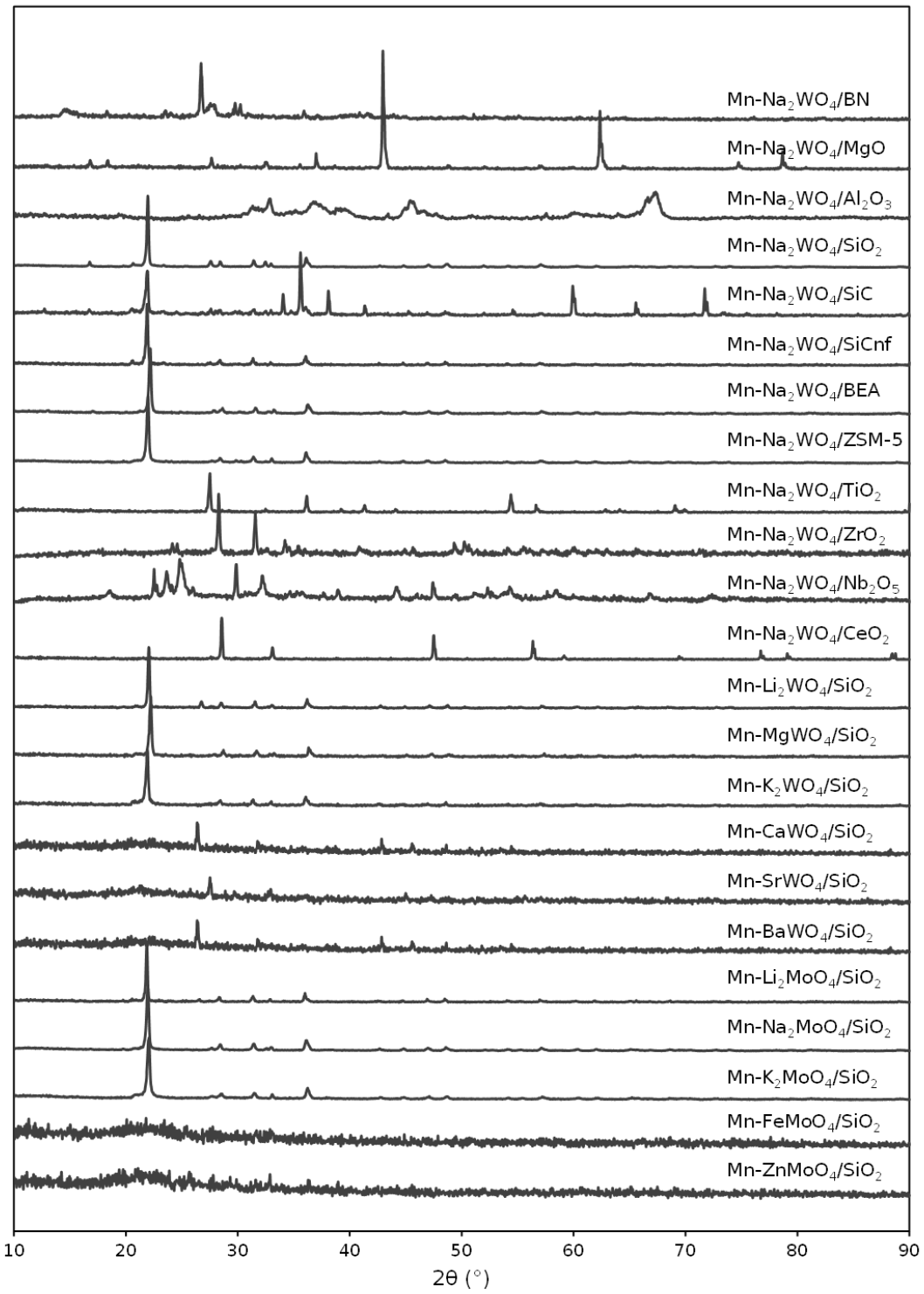
Mn-Na2WO4/BN
Mn-Na2WO4/MgO
Mn-Na2WO4/Al2O3
Mn-Na2WO4/SiO2
Mn-Na2WO4/SiC
Mn-Na2WO4/SiCnf
Mn-Na2WO4/BEA
Mn-Na2WO4/ZSM-5
Mn-Na2WO4/TiO2
Mn-Na2WO4/ZrO2
Mn-Na2WO4/Nb2O5
Mn-Na2WO4/CeO2
Mn-Li2WO4/SiO2
Mn-MgWO4/SiO2
Mn-K2WO4/SiO2
Mn-CaWO4/SiO2
Mn-SrWO4/SiO2
Mn-BaWO4/SiO2
Mn-Li2MoO4/SiO2
Mn-Na2MoO4/SiO2
Mn-K2MoO4/SiO2
Mn-FeMoO4/SiO2
Mn-ZnMoO4/SiO2
10
20
30
40
50
60
70
80
90
2θ (°)

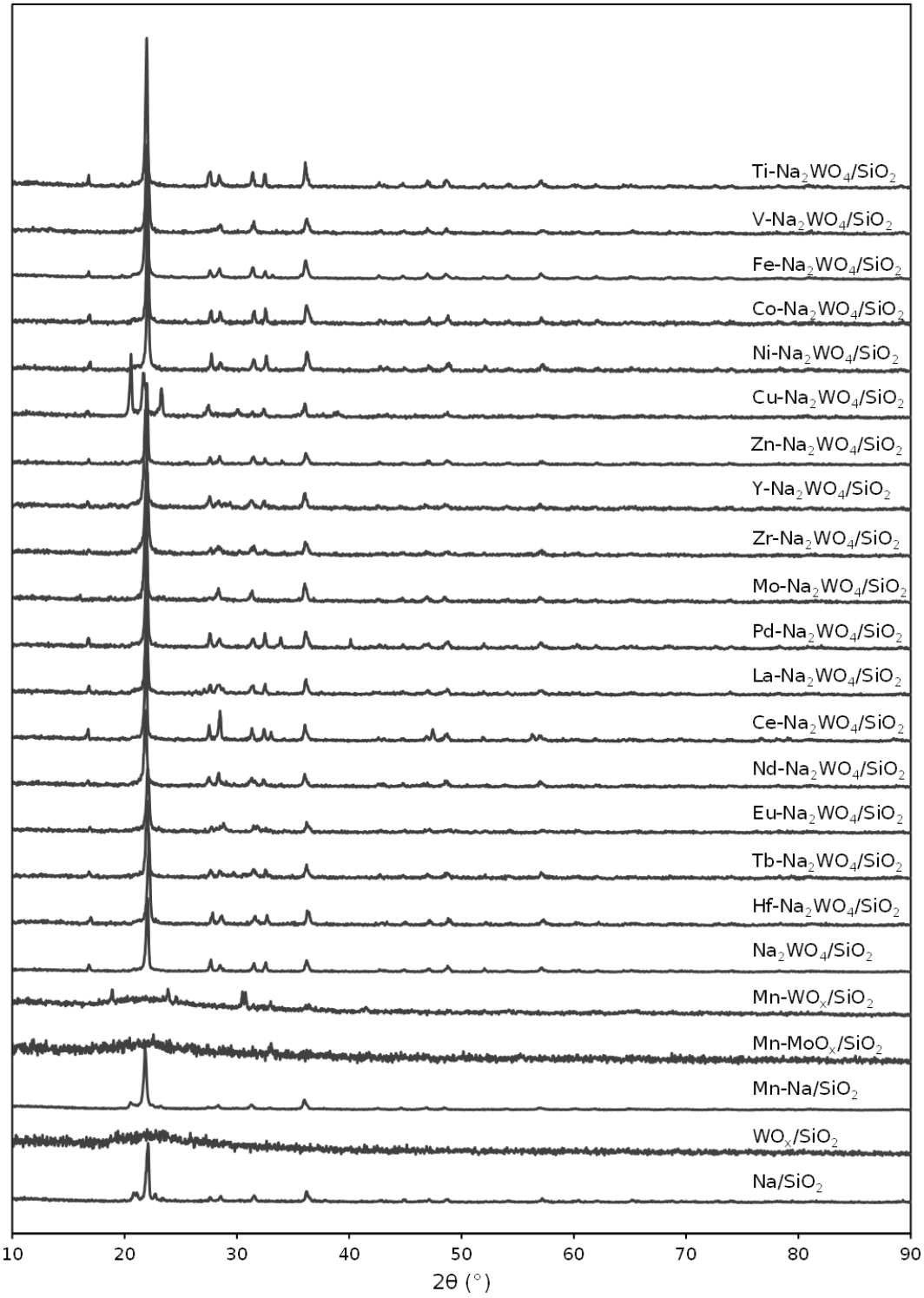

Figure 2.2. XRD patterns of catalyst samples (except bare supports). The XRD patterns were recorded on Rigaku SMARTLAB using Cu Kα (1.5418 Å) radiation. A step scan mode was employed in the 2θ range of 5–90° at the step size of 0.008°.

Table 2.1. List of catalysts.

Catalyst name	Precursor	Support[a]	M1[b]	M2[b]	M3[b]
Mn-Na_2WO_4/BN	$Mn(NO_3)_2{\cdot}6H_2O$, Na_2WO_4	BN	Mn (40)	Na (40)	W (20)
Mn-Na_2WO_4/MgO	$Mn(NO_3)_2{\cdot}6H_2O$, Na_2WO_4	MgO	Mn (40)	Na (40)	W (20)
Mn-Na_2WO_4/Al_2O_3	$Mn(NO_3)_2{\cdot}6H_2O$, Na_2WO_4	Al_2O_3	Mn (40)	Na (40)	W (20)
Mn-Na_2WO_4/SiO_2	$Mn(NO_3)_2{\cdot}6H_2O$, Na_2WO_4	SiO_2	Mn (40)	Na (40)	W (20)
Mn-Na_2WO_4/SiC	$Mn(NO_3)_2{\cdot}6H_2O$, Na_2WO_4	SiC	Mn (40)	Na (40)	W (20)
Mn-Na_2WO_4/SiCnf	$Mn(NO_3)_2{\cdot}6H_2O$, Na_2WO_4	SiCnf	Mn (40)	Na (40)	W (20)
Mn-Na_2WO_4/BEA	$Mn(NO_3)_2{\cdot}6H_2O$, Na_2WO_4	BEA	Mn (40)	Na (40)	W (20)
Mn-Na_2WO_4/ZSM-5	$Mn(NO_3)_2{\cdot}6H_2O$, Na_2WO_4	ZSM-5	Mn (40)	Na (40)	W (20)
Mn-Na_2WO_4/TiO_2	$Mn(NO_3)_2{\cdot}6H_2O$, Na_2WO_4	TiO_2	Mn (40)	Na (40)	W (20)
Mn-Na_2WO_4/ZrO_2	$Mn(NO_3)_2{\cdot}6H_2O$, Na_2WO_4	ZrO_2	Mn (40)	Na (40)	W (20)
Mn-Na_2WO_4/Nb_2O_5	$Mn(NO_3)_2{\cdot}6H_2O$, Na_2WO_4	Nb_2O_5	Mn (40)	Na (40)	W (20)
Mn-Na_2WO_4/CeO_2	$Mn(NO_3)_2{\cdot}6H_2O$, Na_2WO_4	CeO_2	Mn (40)	Na (40)	W (20)
Mn-Li_2WO_4/SiO_2	$Mn(NO_3)_2{\cdot}6H_2O$, Li_2WO_4	SiO_2	Mn (40)	Li (40)	W (20)
Mn-$MgWO_4$/SiO_2	$Mn(NO_3)_2{\cdot}6H_2O$, $MgWO_4$	SiO_2	Mn (50)	Mg (25)	W (25)
Mn-K_2WO_4/SiO_2	$Mn(NO_3)_2{\cdot}6H_2O$, K_2WO_4	SiO_2	Mn (40)	K (40)	W (20)
Mn-$CaWO_4$/SiO_2	$Mn(NO_3)_2{\cdot}6H_2O$, $CaWO_4$	SiO_2	Mn (50)	Ca (25)	W (25)
Mn-$SrWO_4$/SiO_2	$Mn(NO_3)_2{\cdot}6H_2O$, $SrWO_4$	SiO_2	Mn (50)	Sr (25)	W (25)
Mn-$BaWO_4$/SiO_2	$Mn(NO_3)_2{\cdot}6H_2O$, $BaWO_4$	SiO_2	Mn (50)	Ba (25)	W (25)
Mn-Li_2MoO_4/SiO_2	$Mn(NO_3)_2{\cdot}6H_2O$, Li_2MoO_4	SiO_2	Mn (40)	Li (40)	Mo (20)
Mn-Na_2MoO_4/SiO_2	$Mn(NO_3)_2{\cdot}6H_2O$, Na_2MoO_4	SiO_2	Mn (40)	Na (40)	Mo (20)
Mn-K_2MoO_4/SiO_2	$Mn(NO_3)_2{\cdot}6H_2O$, K_2MoO_4	SiO_2	Mn (40)	K (40)	Mo (20)
Mn-$FeMoO_4$/SiO_2	$Mn(NO_3)_2{\cdot}6H_2O$, $FeMoO_4$	SiO_2	Mn (50)	Fe (25)	Mo (25)
Mn-$ZnMoO_4$/SiO_2	$Mn(NO_3)_2{\cdot}6H_2O$, $ZnMoO_4$	SiO_2	Mn (50)	Zn (25)	Mo (25)
Ti-Na_2WO_4/SiO_2	Ti(O*i*Pr)$_4$, Na_2WO_4	SiO_2	Ti (40)	Na (40)	W (20)
V-Na_2WO_4/SiO_2	$VOSO_4{\cdot}xH_2O$ (x=3-5), Na_2WO_4	SiO_2	V (40)	Na (40)	W (20)
Fe-Na_2WO_4/SiO_2	$Fe(NO_3)_3{\cdot}9H_2O$, Na_2WO_4	SiO_2	Fe (40)	Na (40)	W (20)
Co-Na_2WO_4/SiO_2	$Co(NO_3)_2{\cdot}6H_2O$, Na_2WO_4	SiO_2	Co (40)	Na (40)	W (20)
Ni-Na_2WO_4/SiO_2	$Ni(NO_3)_2{\cdot}6H_2O$, Na_2WO_4	SiO_2	Ni (40)	Na (40)	W (20)
Cu-Na_2WO_4/SiO_2	$Cu(NO_3)_2{\cdot}5H_2O$, Na_2WO_4	SiO_2	Cu (40)	Na (40)	W (20)
Zn-Na_2WO_4/SiO_2	$Zn(NO_3)_2{\cdot}6H_2O$, Na_2WO_4	SiO_2	Zn (40)	Na (40)	W (20)
Y-Na_2WO_4/SiO_2	$Y(NO_3)_3{\cdot}6H_2O$, Na_2WO_4	SiO_2	Y (40)	Na (40)	W (20)
Zr-Na_2WO_4/SiO_2	$ZrO(NO_3)_2{\cdot}2H_2O$, Na_2WO_4	SiO_2	Zr (40)	Na (40)	W (20)
Mo-Na_2WO_4/SiO_2	$(NH_4)_2MoO_4$, Na_2WO_4	SiO_2	Mo (40)	Na (40)	W (20)
Pd-Na_2WO_4/SiO_2	$Pd(OAc)_2$, Na_2WO_4	SiO_2	Pd (40)	Na (40)	W (20)
La-Na_2WO_4/SiO_2	$La(NO_3)_3$, Na_2WO_4	SiO_2	La (40)	Na (40)	W (20)
Ce-Na_2WO_4/SiO_2	$Ce(NO_3)_3{\cdot}6H_2O$, Na_2WO_4	SiO_2	Ce (40)	Na (40)	W (20)
Nd-Na_2WO_4/SiO_2	$Nd(NO_3)_3{\cdot}6H_2O$, Na_2WO_4	SiO_2	Nd (40)	Na (40)	W (20)
Eu-Na_2WO_4/SiO_2	$Eu(NO_3)_3{\cdot}5H_2O$, Na_2WO_4	SiO_2	Eu (40)	Na (40)	W (20)
Tb-Na_2WO_4/SiO_2	$Tb(NO_3)_3{\cdot}5H_2O$, Na_2WO_4	SiO_2	Tb (40)	Na (40)	W (20)
Hf-Na_2WO_4/SiO_2	Hf(OEt)$_4$, Na_2WO_4	SiO_2	Hf (40)	Na (40)	W (20)
Blank					
BN		BN			

MgO		MgO			
Al_2O_3		Al_2O_3			
SiO_2		SiO_2			
SiC		SiC			
SiCnf		SiCnf			
BEA		BEA			
ZSM-5		ZSM-5			
TiO_2		TiO_2			
ZrO_2		ZrO_2			
Nb_2O_5		Nb_2O_5			
CeO_2		CeO_2			
Na_2WO_4/SiO_2	Na_2WO_4	SiO_2		Na (67)	W (33)
Mn-WO_x/SiO_2	$Mn(NO_3)_2{\cdot}6H_2O$, $(NH_4)_{10}H_2(W_2O_7)_6$	SiO_2	Mn (67)		W (33)
Mn-MoO_x/SiO_2	$Mn(NO_3)_2{\cdot}6H_2O$, $(NH_4)_2MoO_4$	SiO_2	Mn (67)		Mo (33)
Mn-Na/SiO_2	$Mn(NO_3)_2{\cdot}6H_2O$, $NaNO_3$	SiO_2	Mn (50)	Na (50)	
WO_x/SiO_2	$(NH_4)_{10}H_2(W_2O_7)_6$	SiO_2			W (100)
Na/SiO_2	$NaNO_3$	SiO_2		Na (100)	

[a] Boron nitride (BN, 5.2 m^2/g, Wako Pure Chemical Industries, Ltd.), magnesium oxide (MgO, 5.5 m^2/g, Kanto Chemical Co., Inc.), aluminum oxide (γ-Al_2O_3, 150 m^2/g, Sumitomo Chemical Industry Co., Ltd.), silica gel (SiO_2, 650 m^2/g, 60N, Kanto Chemical Co., Inc.), silicon carbide (SiC, 1.5 m^2/g, Sigma-Aldrich), silicon carbide nanofiber (SiCnf, D < 2.5 μm, L/D ≥ 20, Sigma-Aldrich), BEA (560 m^2/g, SiO_2/Al_2O_3 = 104, zeolite HSZ-960HOA, Tosoh Corporation), ZSM-5 (300 m^2/g, SiO_2/Al_2O_3 = 90, zeolite JRC-Z5-90NA, Süd-Chemie Catalysts Japan), titanium (IV) oxide (TiO_2, 17.4 m^2/g, Kanto Chemical Co., Inc.), zirconium (IV) oxide (ZrO_2, 3.2 m^2/g, Kanto Chemical Co., Inc.), niobium (V) oxide (Nb_2O_5, 4.7 m^2/g, Wako Pure Chemical Industries, Ltd.), cerium (IV) oxide (CeO_2, 3.9 m^2/g, Wako Pure Chemical Industries, Ltd.). The surface area of the supports was obtained by the BET method. A sample was degassed at 150 °C for 10 h in vacuum prior to the N_2 adsorption measurement at 77 K.

[b] The values in parentheses correspond to relative atomic percentages of M1-M3. To a unit gram of a support, 0.371 mmol of M1, 0.370 or 0.185 mmol of M2, and 0.185 mmol of M3 were immobilized.

2.2.2. Instrumental

Figure 2.3 illustrates the HTS system developed and employed in this study. The instrument consists of a mixed gas generator, a flow distributor, reaction tubes, an electric furnace, an auto-sampler, a quadrupole mass spectrometer (QMS), and an exhaust system. The gas generator (MU-3504, HORIBA STEC) supplies a reaction gas mixture of an arbitrary $CH_4/O_2/Ar$ volume ratio at a specified total flow volume (typically 100–200 mL/min). Then, the mixture is equally split into 20 reaction tubes at the gas distributor. Uniform gas distribution is achieved with the aid of capillaries (length = 1 m, I.D. = 0.2 mm). The flow resistance is set sufficiently large so that the resistance from catalyst beds hardly affects the distribution (Figure 2.4a). After being

split into 20 fractions, the gas mixture passes through reaction tubes. A reaction tube is made of a quartz tube whose internal diameter changes from 4 mm in the feed side to 2 mm in the effluent side. This design of the reaction tube assures not only the inertness of the reactor wall at an elevated temperature but also the suppression of undesired gas-phase reactions in the effluent side. A specified height of catalyst powder is fixed at the neck position of the reaction tube with the aid of quartz wool. The reaction tubes are symmetrically placed in a hollow electric furnace. The furnace consists of three temperature zones ($T_{1–3}$), each of which equips a thermocouple and ceramic heater for PID control. The catalyst beds are placed in the middle of the center zone, i.e. when the same temperature is applied for the three zones, the other two zones become a buffer to stabilize the temperature of the catalyst beds at the center zone. The effluent gas from the 20 reaction tubes is transferred to the sampling line of the auto-sampler, which is connected to a diaphragm pump and the inlet of the QMS (Transpector® CPM 3, INFICON). The auto sampling is achieved by a programmed action sequence of pneumatically-actuated diaphragm valves (MEGA-ONE®, Fujikin). Typically, the effluent gas of one reactor tube is sampled for 1.6 seconds, and the sampling line is cleared by evacuation for 7.0 seconds, thus corresponding to 172 seconds for one round. The un-sampled fraction of the effluent gas is discharged through the exhaust system. During the sampling, the effluent gas is continuously transferred to the QMS, and the mass spectra are recorded for a predetermined set of mass numbers. 12 mass spectra are acquired in 1.6 seconds. The mass signal intensities are converted to the relative pressure of individual gas species using external calibration, where scaling factors are obtained for a few major fragments to deal with overlapping fragments. As can be seen in Figure 2.4b, the relative pressure is accurately determined based on the above-mentioned protocol. Finally, cooperation among the programmed gas generation,

temperature, and auto-sampling enables full automation in evaluating the performance of 20 catalysts for a predetermined set of reaction conditions. A safety management system also backups the automation. Here, it is worth noting that HTS instruments having more or less similar mechanic design were reported in literature [23-26], but these instruments were mostly used for catalyst screening at one or a few fixed conditions. The developed instrument enables the acquisition of a dataset that covers a parametric space for both catalysts and process conditions by means of parallelization and automation, respectively. The consistency of results among 20 channels was carefully confirmed using a Mn-Na_2WO_4/SiO_2 catalyst (Figure 2.5).

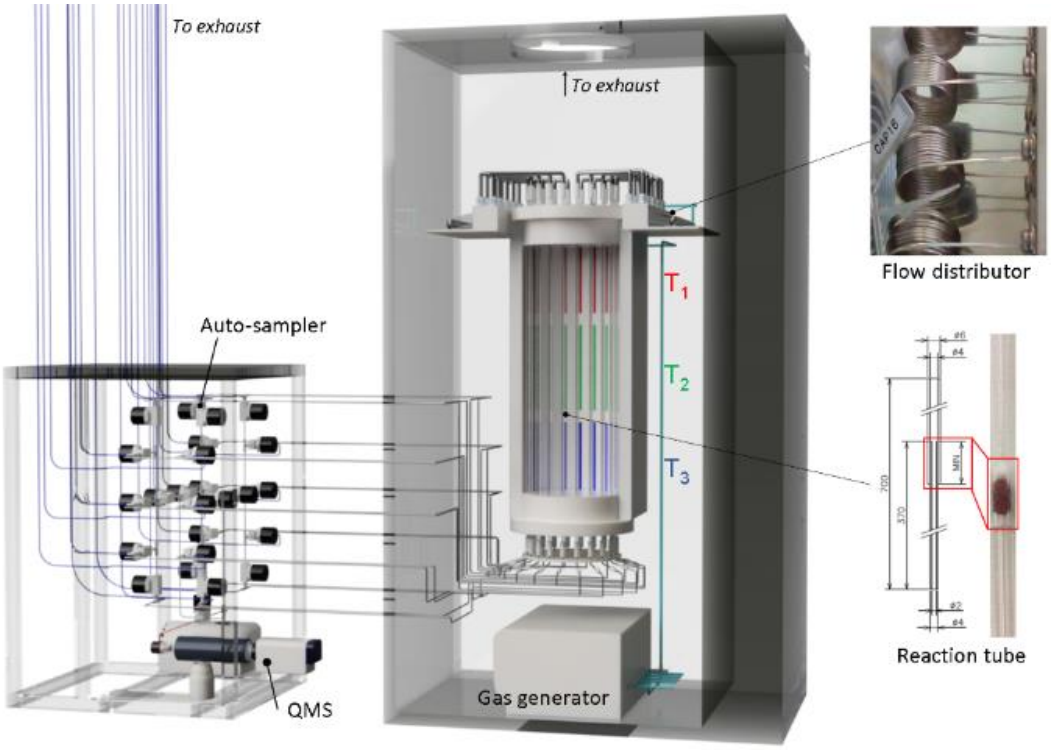

Figure 2.3. Illustration of the developed HTS system.

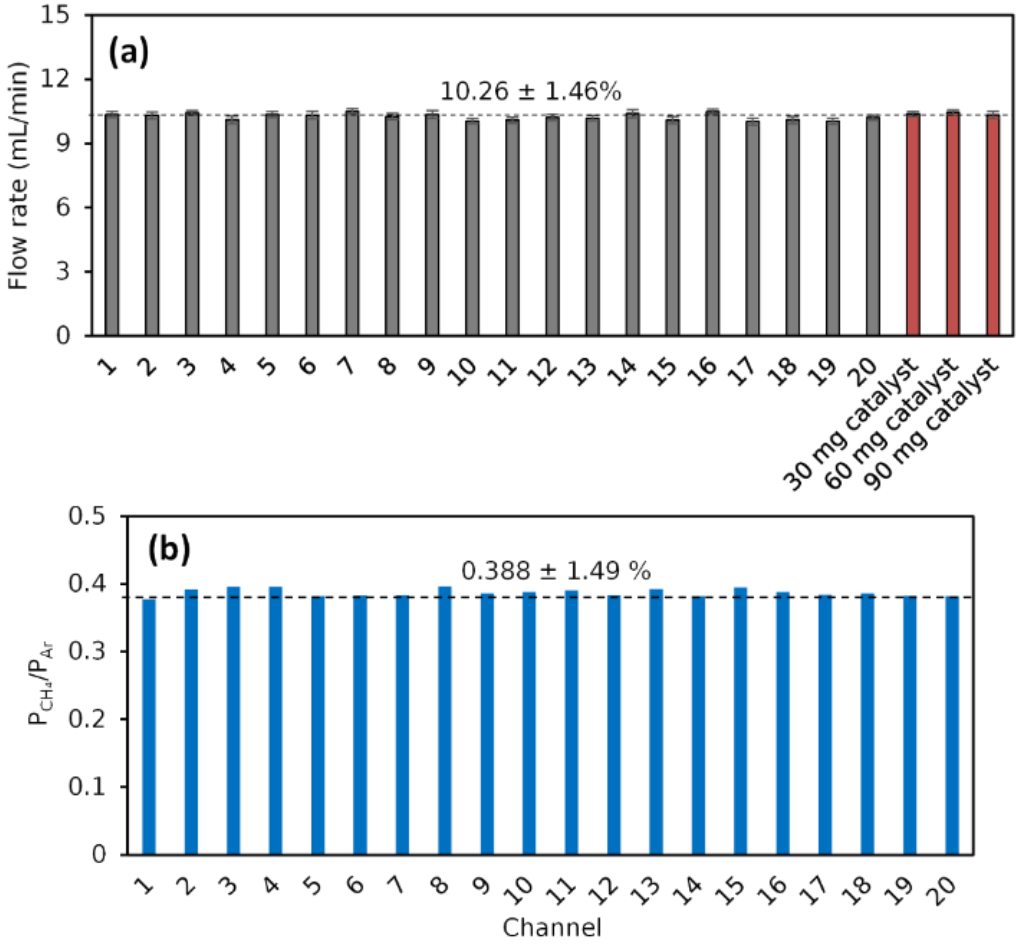

Figure 2.4. Validation of (a) gas distribution and (b) relative pressure determination in the HTS system.

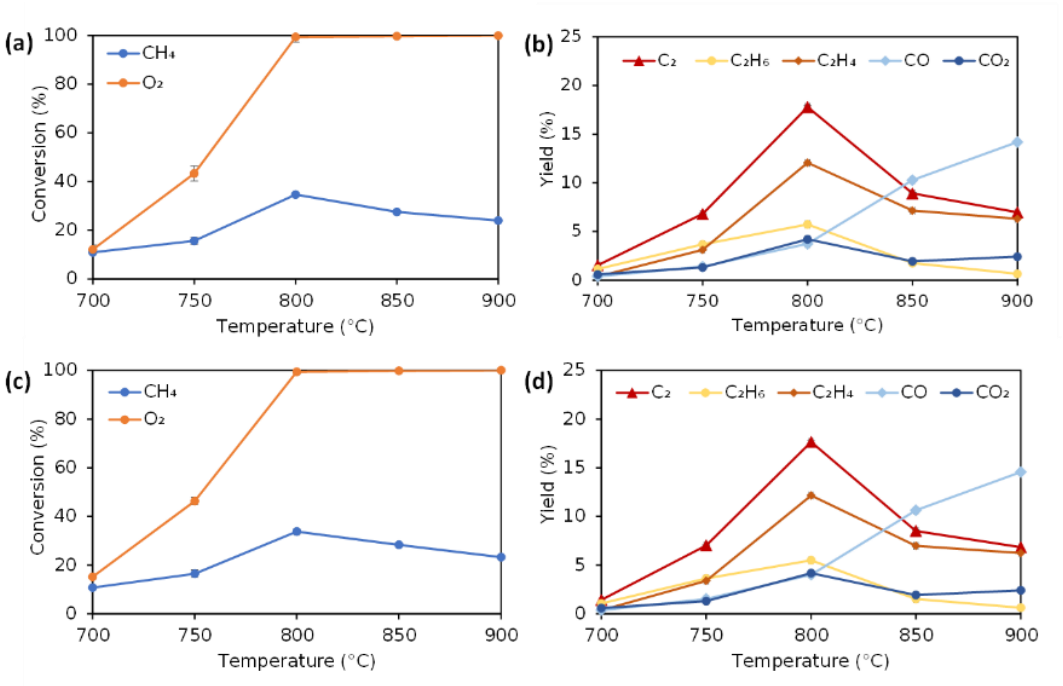

Figure 2.5. Confirmation on the reproducibility of catalytic tests: (a,b) channel 1 and (c,d) channel 2 using Mn-Na_2WO_4/SiO_2 as a catalyst. Ar_Flow/CH4_Flow/O2_Flow = 6/18/6 mL/mL/mL

Figure 2.6 summarizes the programmed sequence of reaction conditions employed in this chapter. Once catalysts are activated at 1000 °C for 160 minutes under O_2, the temperature is stepwise declined from 900 to 850, 800, 775, 750, and 700 °C. At each temperature, the total flow volume (10, 15, 20 mL/min/channel), the CH_4/O_2 ratio (2, 3, 4, 6 mol/mol), and the Ar concentration (P_{Ar} = 0.15, 0.40, 0.70 atm) are stepwise varied. One reaction condition is held for 6–7 min, which allows 2–3 rounds of sampling in the same condition for acquiring the error range of observations. The ascending temperature protocol was not employed as it causes excessive CO and CO_2 production due to the combustion of carbon deposits. The height of the catalyst bed was fixed at 10 mm, leading to a contact time of 0.75, 0.50, or 0.38 seconds at the given total flow volumes. Combined variations in the temperature, the total flow volume, the

CH_4/O_2 ratio, and the Ar concentration lead to 216 conditions per catalyst and 4320 observations for 20 catalysts in a single automated operation.

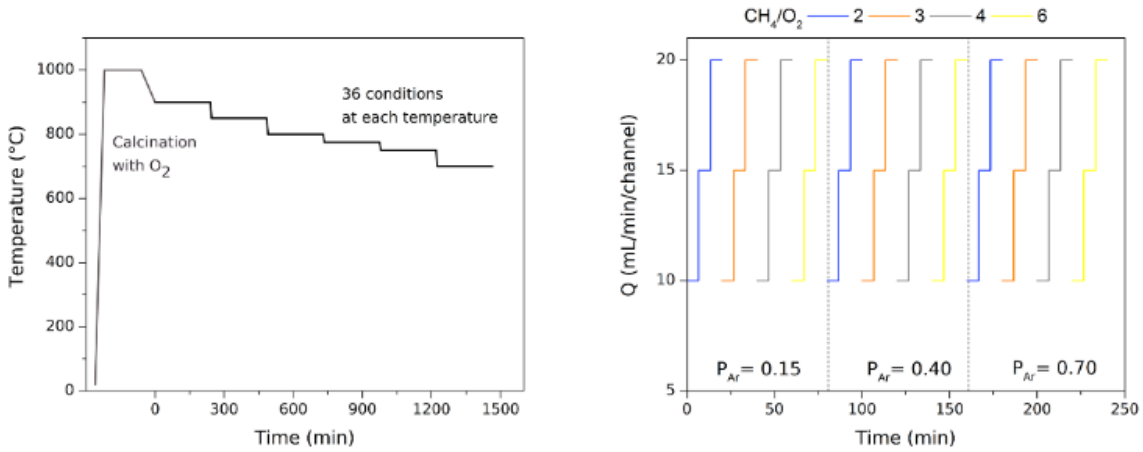

Figure 2.6. Employed programmed sequence of reaction conditions. Note that each temperature step includes a program for the gas flow volume and composition.

2.2.3. Data analysis

Evaluation of 40 catalysts and 19 references under 216 conditions generated an OCM dataset comprised of 12708 data (36 data were lost for Na/SiO_2 at 900 °C due to an experimental mistake). The size of the dataset is one digit larger than hundreds in past HTS studies [23,24] and 1870 in the literature OCM dataset [11]. Moreover, it was acquired in a process-consistent manner, where good and poor catalysts were equally evaluated under the same series of conditions. The dataset relates a catalyst to its performance at a specific condition. A catalyst is described by 7 features: M1-M3, Support, M1-M3_mol, and M1-M3_mol%. The Mx_mol corresponds to the mole of Mx per gram of a support, while Mx_mol% corresponds to the relative atomic percentage of Mx in M1+M2+M3. A condition is represented by Temp (in degree Celsius), Total_flow (in mL/min), Ar_flow, CH4_flow, O2_flow, CT (contact time in

seconds), and CH4/O2 (the molar ratio). Performance is given by CH4_conv as well as the yield and selectivity values for each of major products, *e.g.* C2H6y and C2H6s. The dataset is uploaded in a web platform "Catalyst Acquisition by Data Science (CADS)" for shared usage (Figure 2.7).[19]

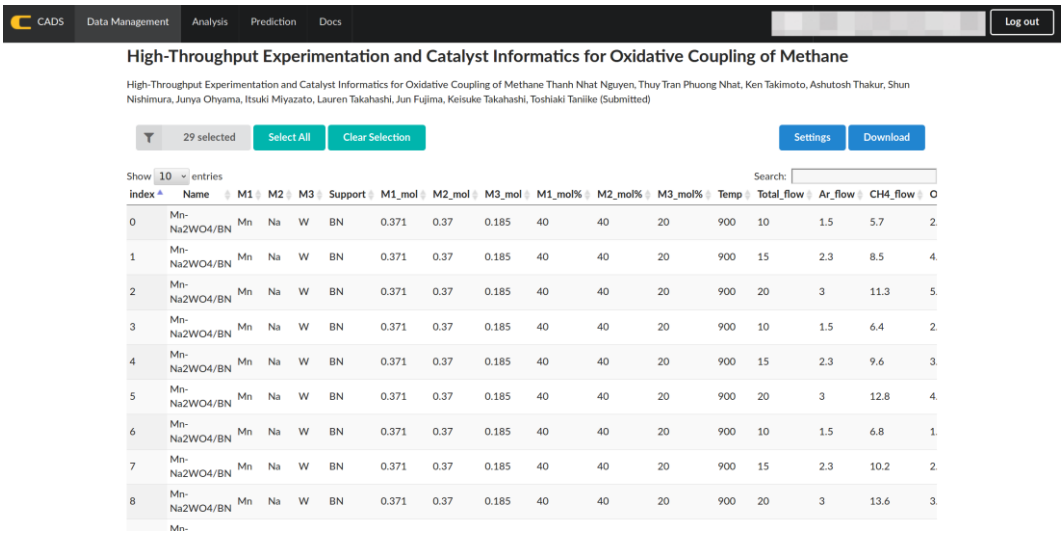

Figure 2.7. Snapshot of the OCM dataset uploaded in Catalyst Acquisition by Data Science (CADS) [19].

The dataset was preprocessed for data visualization and machine learning, where numerical variables were assigned for symbolic information such as atomic elements and supports. Regression models within supervised machine learning were used in order to predict the C_2 yield and selectivity of CO, CO_2, C_2H_4, and C_2H_6. In particular, both of linear and non-linear regression models were considered. Linear regression supervised machine learning, least squares linear regression (LSLR), support vector regression with linear kernel (SVRL), and kernel ridge (KR) while non-linear regression supervised machine learning, random forest regression (RFR), and support vector regression (SVR) with radial basis function (RBF) kernel, were implemented within scikit-learn [4]. Hyper parameters of KR, RFR, and SVR were also tuned. Note that the random state of RFR was fixed at the highest score in cross validation. C and

gamma in SVR were optimized and set to 10 and 0.01, respectively. Accuracy of the trained machine learning models was evaluated through cross validation, where the data was randomly split into 20% test and 80% trained data. The average scores of 10 randomly split test and trained data were taken and evaluated. All the data analysis was implemented under the guidance and supervision of Dr. Keisuke Takahashi, Hokkaido University, Japan.

2.3. Results and discussion

2.3.1. High-throughput experimentation and OCM dataset

A total of 12708 data points were obtained by executing three automated operations with the HTS instrument. This data is much larger in volume than the literature data of past 30 years [11]. Moreover, the performance of 59 catalyst entries including references was uniformly evaluated in each condition. A variety of qualitative tendencies are manifested by three-dimensional representation of the whole data based on scatter plots. For example, Figure 2.8a demonstrates the relationship between the CH_4 conversion and C_2 selectivity with the C_2 yield depicted in the color axis. The limitation of the C_2 yield caused by the tradeoff between the CH_4 conversion and C_2 selectivity is well known, but more clear trends are observed with the acquired dataset: Distribution of the CH_4 conversion and the C_2 selectivity limits the C_2 yield below 20–21%. The main factor of this restriction can be explained by analyzing the relationship between by-products and the C_2 yield. In Figure 2.8b, data points having high C_2 yield are distributed in a region of the CO selectivity of 0–40% and the CO_2 selectivity of 10–50%. Hence, the more fundamental problem is the formation of CO_2. Note that CO_2 production has an adverse effect on both the conversion and selectivity in a sense that it consumes the largest amount of O_2 per CH_4. This is further confirmed by the distribution of data points along reaction conditions. For example, CH_4 conversion is obviously dependent on the amount of O_2 (Figure 2.8c), where the upper limit of the CH_4 conversion is determined by the scarcity of O_2 due to undesired over-oxidation which consumes extra O_2. Temperature is also an important parameter (Figure 2.8d). High temperature favors high conversion and low selectivity due to the occurrence of over-oxidation. Although low temperature is preferred for high selectivity, the catalyst is not sufficiently active for the main reaction. Therefore, the middle range of

temperature is found to be suitable in terms of the tradeoff. In this way, the catalyst big data acquired by high-throughput experimentation is very powerful for quick overview of the general behavior of the catalytic reaction.

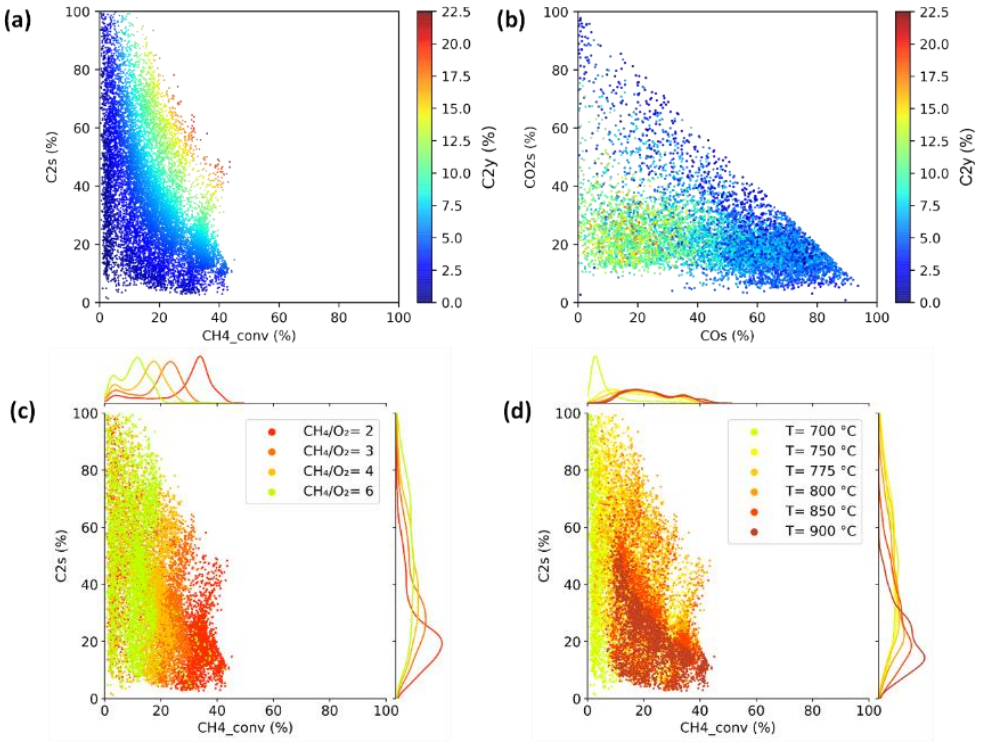

Figure 2.8. Visualization of 12708 data points based on scatter plots. (a) CH_4 conversion vs. C_2 selectivity and (b) CO selectivity vs. CO_2 selectivity with the C_2 yield indicated by color. Distribution of data points in terms of (c) the CH_4/O_2 ratio and (d) temperature.

Now, the dataset is subdivided to compare the performance of different catalysts. In past HTS research, the performance of OCM catalysts was measured at one or a few fixed condition [23,26]. Meanwhile, the dataset obtained here provides the performance of 59 catalysts over a sufficiently wide range of reaction conditions. One obvious profit of such a dataset is that the potential of different catalysts is fairly evaluated at respective sweet spots. Thus, the best C_2 yields of individual catalysts

(among 216 conditions) are compared in Figure 2.9. The corresponding conditions are listed in Table 2.2. Comparison is made in terms of supports, M2,3 metals, and M1 metals based on the formula of M1-$M2_{1\text{-}2}M3O_4$/support. In Figure 2.9a, bare supports hardly promoted the C_2 production as compared to blank, i.e. the gas-phase reaction between CH_4 and O_2. Improvement over the gas-phase reaction was attained by depositing Mn-Na_2WO_4 as the active phase, where the extent of the improvement was observed to be sensitive to the supports. In Figure 2.9b, the best C_2 yields are compared on the removal or the replacement of M2,3 metals in Mn-$M2_{1\text{-}2}M3O_4/SiO_2$. The removal of M2 or the utilization of non-alkali metals as M2 (except Mg) led to a dramatic deterioration in the C_2 yield. Meanwhile, the replacement of Na by other alkali metals or the replacement of W by Mo caused moderate deterioration. Figure 2.9c reports the alternation of M3. It was found that Mn and Ti are the only metals that can enhance the C_2 yield, i.e. other metals gave more or less deteriorated C_2 yields when compared to that of Na_2WO_4/SiO_2. It should be mentioned that Ti-Na_2WO_4/SiO_2 was never reported before at the best of my knowledge.

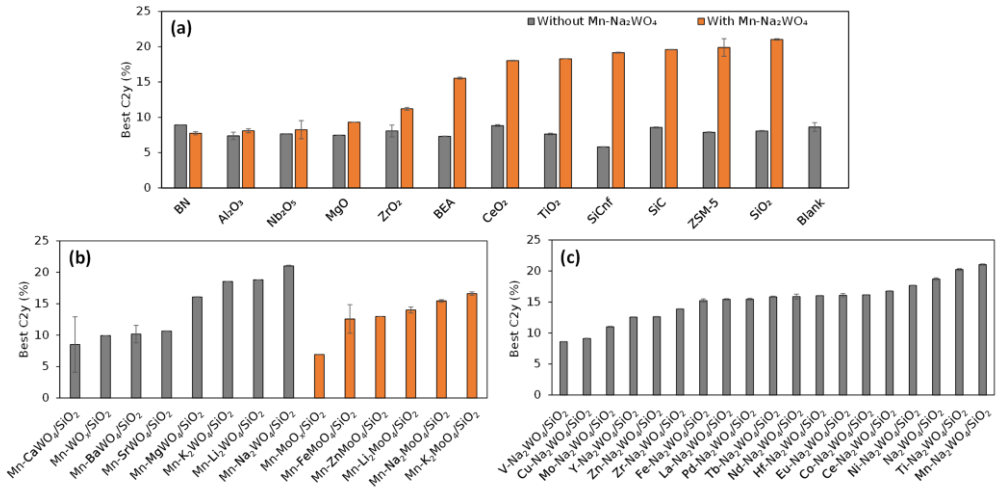

Figure 2.9. Best C_2 yield of individual catalysts: (a) Mn-Na_2WO_4/support, (b) Mn-$M2_{1\text{-}2}M3O_4/SiO_2$, and (c) M1-$Na_2WO_4/SiO_2$.

Table 2.2. List of the conditions corresponding to the best C_2 yield for individual catalysts.

Name	Temp (°C)	Total flow (mL/min)	CH_4/O_2 ratio (mol/mol)	P_{Ar} (atm)	CH_4 conversion (%)	C_2 yield (%)
Mn-Na_2WO_4/BN	800	15	3	0.15	20.8	7.8
Mn-Na_2WO_4/MgO	800	15	3	0.7	22.5	9.3
Mn-Na_2WO_4/Al_2O_3	750	20	3	0.15	22.7	8.1
Mn-Na_2WO_4/SiO_2	800	15	2	0.7	43.5	21
Mn-Na_2WO_4/SiC	800	15	3	0.7	31.5	19.6
Mn-Na_2WO_4/SiCnf	800	20	2	0.7	41.1	19.2
Mn-Na_2WO_4/BEA	800	20	3	0.7	28.4	15.6
Mn-Na_2WO_4/ZSM-5	800	20	3	0.7	30.9	19.9
Mn-Na_2WO_4/TiO_2	750	20	2	0.7	41.7	18.3
Mn-Na_2WO_4/ZrO_2	800	20	4	0.7	20.6	11.2
Mn-Na_2WO_4/Nb_2O_5	800	20	3	0.15	23.8	8.3
Mn-Na_2WO_4/CeO_2	775	10	2	0.7	38.8	18
Mn-Li_2WO_4/SiO_2	800	15	2	0.7	42.5	18.8
Mn-$MgWO_4$/SiO_2	775	15	2	0.7	38.3	16.1
Mn-K_2WO_4/SiO_2	775	10	2	0.7	39.4	18.6
Mn-$CaWO_4$/SiO_2	850	20	4	0.7	21.3	8.5
Mn-$SrWO_4$/SiO_2	850	20	4	0.7	24	10.7
Mn-$BaWO_4$/SiO_2	850	20	6	0.7	16.6	10.2
Mn-Li_2MoO_4/SiO_2	800	20	2	0.7	38.9	14
Mn-Na_2MoO_4/SiO_2	775	15	2	0.7	36.4	15.4
Mn-K_2MoO_4/SiO_2	800	20	3	0.7	26.9	16.6
Mn-$FeMoO_4$/SiO_2	850	20	6	0.7	18.5	12.6
Mn-$ZnMoO_4$/SiO_2	850	15	7	0.7	20	13
Ti-Na_2WO_4/SiO_2	800	10	2	0.7	43.5	20.2
V-Na_2WO_4/SiO_2	775	15	2	0.4	30.2	8.6
Fe-Na_2WO_4/SiO_2	800	10	2	0.7	38.4	15.2
Co-Na_2WO_4/SiO_2	850	20	3	0.7	30.5	16.1
Ni-Na_2WO_4/SiO_2	800	15	2	0.7	39.4	17.7
Cu-Na_2WO_4/SiO_2	800	20	2	0.4	32.2	9.1
Zn-Na_2WO_4/SiO_2	850	20	2	0.7	38.4	12.6
Y-Na_2WO_4/SiO_2	850	15	3	0.7	25.2	12.6
Zr-Na_2WO_4/SiO_2	800	10	2	0.7	37.2	13.9
Mo-Na_2WO_4/SiO_2	800	15	2	0.7	30.5	11
Pd-Na_2WO_4/SiO_2	800	10	2	0.7	36.8	15.5
La-Na_2WO_4/SiO_2	850	20	3	0.7	30.7	15.4
Ce-Na_2WO_4/SiO_2	800	10	2	0.7	40.3	16.8
Nd-Na_2WO_4/SiO_2	850	20	3	0.7	30.2	15.9
Eu-Na_2WO_4/SiO_2	850	20	2	0.7	40.8	16.1
Tb-Na_2WO_4/SiO_2	850	20	3	0.7	29	15.8
Hf-Na_2WO_4/SiO_2	850	20	2	0.7	39.3	16
Blank	775	20	2	0.4	23.8	8.6
BN	750	15	2	0.15	24.7	8.9
MgO	750	20	2	0.4	30.7	7.5
Al_2O_3	750	15	2	0.15	26.1	7.4
SiO_2	750	20	3	0.15	21.3	8.1
SiC	775	20	2	0.15	31.8	8.6
SiCnf	900	20	6	0.15	17.6	6.2
BEA	775	20	2	0.15	30.6	7.3
ZSM-5	750	20	2	0.4	25.4	7.9
TiO_2	850	20	3	0.15	23.1	7.6
ZrO_2	750	20	2	0.15	32.3	8.1
Nb_2O_5	700	10	2	0.4	21	7.7
CeO_2	775	20	3	0.15	21.4	8.8
Na_2WO_4/SiO_2	800	15	2	0.7	40.7	18.7
Mn-WO_x/SiO_2	850	15	7	0.7	15.9	9.9
Mn-MoO_x/SiO_2	850	20	3	0.15	21.6	6.9
Mn-Na/SiO_2	850	20	2	0.7	37.3	9.7
WO_x/SiO_2	775	20	2	0.4	20.7	7.2
Na/SiO_2	750	15	2	0.15	22.1	8.2

In Figure 2.9, I reached a known conclusion that Mn-Na_2WO_4/SiO_2 is the best OCM catalyst among M1-$M2_{1-2}M3O_4$/support, and its modification hardly improves the C_2 yield. Here, the validity of the observed tendencies is discussed based on past literature. The excellence of Mn-Na_2WO_4/SiO_2 has been ascribed to the synergistic combination of Mn-Na-W-Si [22,27]. The active site of this catalyst is tetrahedral WO_4^{2-} [27,28]. It goes up and down between W^{6+} and $W^{5+/4+}$ in the catalytic cycle involving homolytic dissociation of CH_4 and subsequent oxidation [22]. The primary role of Na or other alkali metal is at the stabilization of the tetrahedral WO_4^{2-} against octahedral one [29,30]. Mn of Mn_2O_3 mediates the O spillover to aid the recovery to W^{6+} [14,22,27,31]. Such cooperation of the two redox cycles at W and Mn promotes the OCM. The support exerts its influence by stabilizing tetrahedral WO_4^{2-}, where the cristobalite phase of SiO_2 is believed to be important [31,32]. The second role of Na is to facilitate the formation of the cristobalite phase at lower temperature, e.g. 800 °C, below typical calcination temperature [22,31–33]. Hence, the observed deterioration in performance due to the modification of Mn-Na_2WO_4/SiO_2 would be ascribed to a possibility that the modification caused a negative influence on the said mechanisms otherwise opposed the formation of the desired active phase. For instance, the poor performance of Mn-Na_2WO_4 on Al_2O_3, MgO, or ZrO_2 was attributed to the fact that these supports mediate the formation of poorly crystalline or undesired mixed oxides instead of preferred oxides [34]. Phase transition to α-cristobalite and the formation of the preferred oxides by high-temperature calcination were reported for catalysts supported on Si-based materials other than SiO_2 such as SiC and TS-1 zeolite [35,36]. The results of Figure 2.9a successfully discriminates these good and poor supports. Ji et al. studied the effect of substitution of Na in Mn-Na_2WO_4/SiO_2 with Li, K, Ba, Ca, Fe, Co, Ni, or Al, where the best performance was obtained for Na and K followed by

Li [29], which is consistent with Figure 2.9b. The deterioration in performance caused by the substitution of Na with alkaline earth or transition metals is ascribed to the inability of these metals to induce the low-temperature α-cristobalite formation as well as the formation of a significant amount of octahedral WO_6 in the form of $MnWO_4$ [14]. Anions of strong acid other than the best WO_4^{2-} such as MoO_4^{2-}, SO_4^{2-}, PO_4^{3-} have an ability to stabilize Mn_2O_3 on the catalysts, thus yielding reasonable OCM performance [14,22]. Finally, in relation to the earlier explained cooperative redox mechanism, Malekzadeh et al. found a correlation between the electrical conductivity and the C_2 yield for M1-Na_2WO_4/SiO_2 [31]. The C_2 yield followed the order of V < Zn < Fe < Co << Mn, showing agreement with the results of Figure 2.9c.

The dataset is also useful for discussing the process dependence of catalysts. Figure 2.10 compares the performance of the 40 catalysts and 19 reference materials at three representative conditions. The CH_4 conversion and C_2 selectivity are represented after being normalized to the corresponding values of Mn-Na_2WO_4/SiO_2 at the respective conditions. Among the three conditions, the best C_2 yield (20.88%) was obtained by Mn-Na_2WO_4/SiO_2 at 800 °C and the CH_4/O_2 ratio of 2 (Figure 2.10a). Indeed, the literature data for this catalyst has been reported around similar conditions [37]. Lower performance of the other catalysts is associated with both/either lower conversion and/or lower selectivity, while some catalysts showed comparable C_2 yields in the following two cases. i) Catalysts with comparable or even higher conversion: Mn-$M2_2WO_4/SiO_2$ (M2 = alkaline metal other than Na) and Mn-Na_2WO_4/Si-based supports (SiC, ZSM-5); ii) Catalysts with comparable C_2 selectivity: M1-Na_2WO_4/SiO_2 (M1 = none, Ti, Ni, Co). Interestingly, some M1 metals such as Nd, Eu, Hf, and Tb exhibited relatively high C_2 selectivity (though the conversion was low).

The performance ranking for the catalysts greatly differed when the O_2 concentration was reduced at the same temperature, i.e. 800 °C and the CH_4/O_2 ratio of 4 (Figure 2.10b). Mn-Na_2WO_4/SiO_2 was no longer the best catalyst at this condition (C2y = only 14.75%). Higher C_2 yields were obtained for Mn-Na_2WO_4 when immobilized on specific supports such as ZSM-5 (C2y = 19.40%), SiC (C2y = 17.17%), CeO_2 (C2y = 16.84%), and BEA (C2y = 15.44%). Mn-K_2WO_4/SiO_2 (16.46%) was also a reasonable catalyst. Based on the comparison at the two conditions, an important suggestion is derived: Mn-Na_2WO_4/SiO_2 has an ability to retain high C_2 selectivity at a higher O_2 concentration, but the conversion sharply drops at a lower concentration. On the other hand, the performant catalysts at the CH_4/O_2 ratio of 4 correspond to the catalysts which are less C_2 selective but relatively good in the conversion at the CH_4/O_2 ratio of 2. It is considered that the high activity of these catalysts could be effectively utilized to enhance the C_2 yield when operated at a milder condition (in other words, these catalysts tend to lose the C_2 selectivity at a more severe condition). This idea is further confirmed in Figure 2.10c by lowering the temperature to 750 °C at the CH_4/O_2 ratio of 4. A few catalysts having high activity were definitely advantageous at this condition: Mn-Na_2WO_4 supported on ZSM-5 (C2y = 18.76%), SiC (C2y = 16.17%), and BEA (C2y = 14.64%) in contrast to 5.14% for Mn-Na_2WO_4/SiO_2. Thus, analysis of the dataset proves that the performance of Mn-Na_2WO_4 is sensitive to the modification of Si-based supports in terms of the low-temperature activation of CH_4 and the selectivity tolerance against a high O_2 concentration. This finding is plausibly related to a past report, where Mn-Na_2WO_4/SBA-15 was superior to Mn-Na_2WO_4/SiO_2 at the condition of 750 °C and the CH_4/O_2 ratio of 4 [38]. However, including this example, the performance of OCM catalysts had been mostly compared at one condition in literature. To be important, the above-explained aspects which are useful

for catalyst design could be derived only by comparing the performance of different catalysts at multiple conditions.

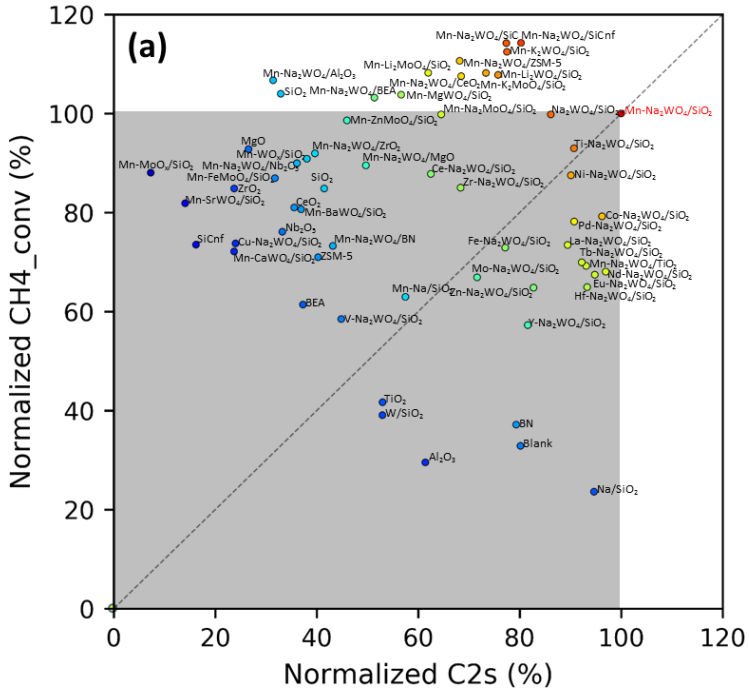

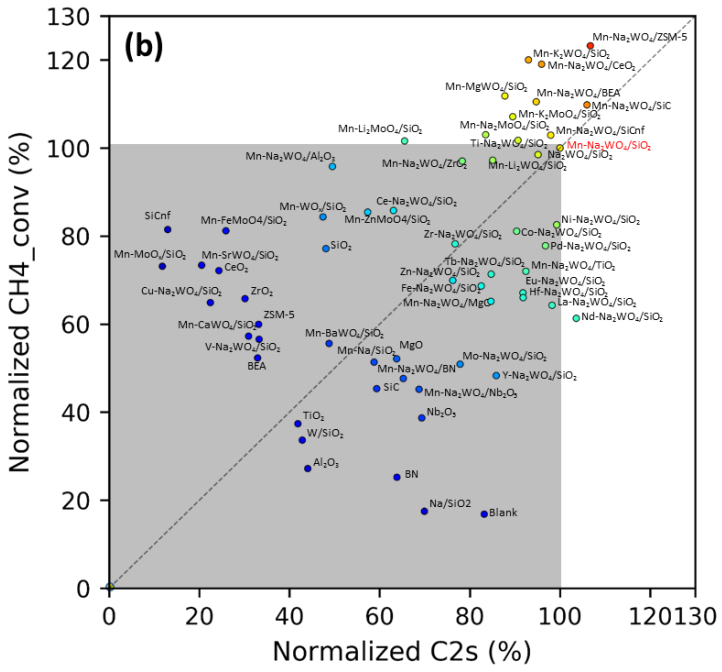

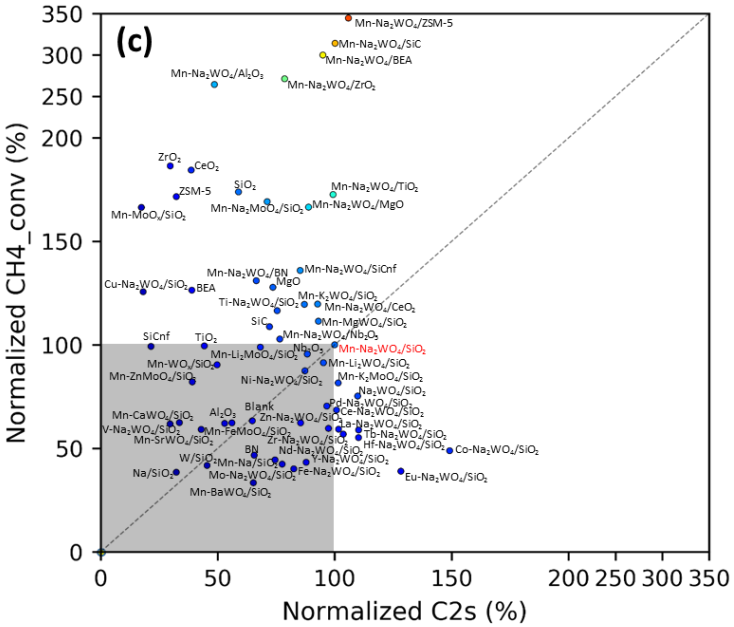

Figure 2.10. Process dependence of catalyst performance at (Temp, CH_4/O_2) = (a) (800 °C, 2 mol/mol), (b) (800 °C, 4 mol/mol), and (c) (750 °C, 4 mol/mol). The total flow volume and the partial pressure of Ar are set at 20 mL/min and 0.70 atm, respectively. The CH_4 conversion and the C_2 selectivity are normalized to those of Mn-Na_2WO_4/SiO_2 at the identical conditions: (CH4_conv, C2s) = (35.96%, 58.06%) at (800 °C, 2 mol/mol), (21.22%, 69.51%) at (800 °C, 4 mol/mol), and (7.88%, 65.23%) at (750 °C, 4 mol/mol).

It was earlier seen that the limited C_2 yield mainly comes from the CO_2 by-production (Figure 2.8b). Meanwhile, the electric furnace of the HTS instrument consists of three temperature zones (T_1: inlet, T_2: catalyst bed, T_3: outlet). The three temperatures can be independently set if the temperature difference of neighboring zones does not exceed 100 °C. In an attempt to optimize the three temperatures, I found that the C_2 yield was improved when $T_{1,3}$ (especially T_1) were lowered with respect to T_2 (Figure 2.11). This fact suggests that the C_2 yield is sensitive to the suppression of

non-selective oxidation in the gas phase [9,10,36] and may explain why the literature data is largely distributed among different groups.

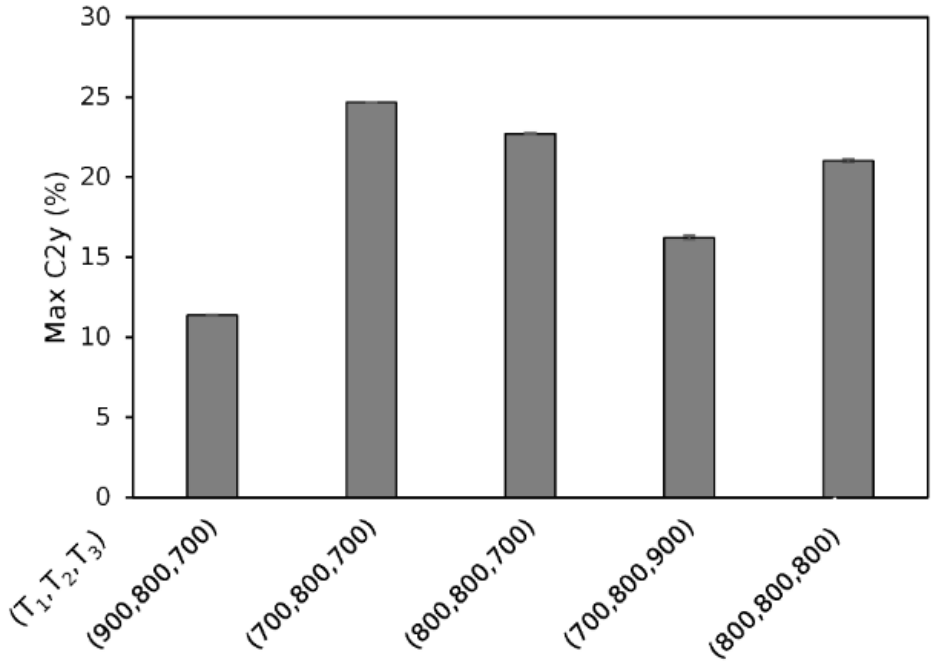

Figure 2.11. Dependence of the C_2 yield on the temperature protocol. T_2 was fixed at 800 °C, while T_1 and T_3 were independently varied. The C_2 yield was optimized in terms of the total flow (Q), the Ar pressure (P_{Ar}) and the CH_4/O_2 ratio using Mn-Na_2WO_4/SiO_2 as the catalyst.

According to the above result, the performance of selected 20 catalysts was re-evaluated in 216 conditions, where $T_{1,3}$ was set equal to T_2−100 °C. The results are summarized in Figure 2.12a. By suppressing the gas-phase reaction, the upper boundary line of the C_2 yield shifted from *ca.* 21% to *ca.* 26% (Figure 2.12a). The best C_2 yield was updated from 21.03% for Mn-Na_2WO_4/SiO_2 to 25.84% for Mn-Na_2WO_4/SiC. The best C_2 yield is compared between the original isothermal and new non-isothermal conditions for individual catalysts (Figure 2.12b). One can see that the new condition

does not necessarily upgrade all the catalysts, and the presence of Mn is essential for the upgrade. Indeed, lower temperature of the inlet (T_1) likely reduces the CH_4 conversion by suppressing the initial radical formation (CH_3•) [22,39]. The C_2 yield would not be improved unless the CH_4 conversion was maintained and/or the deterioration was overcome by the C_2 selectivity. The role of Mn was investigated by comparing scatter plots in the absence and presence of Mn (Figure 2.13), where the data points are restricted over 10% of the C_2 yield for visibility. Without Mn, high C_2 yield was obtained over the CH_4 conversion of 40% for the isothermal condition, while data points of high C_2 yield were concentrated in a region of the CH_4 conversion of 36–39% and the C_2 selectivity of 51–54% for the non-isothermal condition. The improvement in the C_2 selectivity was thus compensated by lower CH_4 conversion in the absence of Mn. The deterioration of CH_4 conversion in the non-isothermal condition was hardly observed in the presence of Mn. In this case, data points of high C_2 yield were distributed around the CH_4 conversion of 38–44% and the C_2 selectivity of 55–60%. It is clear that Mn promotes the activation of CH_4 as well as its selective oxidation. Lastly, the best C_2 yields of top 6 catalysts were identified in a very narrow range (18.80–21.03%) in the isothermal condition, and the use of the non-isothermal condition expanded the span to 20.05–25.84%. The suppression of the gas-phase reaction raised the impact of the catalyst design, and this in turn dictated the importance of simultaneous optimization of the catalyst and reactor design in OCM.

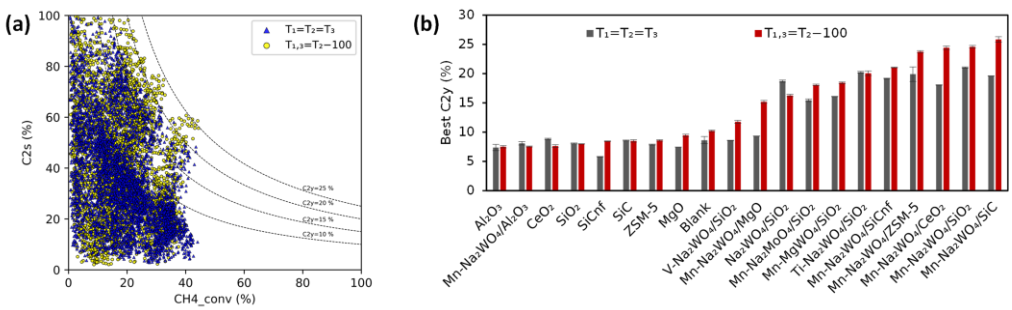

Figure 2.12. Comparison between two temperature protocols: (a) Scatter plot and (b) best C2 yield of individual catalysts.

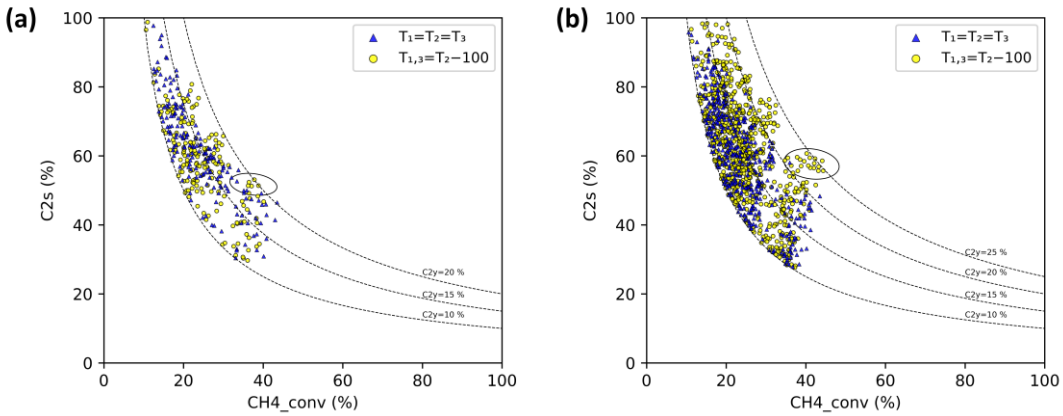

Figure 2.13. Role of Mn in OCM. Scatter plots are compared in the (a) absence and (b) presence of Mn for two temperature protocols, where the data points are limited based on the C_2 yield > 10%. The circled areas provide relatively high C_2 yield in the non-isothermal temperature protocol.

2.3.2. Machine learning

Linear and non-linear regression analysis was implemented for predicting the C_2 yield and the selectivity of CO, CO_2, C_2H_4, and C_2H_6. 11 descriptors were employed for each model: 7 features related to the catalyst design (M1_atom_number, M2_atom_number, M3_atom_number, Support_ID, M1_mol, M2_mol, M3_mol) and 4 features related to experimental process conditions (Temp, Ar_flow, CH4_flow, O2_flow). Here, the goal of the machine learning is to reveal how catalyst design and process conditions affect the yield and the selectivity of OCM. The cross validation scores for predicting the C_2 yield and the selectivity of CO, CO_2, C_2H_4, and C_2H_6 using the 11 descriptors are collected in Table 2.3. It was demonstrated that the C_2 yield can

be well predicted using RFR with a cross validation score of 0.88 and moderately predicted with SVR, leading one to consider that the prediction of the C_2 yield is a non-linear matter. True and predicted C_2 yields using RFR are visualized in Figure 2.14. Here, the test data is well predicted, whereas any of the regression models are unable to do so when implemented on literature OCM data collected from the past 30 years [11,12]. The importance of 11 descriptors for predicting the C_2 yield in RFR is summarized in Figure 2.14. The importance was determined by reviewing the generated decision trees in order to determine descriptor prominence and frequency throughout the decision process. It was found to be consistent with experimental observations.

Table 2.3. Cross validation scores for predicting the C_2 yield and the selectivity of CO, CO_2, C_2H_4, and C_2H_6 using 11 descriptors and 5 different machine learnings.

Objective variable	LSLR	SVRL	KR	RFR[a]	SVR[b]
C2y	0.16	−0.15	0.16	0.88	0.66
COs	0.55	0.21	0.45	0.84	0.72
CO2s	0.09	−0.68	−0.01	0.8	0.22
C2H4s	0.24	−1.38	0.22	0.7	0.5
C2H6s	0.59	−0.37	0.2	0.79	0.7

[a] The number of trees were set to 100.
[b] C and gamma were optimized and set to 10 and 0.01, respectively.

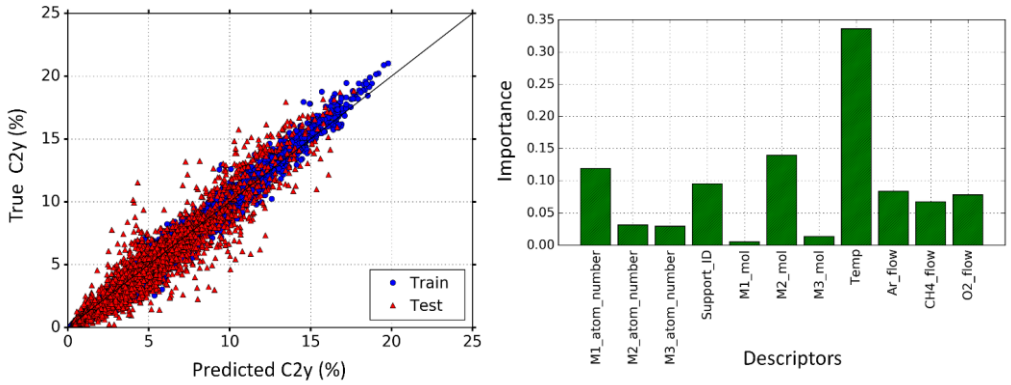

Figure 2.14. True and predicted C_2 yields using RFR and the importance of corresponding 11 descriptors in RFR.

The scarcity of poor data constitutes one of the major problems of literature data for machine learning. Here, additional random forest regression was performed, where poor data corresponding to the C_2 yield below 10% were omitted during training. As seen in Figure 2.15, the omission of poor data during the training process results in overly optimistic or otherwise largely inaccurate predictions.

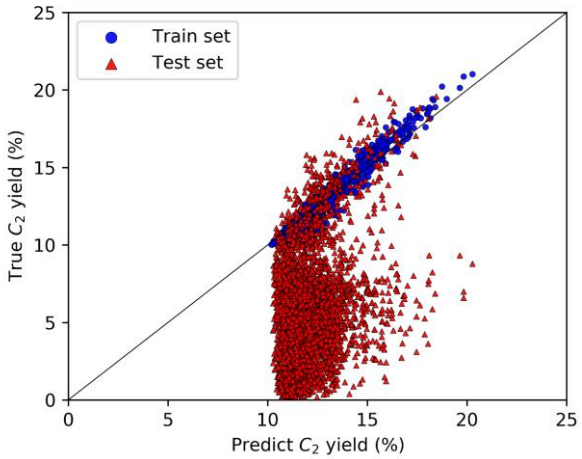

Figure 2.15. True and predicted C_2 yields using RFR when poor data (C_2 yield < 10%) is omitted during training. The score for the test set is −3.49. It must be noted that poor data cannot be predicted when only good data are used for the training.

The OCM data generated by the high-throughput experimentation produced a highly dispersed and consistent dataset, thereby resulting in the ability to apply regression models. The selectivity of CO, CO_2, C_2H_4, and C_2H_6 was also predicted using RFR and SVR with the same 11 descriptors, as shown in Table 2.3. Overall, RFR resulted in a higher cross validation score when compared to SVR. More importantly,

one can see that the selectivity of CO and C_2H_6 exhibited a higher score than that of CO_2 and C_2H_4, particularly for the results produced using SVR. This suggests that the catalyst and process conditions more directly affect the selectivity of CO and C_2H_6. On the other hand, the selectivity of CO_2 and C_2H_4 could be considered to be more involved with other factors. From this, machine learning implied the order of reactions, where CO and C_2H_6 has a more direct relation with the initial conditions while CO_2 and C_2H_4 are more indirectly affected by such conditions. This implication likely agrees with the proposed OCM reaction mechanism reported using microkinetic analysis: C_2H_6 is produced by CH_3•, followed by dehydrogenation to form C_2H_4 [39].

The power of machine learning lies in interpolation filling using a trained machine. Here, trained RFR with 11 descriptors are used to map out how the C_2 yield changes by experimental process conditions. Figure 2.16a is the surface plot of the CH_4/O_2 ratio and temperature against the C_2 yield, where the 24 actual data points are extracted for Mn-Na_2WO_4/SiO_2 at the total flow (Q) of 20 mL/min and the Ar pressure of 0.40 atm. Figure 2.16a shows a discreetness of data points, meaning that the optimum CH_4/O_2 ratio and temperature remain inaccurately determined for maximizing the C_2 yield. Then, interpolation filling of experimental conditions was performed using RFR that was trained for a full set of data. As shown in Figure 2.16b, the interpolation filling made the surface plot much smoother. The accuracy of the interpolation filling was primarily assured in Figure 2.14, and further validated by comparing the surface plot with 15 data points acquired from separate experiments for the same catalyst [40], where the newly added data points clearly matched with the trends given by RFR. Similar interpolation filling of how the flow of Ar, CH_4, and O_2 impacts the C_2 yield is performed for Mn-Na_2WO_4/SiO_2 at 800 °C. The predicted scatter plot of the flow of the three gases against the C_2 yield displays the sensitivity of the C_2 yield to the flow of Ar

and O_2 (Figure 2.17). Higher Ar flow (i.e. shorter contact and more dilution) and an optimal O_2 flow range between 2 and 3 are found to be preferred. Data science provides a means of unveiling trends within data which can then act as guides and provide hints when attempting to design catalysts. Figure 2.18 shows the predicted performance of M1-Na_2WO_4/SiO_2 catalysts, where the atomic number of M1 is varied from 22 to 72 with the exception of non-metals. The C_2 yield is predicted along the temperature while the other conditions are fixed as (Q, CH_4/O_2, P_{Ar}) = (20 mL/min, 2 mol/mol, 0.40 atm). Mn is found to exhibit the highest C_2 yield at 800 °C, which is in accordance to the original data. Interestingly, heavy elements, lanthanoids in particular, are predicted to result in a high C_2 yield at a higher temperature. These results suggest that the combination of high-throughput experimentation and machine learning allows for the prediction of catalysts and process conditions simultaneously.

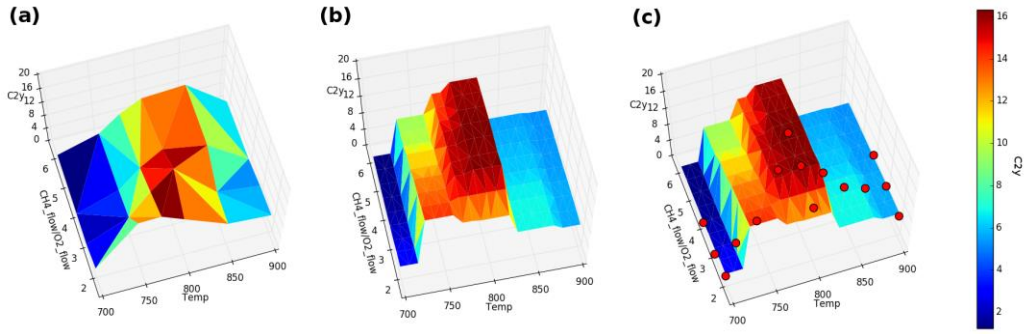

Figure 2.16. Surface plot of the CH_4/O_2 ratio and temperature against the C_2 yield for Mn-Na_2WO_4/SiO_2: (a) Actual data points, (b) interpolation filling by RFR, and (c) validation with separate experimental data points. Color bar indicates the C_2 yield (C2y) in %.

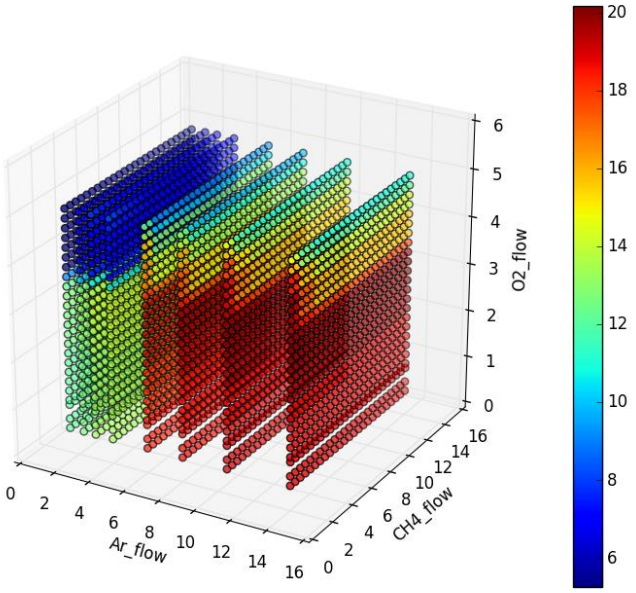

Figure 2.17. Predicted scatter plot of the flow of Ar, CH_4, and O_2 against the C_2 yield for Mn-Na_2WO_4/SiO_2 at 800 °C. Color bar indicates the C_2 yield (C2y) in %.

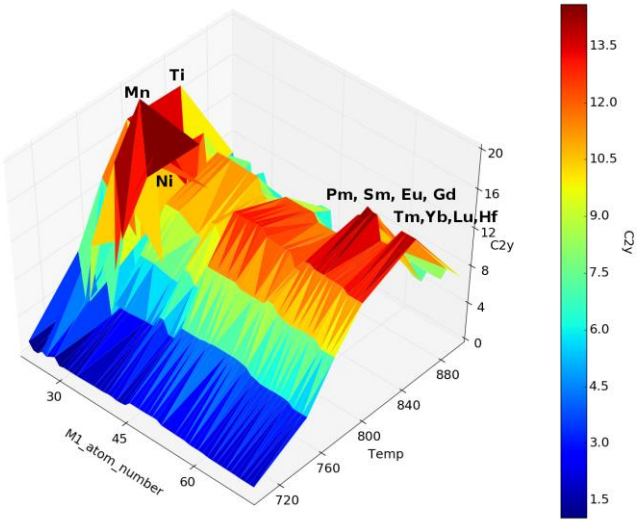

Figure 2.18. Predicted C_2 yield for M1-Na_2WO_4/SiO_2 catalysts at different temperatures. Color bar indicates the C_2 yield (C2y) in %.

2.4. Conclusions

The presence of a catalyst dataset that covers a parametric space of materials and process conditions in a process-consistent manner is essential for the realization of catalyst informatics. In this chapter, a HTS instrument was developed and exploited for preparing such a dataset for OCM catalysis. The instrument enables an automatic performance evaluation of 20 catalysts at a series of predefined conditions in fixed bed reactors, affording a dataset comprised of 12708 data for 59 catalysts. Thus far, the performance of OCM catalysts has been compared at one or a few fixed conditions within literature reports. This has resulted in ambiguity regarding whether a catalyst itself is superior or the catalyst is more suited to the employed condition. Importantly, OCM catalysts are sensitive to process conditions owing to competition between the activation of inert CH_4 and excessive oxidation, while different catalysts have their own sweet spots for peak performance. In this sense, I successfully demonstrated the usefulness of a dataset that covers a parametric space in terms of both catalysts and process conditions for overviewing the catalysis itself based on scatter plots, understanding process dependence of individual catalysts, and eventually acquiring how to improve catalysts and processes in a cooperative manner. Important findings are summarized below.

i) The restriction of C_2 yield comes from the tradeoff between the CH_4 conversion and C_2 selectivity, where the by-production of CO_2 is most detrimental.

ii) The comparison of the best C_2 yield among different catalysts has confirmed the superiority of a synergetic combination among Mn-Na-W-Si.

iii) The OCM reaction is generally sensitive to the process conditions, and catalyst design has a great impact on the process dependence. In particular, the modification of Si-based support affects the performance of Mn-Na_2WO_4 in terms of the low-temperature activation of CH_4 and the selectivity tolerance against high O_2 concentration.

iv) The combination of support modification for activity improvement and suppression of the gas phase reaction based on non-isothermal temperature control was found to be promising for upgrading the supported Mn-Na_2WO_4 system.

v) Combining the HTS data and regression in machine learning, accurate prediction of the C_2 yield becomes achievable via interpolation filling. The non-linear nature of the model suggests intrinsic complexity of OCM reaction.

vi) The supervised machine learning regression model was successfully implemented using the consistent HTS data, where previous efforts had failed when applied towards 1869 OCM data gathered from literature [12].

Based on all given demonstrations and achievements, I believe that the present contribution constitutes an importance piece of progress towards the implementation of catalyst informatics.

References

[1] Takahashi, K.; Takahashi, L.; Miyazato, I.; Fujima, J.; Tanaka, Y.; Uno, T.; Satoh, H.; Ohno, K.; Nishida, M.; Hirai, K.; Ohyama, J.; Nguyen, T. N.; Nishimura, S.; Taniike, T., The Rise of Catalyst Informatics: Towards Catalyst Genomics. ChemCatChem 2019, 11, 1146-1152.

[2] Ramprasad, R.; Batra, R.; Pilania, G.; Mannodi-Kanakkithodi, A.; Kim, C., Machine Learning in Materials Informatics: Recent Applications and Prospects. Npj Comput. Mater. 2017, 3, 54.

[3] Agrawal, A.; Choudhary, A., Perspective: Materials Informatics and Big Data: Realization of the "Fourth Paradigm" of Science in Materials Science. APL Mater. 2016, 4, 053208.

[4] Pedregosa, F.; Varoquaux, G.; Gramfort, A.; Michel, V.; Thirion, B.; Grisel, O.; Blondel, M.; Prettenhofer, P.; Weiss, R.; Dubourg, V.; Vanderplas, J.; Passos, A.; Cournapeau, D.; Brucher, M.; Perrot, M.; Duchesnay, É., Scikit-learn: Machine Learning in Python. J. Mach. Learn. Res. 2011, 12, 2825.

[5] Schütt, K. T.; Kessel, P.; Gastegger, M.; Nicoli, K. A.; Tkatchenko, A.; Müller, K. R., Schnetpack: A Deep Learning Toolbox for Atomistic Systems. J. Chem. Theory Comput. 2019, 15, 448-455.

[6] Takahashi, K.; Tanaka, Y., Materials Informatics: A Journey Towards Material Design and Synthesis. Dalton Trans. 2016, 45, 10497-10499.

[7] Schmidt, J.; Marques, M. R. G.; Botti, S.; Marques, M. A. L., Recent Advances and Applications of Machine Learning in Solid-State Materials Science. Npj Comput. Mater. 2019, 5, 83.

[8] Taniike, T.; Funako, T.; Terano, M., Multilateral Characterization for Industrial Ziegler–Natta Catalysts toward Elucidation of Structure–Performance Relationship. J. Catal. 2014, 311, 33-40.

[9] Sun, J.; Thybaut, J. W.; Marin, G. B., Microkinetics of Methane Oxidative Coupling. Catal. Today 2008, 137, 90-102.

[10] Kondratenko, E. V.; Peppel, T.; Seeburg, D.; Kondratenko, V. A.; Kalevaru, N.; Martin, A.; Wohlrab, S., Methane Conversion into Different Hydrocarbons or Oxygenates: Current Status and Future Perspectives in Catalyst Development and Reactor Operation. Catal. Sci. Technol. 2017, 7, 366-381.

[11] Zavyalova, U.; Holena, M.; Schlögl, R.; Baerns, M., Statistical Analysis of Past Catalytic Data on Oxidative Methane Coupling for New Insights into the Composition of High-Performance Catalysts. ChemCatChem 2011, 3, 1935-1947.

[12] Takahashi, K.; Miyazato, I.; Nishimura, S.; Ohyama, J., Unveiling Hidden Catalysts for the Oxidative Coupling of Methane Based on Combining Machine Learning with Literature Data. ChemCatChem 2018, 10, 3223-3228.

[13] Liu, H.; Wang, X.; Yang, D.; Gao, R.; Wang, Z.; Yang, J., Scale up and Stability Test for Oxidative Coupling of Methane over Na_2WO_4-Mn/SiO_2 Catalyst in a 200 mL Fixed-Bed Reactor. J. Nat. Gas Chem. 2008, 17, 59-63.

[14] Hou, S.; Cao, Y.; Xiong, W.; Liu, H.; Kou, Y., Site Requirements for the Oxidative Coupling of Methane on SiO_2-Supported Mn Catalysts. Ind. Eng. Chem. Res. 2006, 45, 7077-7083.

[15] Kondratenko, E. V.; Schlüter, M.; Baerns, M.; Linke, D.; Holena, M., Developing Catalytic Materials for the Oxidative Coupling of Methane through Statistical Analysis of Literature Data. Catal. Sci. Technol. 2015, 5, 1668-1677.

[16] Jia, X.; Lynch, A.; Huang, Y.; Danielson, M.; Lang'at, I.; Milder, A.; Ruby, A. E.; Wang, H.; Friedler, S. A.; Norquist, A. J.; Schrier, J., Anthropogenic Biases in Chemical Reaction Data Hinder Exploratory Inorganic Synthesis. Nature 2019, 573, 251-255.

[17] Maier, W. F.; Stöwe, K.; Sieg, S., Combinatorial and High-Throughput Materials Science. 2007, 46, 6016-6067.

[18] Hagemeyer, A.; Strasser, P.; Volpe, A. F., Jr., Eds. High Throughput Screening in Catalysis; Wiley-VCH: Weinheim, Germany, 2004.

[19] Catalyst Acquisition by Data Science [CADS] homepage https://cads.eng.hokudai.ac.jp/ [accessed September 13, 2019]. The dataset will be available to the public after the decision of publication.

[20] Wang, D. J.; Rosynek, M. P.; Lunsford, J. H., Oxidative Coupling of Methane over Oxide-Supported Sodium-Manganese Catalysts. J. Catal. 1995, 155, 390-402.

[21] Wang, J.; Chou, L.; Zhang, B.; Song, H.; Zhao, J.; Yang, J.; Li, S., Comparative Study on Oxidation of Methane to Ethane and Ethylene over Na_2WO_4-Mn/SiO_2 Catalysts Prepared by Different Methods. J. Mol. Catal. A: Chem. 2006, 245, 272-277.

[22] Arndt, S.; Otremba, T.; Simon, U.; Yildiz, M.; Schubert, H.; Schomäcker, R., Mn-Na_2WO_4/SiO_2 as Catalyst for the Oxidative Coupling of Methane. What Is Really Known? Appl. Catal., A. 2012, 425-426, 53-61.

[23] Olivier, L.; Haag, S.; Pennemann, H.; Hofmann, C.; Mirodatos, C.; van Veen, A. C., High-Temperature Parallel Screening of Catalysts for the Oxidative Coupling of Methane. Catal. Today 2008, 137, 80-89.

[24] Moehmel, S.; Steinfeldt, N.; Engelschalt, S.; Holena, M.; Kolf, S.; Baerns, M.; Dingerdissen, U.; Wolf, D.; Weber, R.; Bewersdorf, M., New Catalytic Materials for the High-Temperature Synthesis of Hydrocyanic Acid from Methane and Ammonia by High-Throughput Approach. Appl. Catal., A. 2008, 334, 73-83.

[25] Wang, H.; Liu, Z.; Shen, J., Quantified MS Analysis Applied to Combinatorial Heterogeneous Catalyst Libraries. J. Comb. Chem. 2003, 5, 802-808.

[26] Ras, E.-J.; Gomez-Quero, S., Oxidative Coupling of Methane in Small Scale Parallel Reactors. Top. Catal. 2014, 57, 1392-1399.

[27] Li, S.-B., Oxidative Coupling of Methane over W-Mn/SiO_2. Chin. J. Chem . 2001, 19, 16-21.

[28] Wu, J.; Li, S.; Niu, J.; Fang, X., Mechanistic Study of Oxidative Coupling of Methane over Mn_2O_3-Na_2WO_4/SiO_2 Catalyst. Appl. Catal., A. 1995, 124, 9-18.

[29] Ji, S.; Xiao, T.; Li, S.; Chou, L.; Zhang, B.; Xu, C.; Hou, R.; York, A. P. E.; Green, M. L. H., Surface Wo_4 Tetrahedron: The Essence of the Oxidative Coupling of Methane over M-W-Mn/SiO_2 Catalysts. J. Catal. 2003, 220, 47-56.

[30] Palermo, A.; Vazquez, J. P. H.; Lambert, R. M., New Efficient Catalysts for the Oxidative Coupling of Methane. Catal. Lett. 2000, 68, 191-196.

[31] Malekzadeh, A.; Dalai, A. K.; Khodadadi, A.; Mortazavi, Y., Structural Features of Na_2WO_4–MO_x/SiO_2 Catalysts in Oxidative Coupling of Methane Reaction. Catal. Commun. 2008, 9, 960-965.

[32] Palermo, A.; Vazquez, J. P. H.; Lee, A. F.; Tikhov, M. S.; Lambert, R. M., Critical Influence of the Amorphous Silica-to-Cristobalite Phase Transition on the Performance of $Mn/Na_2WO_4/SiO_2$ Catalysts for the Oxidative Coupling of Methane. J. Catal. 1998, 177, 259-266.

[33] Wu, J.; Li, S., The Role of Distorted WO_4 in the Oxidative Coupling of Methane on Supported Tungsten Oxide Catalysts. J. Phys. Chem. 1995, 99, 4566-4568.

[34] Elkins, T. W.; Hagelin-Weaver, H. E., Characterization of Mn–Na_2WO_4/SiO_2 and Mn–Na_2WO_4/MgO Catalysts for the Oxidative Coupling of Methane. Appl. Catal., A. 2015, 497, 96-106.

[35] Wang, H.; Schmack, R.; Paul, B.; Albrecht, M.; Sokolov, S.; Rümmler, S.; Kondratenko, E. V.; Kraehnert, R., Porous Silicon Carbide as a Support for Mn/Na/W/SiC Catalyst in the Oxidative Coupling of Methane. Appl. Catal., A. 2017, 537, 33-39.

[36] Wang, P.; Zhao, G.; Wang, Y.; Lu, Y., $MnTiO_3$-Driven Low-Temperature Oxidative Coupling of Methane over TiO_2-Doped Mn_2O_3-Na_2WO_4/SiO_2 Catalyst. Sci. Adv. 2017, 3, e1603180.

[37] Godini, H. R.; Gili, A.; Görke, O.; Arndt, S.; Simon, U.; Thomas, A.; Schomäcker, R.; Wozny, G., Sol–Gel Method for Synthesis of Mn–Na_2WO_4/SiO_2 Catalyst for Methane Oxidative Coupling. Catal. Today 2014, 236, 12-22.

[38] Yildiz, M.; Aksu, Y.; Simon, U.; Kailasam, K.; Goerke, O.; Rosowski, F.; Schomäcker, R.; Thomas, A.; Arndt, S., Enhanced Catalytic Performance of Mn_xO_y–Na_2WO_4/SiO_2 for the Oxidative Coupling of Methane Using an Ordered Mesoporous Silica Support. Chem. Commun. 2014, 50, 14440-14442.

[39] Karakaya, C.; Zhu, H.; Loebick, C.; Weissman, J. G.; Kee, R. J., A Detailed Reaction Mechanism for Oxidative Coupling of Methane over Mn/Na_2WO_4/SiO_2 Catalyst for Non-isothermal Conditions. Catal. Today 2018, 312, 10-22.

[40] Ohyama, J.; Nishimura, S.; Takahashi, K., Data Driven Determination of Reaction Conditions in Oxidative Coupling of Methane via Machine Learning. ChemCatChem 2019, 11, 1-8.

Chapter 3

Factors to influence low-temperature performance of supported Mn–Na_2WO_4 in oxidative coupling of methane

Abstract: The oxidative coupling of methane is an effective approach for directly upgrading methane to valuable products. Among known OCM catalysts, Mn–Na_2WO_4/SiO_2 is a promising candidate for an industrial application with superior catalytic performance and high stability. In the last chapter, I had found that the performance of Mn–Na_2WO_4 significantly depends on the choice of support materials. Here, a variety of Mn–Na_2WO_4 catalysts were prepared using different Si-based materials as supports. The OCM performance of these catalysts was evaluated by a high-throughput screening instrument that had been developed in the last chapter. The relationship between the catalyst performance and the choice of support materials was studied in detail on the basis of characterization using Raman spectroscopy, X-ray diffraction, elemental mapping, and X-ray photospectroscopy.

Keywords: Oxidative coupling of methane, Mn–Na_2WO_4, support materials, high-throughput screening, characterization.

3.1. Introduction

Owing to the enormous proven reverses of natural gas and the depleting reserves of crude oil, research interests have been focused on the development of technology towards selective conversion of methane into more valuable products [1,2]. Currently, methane is industrially transformed into methanol or higher hydrocarbons through stream reforming (to form a mixture of CO and H_2), followed by the Fisher-Tropsch process [3]. However, this transformation consists of multiple energy intensive processes [1,3]. Thus, one-step or direct conversion of methane to ethylene, methanol, and formaldehyde has been desired [3]. Among them, the oxidative coupling of methane (OCM) into C_2 products has been intensively studied over three decades [4]. The major challenge of this reaction arises from the fact that methane, comprised solely of weakly polarized C-H bonds, is extremely stable [5]. The C-H bond activation of methane requires a relatively high temperature as well as oxygen-rich atmosphere, resulting in undesired side reactions (e.g. complete combustion) [5,6]. This encompasses a tradeoff between the conversion and selectivity as an intrinsic nature of OCM and the main reason of unsuccessful industrialization. Hence, the development of novel OCM catalysts with a special emphasis on the conversion-selectivity tradeoff is an emerging task.

In an endeavor to find performant OCM catalysts, a number of catalysts have been reported in the past three decades. However, few catalysts could fulfill the C_2 yield over 30% (criteria for industrialization) in a fixed-bed reactor configuration [4]. So far, the best OCM catalysts could give 30–50% of the methane conversion and 40–80% of the C_2 selectivity, resulting in the C_2 yield from 18 to 25% [4,7]. Li/MgO, one of the most studied catalysts, tends to lose its activity in just a few hours on stream [8]. Mn–Na_2WO_4/SiO_2 is one of a few promising catalysts for OCM due to its good C_2 selectivity

and high stability [9]. Attempts to improve the performance of this ternary system have been hardly successful [9-11]. For example, substituion of Mn by other redox-active elements [12], substituion of Na by other alkaline or alkaline earth elements [9], replacement of WO_4^{2-} by other Lewis acidic anions [13], and utilization of other support materials [11,14] were found to lower the C_2 yield in most of cases, except when unusual conditions for Mn–Na_2WO_4/SiO_2 were adopted [5,15]. In chapter 2, I developed a high-throughput screening (HTS) instrument that automates the performance evaluation of 20 catalysts placed in parallel fixed-bed reactors at a predefined set of reaction conditions. The instrument was used to evaluate 40 catalysts that were derived from Mn–Na_2WO_4/SiO_2 [16]. In agreement with previous literature, any substitution did not largely upgrade the best C_2 yield of individual catalysts from that of Mn–Na_2WO_4/SiO_2. Contrary, by testing the catalysts in a wide range of conditions, it was newly found that the choice of supports largely changes the response of Mn–Na_2WO_4 to different reaction conditions, especially, in terms of low-temperature methane activation and C_2 selectivity tolerance to harsh conditions, i.e. two most important properties for coping with the conversion-selectivity tradeoff.

In this chapter, I report a subsequent research: Mn–Na_2WO_4 catalysts supported on 20 different Si-based materials were tested in a wide range of conditions using the above-mentioned HTS instrument. Their responses to the reaction conditions and the origin of different responses were studied with the aid of Raman spectroscopy, X-ray diffraction, elemental mapping based on scanning electron microscopy, and X-ray photoelectron spectroscopy. The mechanism of good activity at low temperature of some Si-based supports will elucidated, which promise a better performance for Mn–Na-W-Si system toward the industrial target.

3.2. Experimental

3.2.1. Materials

Metal precursors, manganese (II) nitrate (Wako) and sodium tungstate (Sigma-Aldrich), were used as received. In the last chapter, it was found that some types of Si-based supports showed superior performance under milder conditions. In order to explore better Si-based supports for the Mn–Na_2WO_4 as well as to obtain a mechanistic insight, several types of supports were selected here with variations in the pore size and shape, the amount of impurity (aluminum or titanium), the cation type, and the surface area. These supports are listed in Table 3.1. They were supplied from Tosoh Corporation, Japan Reference Catalyst (JRC) Committee of the Catalysis Society of Japan, ACS Material, Kanto Chemical Corporation, and Sigma-Aldrich.

Table 3.1. List of supports

Type	Name	Trade name	Pore size (Å)	Si/Al(Ti)[a] (mol/mol)	Cation type	S_{BET}[b] (m^2/g)
Al-Si zeolite	BEA(25)	JRC-Z-HB25	6.5	25	H^+	494
	BEA(28)	HSZ-930NHA	6.5	28	NH_4^+	590
	BEA(41)	HSZ-940NHA	6.5	41	NH_4^+	580
	BEA(42.2)	HSZ-941HOA	6.5	42.2	H^+	520
	BEA(104)	HSZ-960HOA	6.5	104	H^+	560
	BEA(150)	JRC-HB150	6.5	150	H^+	607
	BEA(440)	HSZ-980HOA	6.5	440	H^+	500
	BEA(1700)	HSZ-990HOA	6.5	1700	H^+	470
	ZSM(22.5)	HSZ-820NHA	5.8	22.5	NH_4^+	510
	ZSM(23.9)	HSZ-822HOA	5.8	23.9	H^+	330
	ZSM(37)	HSZ-840HOA	5.8	37	H^+	330
	ZSM(39)	HSZ-840NHA	5.8	39	NH_4^+	330
	ZSM(90)	JRC-Z5-90NA	5.8	90	Na^+	300
	ZSM(1880)	HSZ-891HOA	5.8	1880	H^+	310
	ZSM(2120)	HSZ-890HOA	5.8	2120	H^+	310
Ti-Si zeolite	TS-1	TS-1	5.0	80	n.a.	420
Mesoporous silica	SBA-15	SBA-15	60	n.a.	n.a.	>550
	MCM-41	MCM-41	45	n.a.	n.a.	1000
Silica gel	SiO_2	60N	60	n.a.	n.a.	650
Silicon carbine	SiC	SiC	n.a.	n.a.	n.a.	1.5

[a,b] The information of Si/Al ratio and surface area are taken from producers, where information from SiC was measured.

3.2.2. Catalyst preparation

The catalysts were prepared based on a co-impregnation method. A support powder (1.0 g) was impregnated with an aqueous solution (4–5 mL) containing $Mn(NO_3)_2 \cdot 6H_2O$ (0.345 mmol) and $Na_2WO_4 \cdot 2H_2O$ (0.269 mmol) at 50 °C in 6 hours. The product was dried at 110 °C, followed by calcination at 1000 °C for 3 hours. The theoretical amounts of the active components were 5.0 wt% for Na_2WO_4 and 2.0 wt% for Mn to the support.

3.2.3. Catalyst test

The OCM performance of catalysts was evaluated based on the high-throughput screening (HTS) instrument, which had been developed in the last chapter [16]. The instrument consists of a mixed gas generator, a flow distributor system, 20 reaction tubes, an electric furnace, an autosampler, and a quadrupole mass spectrometer (QMS). The gas mixer provides a gas mixture of $CH_4/O_2/Ar$ with the desired gas composition. The gas mixture is equally divided into 20 portions, and transferred to 20 reaction tubes made of quartz. A catalyst bed of 10 mm in height is set in the middle of each reaction tube with the aid of quartz wool. The 20 reaction tubes are placed symmetrically in a hollow electric furnace. The furnace consists of three temperature zones ($T_{1–3}$). Here, the temperature of the middle zone (T_2) was set 100 °C higher than the temperature of the upstream and downstream zones ($T_{1,3}$) in order to suppress less selective gas-phase reaction [16]. Effluent gas which comes out from the 20 reaction tubes is sequentially transferred to the sampling line, and then analyzed by QMS. The programmed sequence of reaction conditions is shown in Figure 3.1. The temperature was varied from 900 to 850, 800, 750, and 700 °C, and at each temperature, the total flow volume (Q = 10, 15,

and 20 mL/min/channel), the CH_4/O_2 ratio (2, 4, and 6 mol/mol), and the Ar concentration (P_{Ar} = 0.15, 0.40, 0.70 atm) were stepwise varied. The OCM performance of 20 catalysts was thus evaluated at 135 conditions in an automated fashion.

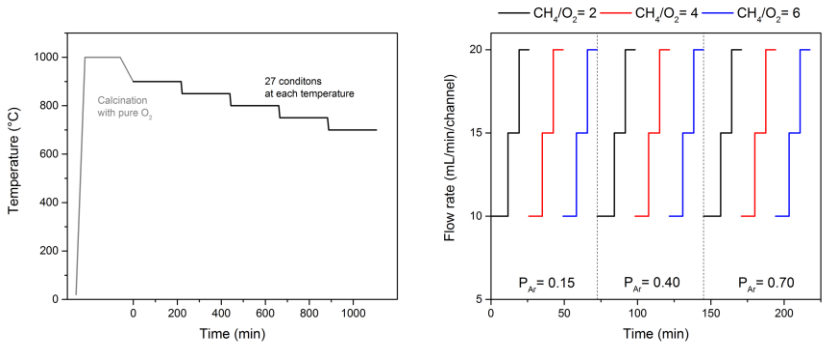

Figure 3.1. Employed programmed sequence of reaction conditions. Note that each temperature step includes a program for the gas flow volume and composition.

3.2.4. Catalyst characterization

Selected catalysts were characterized by several techniques. Raman spectra of the catalysts were recorded on a Laser Raman spectrometer (NRS-4100, JASCO) with a 532 nm laser. A polynomial method was used for background subtraction. Powder X-ray diffraction was performed (CuKα radiation, λ = 0.154 nm) on a SmartLab (Rigaku) X-ray diffractometer. The diffraction patterns were collected in the 2θ range of 5–40° with a step size of 0.008°. The surface morphology and elemental distribution of the catalysts were studied by scanning electron microscopy with energy dispersive X-ray spectroscopy (SEM-EDS). A small amount of a sample powder was placed on a carbon tape. The measurements were performed on a tabletop microscope (Hitachi TM 3030Plus, 15 kV) equipped with an EDS detector. The near surface chemical analysis was performed based on X-ray photoelectron spectroscopy (XPS, Kratos AXIS-Ultra DLD) using monochromatic Al-Kα radiation. The pass energy of the concentric

hemispherical analyzer was set at 40 eV. A narrow scan was recorded in 240 s with a step increment of 0.1 eV and repeated at least 5 times for each element. Powder samples were loaded on a sample holder through double-sided adhesive copper tape. The binding energies (BE) were calibrated using the C1s peak of surface hydrocarbons at 285.0 eV as the internal reference.

3.3. Results and discussion

3.3.1 Catalytic test

The OCM performance of 20 catalysts, comprising of Mn–Na_2WO_4 supported on different Si-based supports, were evaluated in 135 reaction conditions. The obtained 2700 data are represented in a scatter plot, where the relationship between the CH_4 conversion and the C_2 selectivity is displayed with the corresponding C_2 yield depicted in the color axis to understand a general behavior of catalyst performance (Figure 3.2). There was a boundary of limiting the CH_4 conversion and C_2 yield. The maximum CH_4 conversion and C_2 yield were respectively recorded at 47% and 25.6%, while the C_2 selectivity varied from 0 to 100%, which results in C_2 yield varied from 0-25 %.

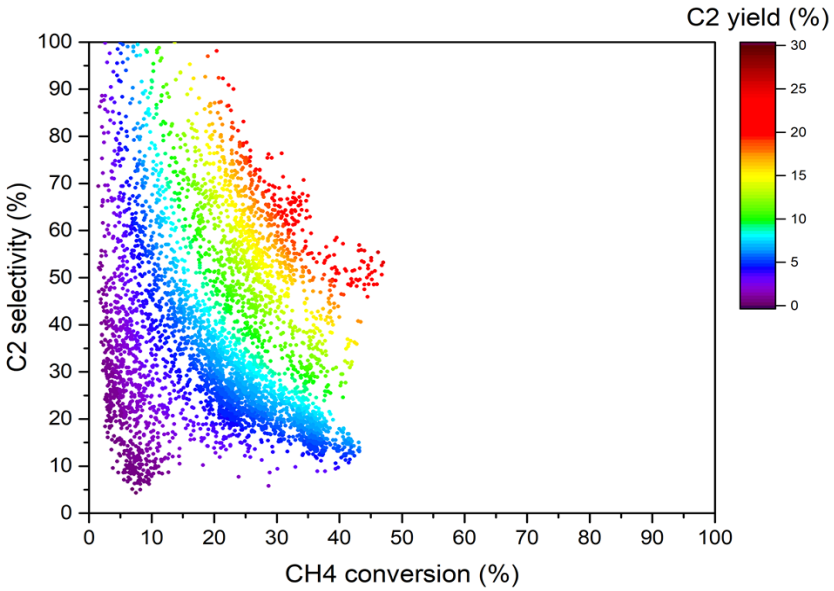

Figure 3.2. Visualization of 2700 data points based on a scatter plot for the CH_4 conversion and C_2 selectivity. The C_2 yield as their product is indicated by the color.

Next, I compare the impact of different Si-based supports on the OCM performance of the catalysts. For this, the color axis of the scatter plot in Figure 3.2 was

changed to various features of the supports, and then the Si/Al ratio was identified as the most impactful feature. This is shown in Figure 3.3a. It can be seen that the upper boundary of the C_2 yield becomes less than 10% for the supports having the Si/Al ratio lower than 50. The best C_2 yield of individual catalysts was compared in Figure 3.3b, and relevant data are listed in Table 3.2. These again confirmed the negative influence of using Al-rich zeolites as support materials. All of the catalysts using pure silica supports (SBA-15, MCM-41, SiO_2) and SiC exhibited high performance: 43–47% CH_4 conversion, 53–57% C_2 selectivity, and 24.3–25.6% C_2 yield, in agreement with the literature data [9-11,16], TS-1, a titanium-silicate zeolite, could also be a good support (23.4% C_2 yield) [5]. On the contrary, the performance of catalysts using aluminum silicate zeolites was greatly different, especially in relation to the variation in the Si/Al ratio. The performance became comparable to that of the pure silica when high-silica zeolites were employed, while the C_2 yield became less than 10% for Al-rich zeolites.

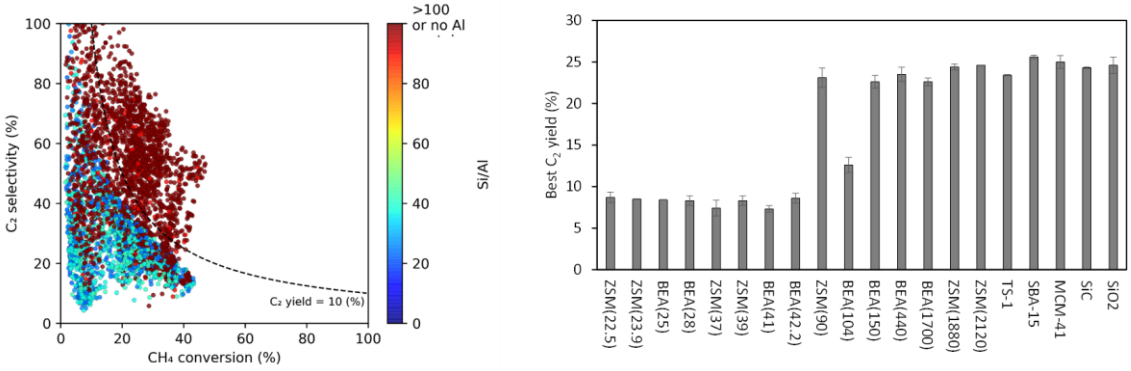

Figure 3.3. Catalyst performance among Mn–Na-W/Si-based supports with their impurity a) Scatter plot of all data with color map depicted Si/Al ratio, b) best C_2 yield of all catalysts.

Table 3.2. List of data corresponding to the best C_2 yield for individual catalysts.

Sample	C_2 yield (%)	CH_4 conv. (%)	C_2 sel. (%)	Temp. (°C)	Q (mL/min)	CH_4/O_2 (mol/mol)	P_{Ar} (atm)
ZSM(22.5)	8.7	33	26.4	800	20	2	0.4
ZSM(23.9)	8.5	27.6	30.9	800	20	2	0.7
BEA(25)	8.4	33.1	25.4	800	20	2	0.15
BEA(28)	8.3	31.5	26.3	800	20	2	0.4
ZSM(37)	7.4	34.5	21.5	800	20	2	0.15
ZSM(39)	8.3	26.3	31.6	800	20	2	0.7
BEA(41)	7.3	32.5	22.3	800	20	2	0.7
BEA(42.2)	8.6	30.5	28.2	800	20	2	0.4
ZSM(90)	23.1	44.6	51.9	800	20	2	0.7
BEA(104)	12.6	37.3	33.9	800	20	2	0.7
BEA(150)	22.6	43.3	52	800	20	2	0.7
BEA(440)	23.5	44.6	52.6	800	20	2	0.7
BEA(1700)	22.6	44.8	50.6	800	20	2	0.7
ZSM(1880)	24.4	45.1	54.2	800	20	2	0.7
ZSM(2120)	24.6	46.8	52.6	800	20	2	0.7
TS-1	23.4	43.9	53.3	800	20	2	0.7
SBA-15	25.6	46.2	55.4	800	20	2	0.7
MCM-41	25.0	47	53.2	800	20	2	0.7
SiC	24.3	43.5	55.9	800	20	2	0.7
SiO_2	24.6	43.2	56.9	800	15	2	0.7

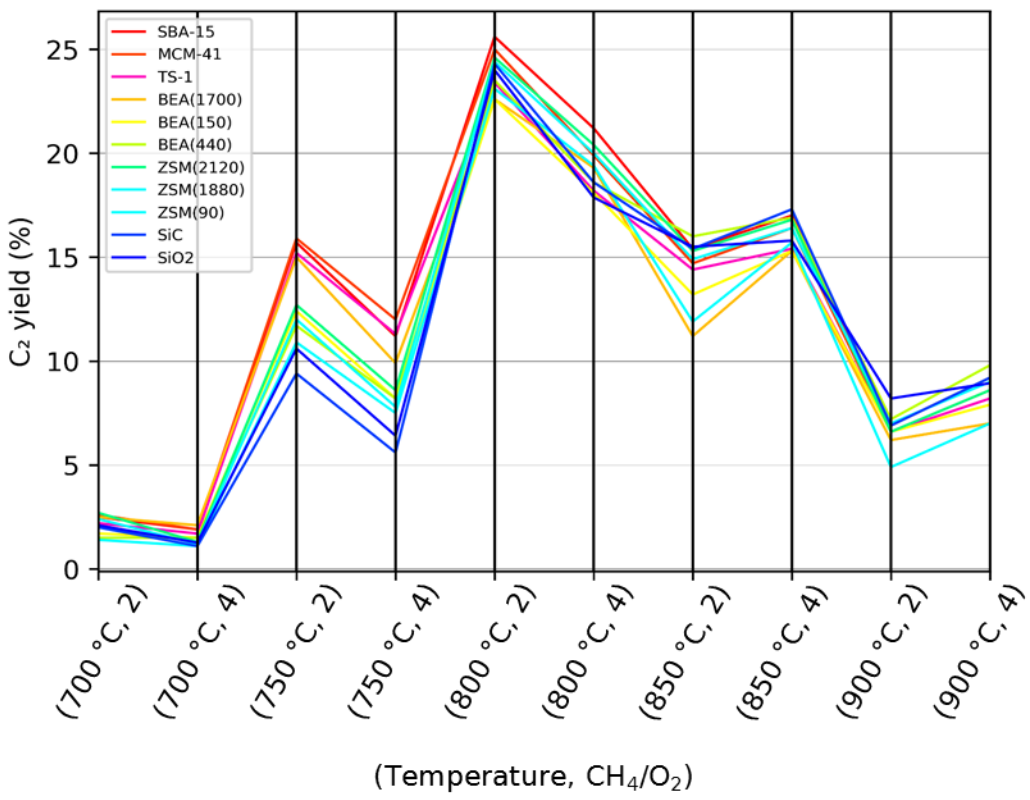

Figure 3.4. Variation of the C_2 yield in response to the temperature and the CH_4/O_2 ratio.

In general, SiO_2 is believed as the best support for Mn–Na_2WO_4. A potential explanation is that the cristbalite phase of SiO_2, formed at a calcination temperature in the presence of Na^+, strongly stabilizes tetrahedral WO_4^{2-} as active species [12,13,17]. On the other hand, in Chapter 2, I found that the choice of Si-based supports greatly affected the response of the catalysts to the variation of reaction conditions, especially when the conditions were deviated off the best conditions [16,18]. This differentiated the ability of catalysts in terms of low-temperature methane activation as well as C_2 selectivity tolerance to harsh conditions.

Accordingly, the performance of the catalysts with the best C_2 yield over 20% was compared at different temperatures and CH_4/O_2 ratios (Figure 3.4). At 800 °C and

the CH_4/O_2 ratio of 2, corresponding to the best conditions for all the good catalysts, the C_2 yield was not largely different among the catalysts (22-25.5%). However, the difference among the catalysts largely expanded when the reaction conditions were deviated from the optimum ones: 9–16% at (750 °C, CH_4/O_2=2), 6–13% at (750 °C, CH_4/O_2 =4), and 22–25.5% at (800 °C, CH_4/O_2 =2). Further deviation rather reduced the difference, as all the catalysts were basically not performant in these conditions. To comprehend the different behaviors of the catalysts at deviated conditions, the C_2 yield is broken down into the CH_4 conversion and the C_2 selectivity, as depicted in Figure 3.5.

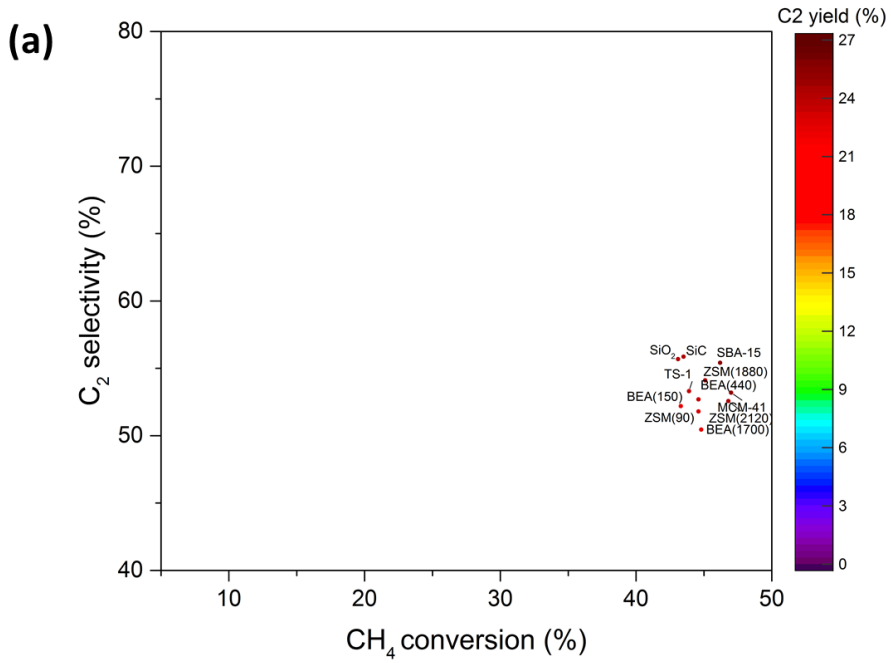

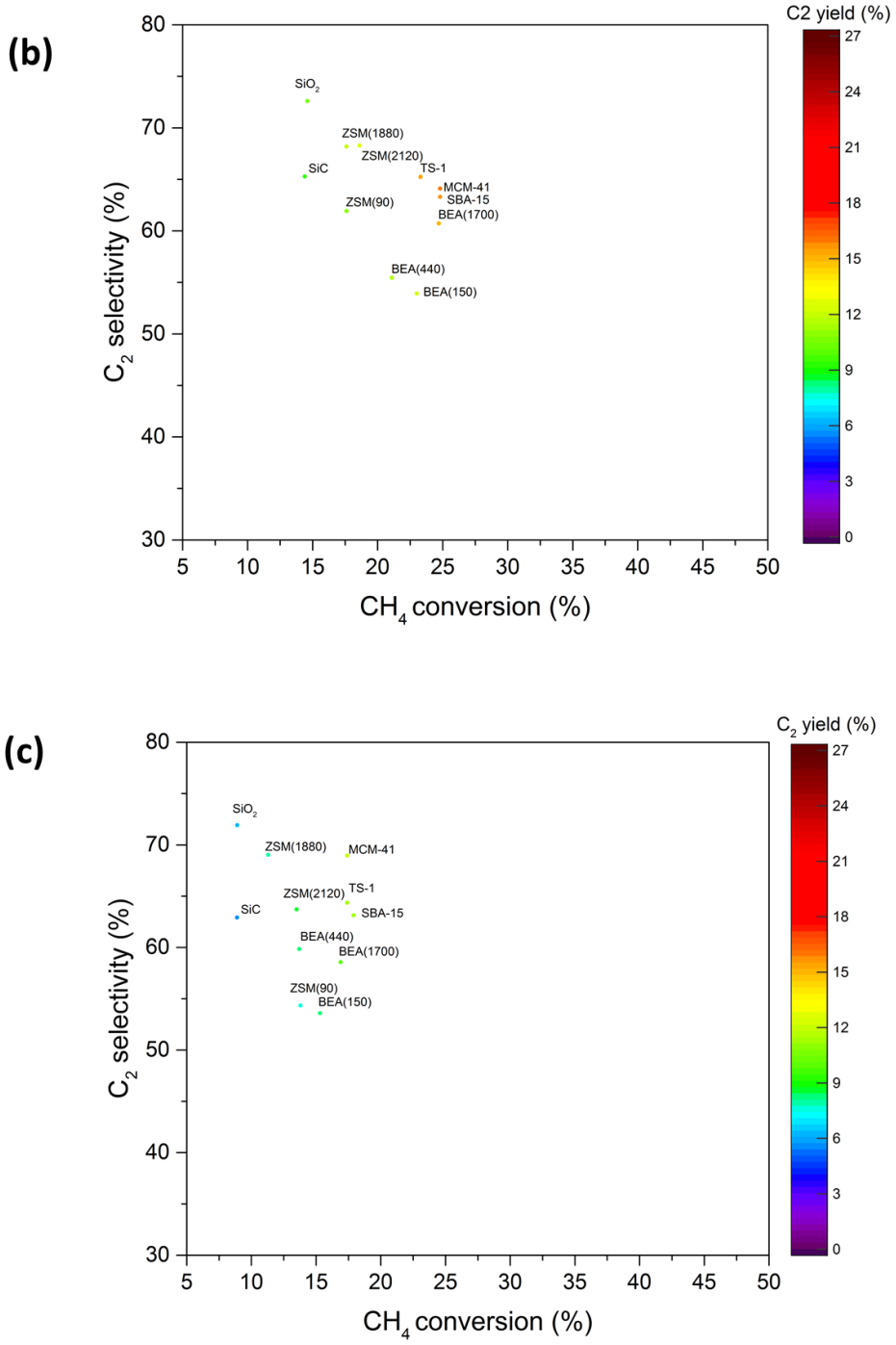

Figure 3.5. Process dependence of catalyst performance: (a) (Temp, CH_4/O_2) = (a) (800 °C, 2 mol/mol), (b) (750 °C, 2 mol/mol), (c) (750 °C, 4 mol/mol), and (d) (800 °C, 2 mol/mol). The total flow volume and the partial pressure of Ar are fixed at 20 mL/min and 0.70 atm, respectively.

As can be seen in Figure 3.5a, Mn–Na_2WO_4 showed consistent performance at 800 °C and CH_4/O_2 = 2 when immobilized on silica-rich supports (SBA-15, MCM-41, ZSM(2120), ZSM(1880), ZSM(90), BEA(440), BEA(150), SiO_2 and, SiC). The CH_4 conversion of 40–50% and the C_2 selectivity of 50–60% resulted in the C_2 yield of 22–25.6% C_2 yield. Such high performance of Mn–Na_2WO_4 at similar conditions was reported in many literature reports [4,10,16]. On the other hand, the deviation of process conditions from the optimum ones increased the deviation of the performance among these catalysts: a great difference when the temperature decreases to 750 °C with CH_4/O_2 ratio of 2. At this milder condition, the performance among the performant catalysts were decrease sharply because of the trade-off between conversion and selectivity; but their variation was comparable among Si-based supports. The mesoporous sillica (MCM-41, SBA-15) and BEA(1700) exhibited the highest CH_4 conversion. Non-ordered structured like SiC and SiO_2 showed the least activity. In general, BEA-type zeolite support showed higher CH_4 conversion compared to ZSM-typed zeolite, while ZSM keep much higher C_2 selectivity. Top 4 catalysts with the highest C_2 yields were obtained for Mn–Na_2WO_4 when cooperated in supports such as SBA-15 (15.93%), MCM-41 (15.72%), TS-1 (15.17%), and BEA(1700) (14.96%), which were able to keep reasonable high CH_4 conversion and C_2 selectivity. Such observation was further validated at milder condition by an increase at the CH_4/O_2 ratio of 4 at 750 °C in Figure 3.4c. At this condition, methane activation becomes more difficult, catalysts which exhibited better CH_4 conversion at CH_4/O_2 ratio of 2 are obviously advantageous toward C_2 yield at high CH_4/O_2 ratio. However, under harsh condition (850 °C and CH_4/O_2=2), SiO_2 give the highest C_2 yield. The highest C_2 yield might come from the kept high C_2 yield, while the CH_4 conversion appeared not much deviated among catalysts supports. Therefore, characterization should be conducted for

clarifying the origin of difference between catalysts activity among Mn–Na_2WO_4/Si-based catalysts.

3.3.2. Catalyst characterization

In order to clarify the origin of different performance of Mn–Na_2WO_4 supported on various Si-based supports, catalysts were characterized by several techniques. First, Raman spectroscopy was employed to investigate the structure of catalysts. The spectra of the catalysts are shown in Figure 3.6. Mn–Na_2WO_4/SiO_2 is regarded as the most standard catalyst. Its spectrum exhibits two bands at 960 and 926 cm^{-1} due to the tetrahedral WO_4^{2-}, and strong band at 409 cm^{-1} ascribed to α-cristobalite and the exist of Mn_2O_3 peak in some catalyts. The co-existence of tetrahedral WO_4^{2-}, Mn_2O_3, and SiO_2 in the α-cristobalite form is believed as the prerequisite for obtaining highly selective Mn–Na_2WO_4 catalysts [13,17,19,20]. The main active site of this catalyst is tetrahedral WO_4^{2-}, which undergoes a catalytic redox cycle between W^{6+} and $W^{5+/4+}$ based on the homolytic dissociation of CH_4 and subsequent oxidation [9,13,16]. Hence, it was considered that Si-based supports being able to form tetrahedral WO_4^{2-} Mn_2O_3, and α-cristobalite would afford the performance comparable to that of Mn–Na_2WO_4/SiO_2. This hypothesis was confirmed by cross-referencing between the catalytic performance in Table 3.2 and the Raman spectra in Figure 3.6: The catalysts which exhibited the best C_2 yield over 20% satisfied the prerequisite. On the other hand, any Si-based supports, which mediate the formation of undesired mixed oxides instead of preferred oxides, would result in poor performance [9,10,17]. Indeed, the poor catalysts possessed a band at around 890 cm^{-1} for octahedral tungstate [21], while the bands of the tetrahedral WO_4^{2-} and α-cristobalite almost completely vanished. In the

case of Al-rich zeolites, no peak of Al was observed in the spectra. The high-temperature calcination melts zeolites. The Al atoms are distributed in the resultant SiO_2, thus restricting the formation of α-cristobalite [9,10,17]. Besides, acidic Al sites binds ethylene for its combustion [17].

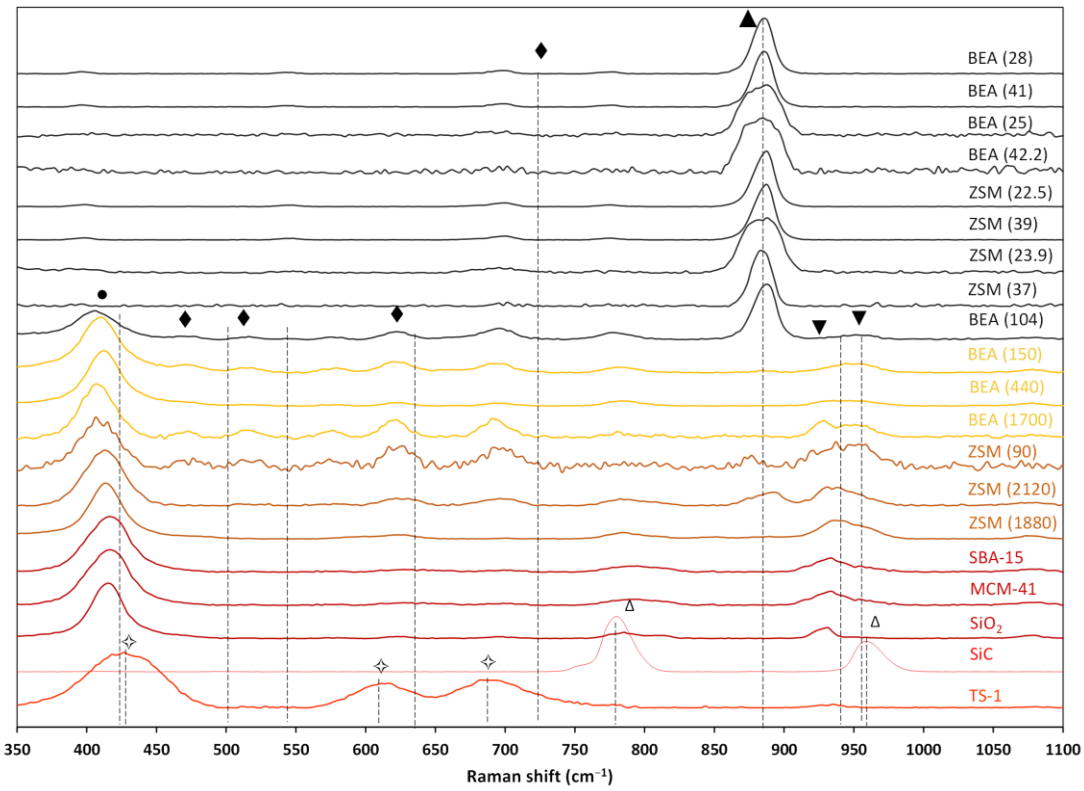

Figure 3.6. Raman spectra of Mn–Na_2WO_4 catalysts prepared using different Si-based supports. Na_2WO_4 (▼), α–cristobalite (●), $MnWO_4$ (▲), Mn_2O_3 (♦), and $MnTiO_3$ $MnTiO_3$ (✧), Si-C (Δ).

The XRD spectra further confirmed the phase difference among the catalysts (Figure 3.7). It is clear that the XRD patterns among good catalysts shared similar features arising from the co-existence of Na_2WO_4, Mn_2O_3 and α-cristobalite phase [14,22,23]. A minor presence of $MnWO_4$ was observed in some catalysts (SiC, TS-1, and SBA-15). In addition, besides of Na_2WO_4, Mn_2O_3 and α-cristobalite, there are

several peak of SiC at 33, 36, 38° [24,25]. The crystallite sizes of Na_2WO_4 and Mn_2O_3 calculated based on the Scherrer equation were found to be in agreement with literature results [26]. The poor catalysts showed poor crystallinity (as seen from noisy XRD patterns) and contained the undesired mixed oxides ($MnWO_4$, $NaWO_3$, and Mn_2O_3). Likewise, the Raman and XRD results afforded a consistent picture: The formation of tetrahedral WO_4^{2-}, as the main active phase, premises the formation of α-cristobalite, otherwise it forms non-selective mixed oxide phases. Mn–Na_2WO_4/TS-1 is exceptional catalyst: there is the peak of interaction between Ti and Mn, which peak of $MnTiO_3$ shown in XRD and Raman analysis. In the literature, it could be found that the addition of Ti accelerate the generation of oxygen spillover from Mn_2O_3 to the Na_2WO_4, thus increasing the performance of Mn–Na_2WO_4.

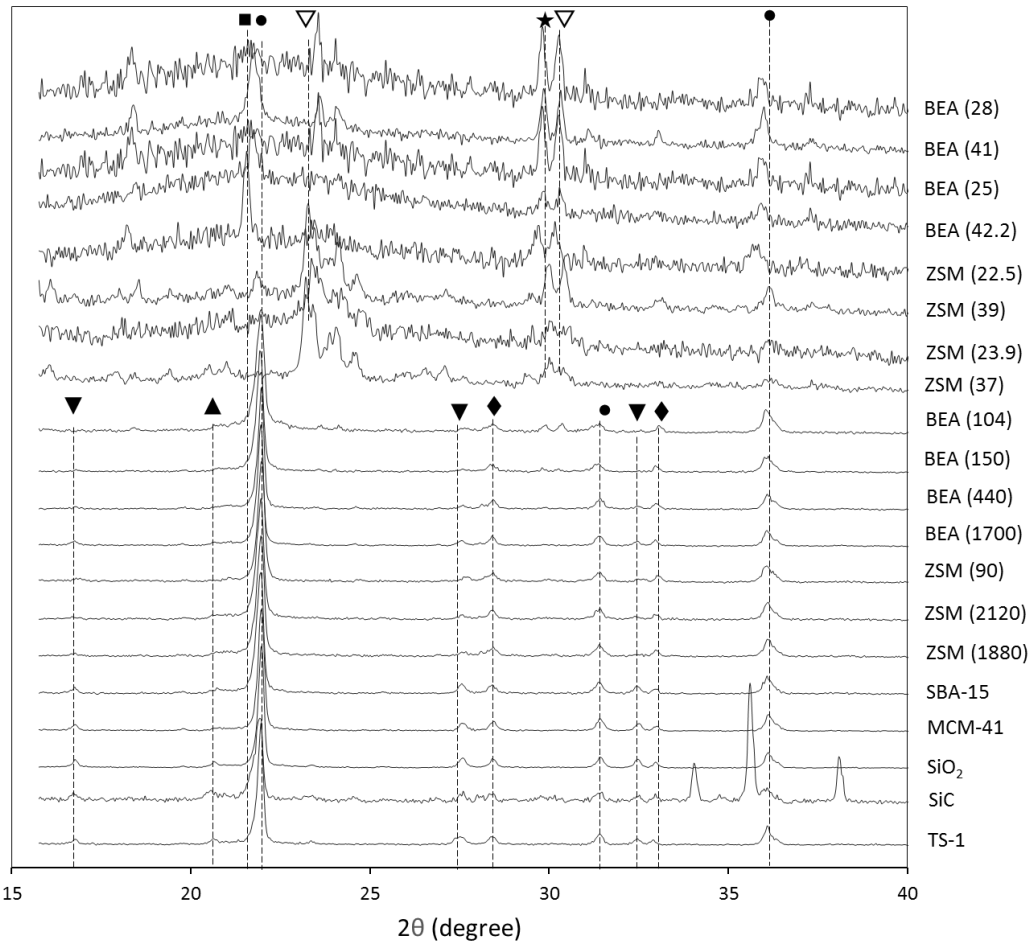

Figure 3.7. XRD patterns of Mn–Na_2WO_4 catalysts prepared using different Si-based supports. Na_2WO_4 (▼), Tridymite (■),α-cristobalite (●), $MnWO_4$ (▲), Mn_2O_3 (♦), $NaWO_3$ (∇).

The good and poor catalysts were clearly differentiated based on the phase structure of oxides. Next, I attempted to understand the difference among the good catalysts. It was suspected that the different performance of the catalysts at mild conditions could originate from different surface properties, such as the morphology, the dispersion of the active phase, and the surface composition. Accordingly, SEM–EDS measurements were performed for selected catalysts with the best C_2 yield over 20% (Figure 3.8).

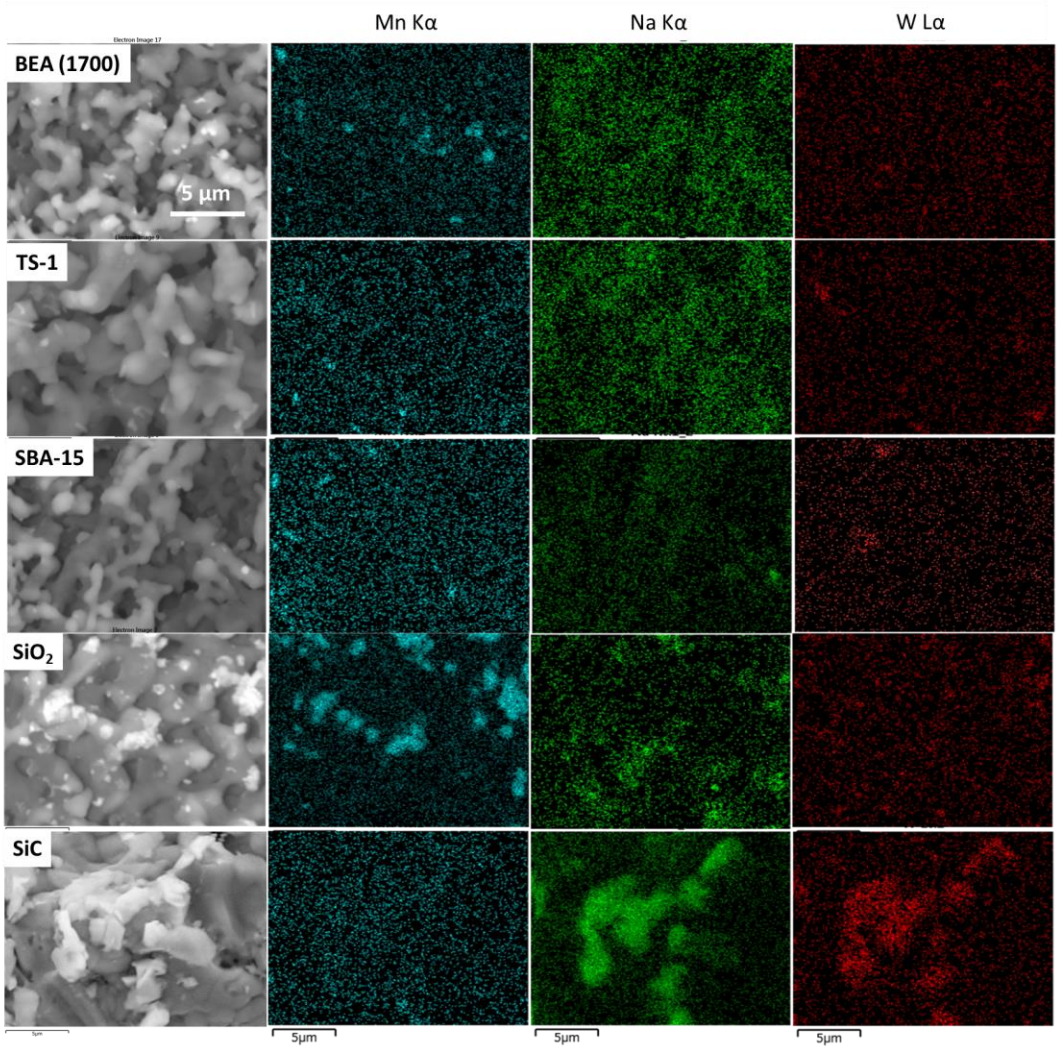

Figure 3.8. SEM and EDS results for selected Mn–Na_2WO_4 catalysts with the best C_2 yield over 20%. Scale bar indicated 5 µm.

The EDS mapping results in Figure 3.8 reveals that SiO_2- and SiC-supported catalysts possess an inhomogeneous distribution of the active metals. In particular, the SiO_2-supported catalyst exhibited a local enrichment of Mn, while the Na and W special distribution was inhomogeneous for the SiC-supported catalyst. Contrary, the EDS results for catalysts based on ordered-porous supports (BEA(1700), TS-1, SBA-15) showed a homogeneous dispersion of all the three active elements.. Their morphology also looked similar with each other. .

Cross-referencing the results for catalytic activity at 750 °C (Figures 3.5b,c) and the EDS results (Figure 3.8) suggests that the catalytic activity at a lower temperature is correlated with the uniform distribution of active elements throughout the surfaces of the supports. Supports with irregular pores exhibited a less uniform distribution of the active elements and thus poorer performance compared to supports with ordered pores (SBA-15 or high-silica zeolites). Metal precursors dispersed better in the ordered pores of zeolites or mesoporous silica during the impregnation. This leads to a uniform distribution of active elements after the calcination. Better dispersion of active elements results in more accessible sites which is believe to be important to enable low-temperature activation of CH_4.

Table 3.3. Near-surface composition for selected Mn–Na_2WO_4 catalysts with the best C_2 yield over 20%.[a]

Support	O(1s)(MO_x)		O(1s)(SiO_2)		Si(2p)		W(4f7/2)		Na(1s)		Mn(2p)	
	BE	%a	BE	%a	BE	%a	BE	%a	BE	%a	BE	%a
BEA (150)	529.9	2.9	532.3	59.5	103	32.3	35.3	0.9	1072	4.1	641.5	0.2
BEA (440)	530.2	4.2	532.4	55.7	103.2	34.5	35.4	1.1	1072	4.2	641.7	0.4
BEA (1700)	530	5.0	532.4	55.1	103.2	35	35.4	1.1	1072	3.4	641.6	0.3
ZSM (90)	529.8	2.9	532.1	59.2	102.7	29.9	35	0.9	1072	6.7	641.5	0.4
ZSM (2120)	530.2	4.4	532.5	56.3	103.2	34.7	35.3	0.9	1072	3.1	641.8	0.4
ZSM (1880)	530.2	4.9	532.6	56.3	103.4	34	35.5	1.0	1071	3.4	642	0.4
SBA-15	530.1	5.0	532.4	53.5	103.3	36.6	35.5	1.3	1071	3.3	641.9	0.3
TS-1	530.1	6.9	532.3	53.5	103.2	33.5	35.4	1.0	1072	4.7	641.7	0.4
SiO_2	530	3.9	532.6	58.5	103.2	33.4	35.1	0.7	1072	2.8	641.9	0.6

[a] Loading: 2% Mn, 5% Na_2WO_4.

Among the ordered porous supports, mesoporous silica (SBA-15) gave a higher activity compared to that of BEA and ZSM at a lower temperature. As their morphology and dispersion of active elements looked quite identical, the surface composition of the catalysts was examined based on XPS. Table 3.3 compares the near-surface concentration of the metals (Na, Mn, and W) for selected catalysts with the best C_2

yield over 20%. It is clear that the surface was enriched in Na for all the catalysts, and its near-surface concentration was much higher than those of W and Mn when compared to the theoretical composition. Apparently, during the high-temperature calcination, light elements like Na is easily migrated from the inner parts of the catalysts to the near-surface area, resulting in the observed near-surface enrichment in Na. On the other hand, the SBA-15-supported catalyst had the highest near-surface concentration of W (1.3%a), followed by BEA (1.1%a) and ZSM (0.9–1.0%a), which is highly consistent with the order of CH_4 conversion of these catalysts at 750 °C. This fact together with SEM-EDS results suggests that the number of tetrahedral WO_4^{2-} active sites available is the most important for the low-temperature CH_4 activation. The higher concentration of W on the near surface of the SBA-15-supported catalyst compared to the ZSM- and BEA-supported catalysts could be attributed to the pore size of the support itself. The large pore size of SBA-15 plausibly leads to more uniform impregnation of the metal precursor. The higher CH_4 conversion of BEA than ZSM zeolite further confirmed the advantage of the larger pore size on the dispersion of W.

3.4. Conclusion

In this chapter, the OCM performance of Mn–Na_2WO_4 catalysts supported on various Si-based supports were thoroughly investigated in order to discover the origin of their different performance. It was found that the pure or high silica supports were suitable to immobilize Mn–Na_2WO_4 When such supports were employed, the catalysts exhibited similar performance at 800 °C. However, at a lower temperature, mesoporous silica, SBA-15, appeared to be most promising in terms of their ability to maintain the catalytic performance. Through a series of characterization, it was elucidated that the large and ordered pores of SBA-15 is essential for improving the dispersion of tetrahedral WO_2^- active sites macroscopically over particles and microscopically newer the surface. The OCM reaction suffers from an intrinsic tradeoff between the CH_4 conversion and C_2 selectivity, which becomes severer at a higher temperature. The structure-performance relationship clarified here is directly useful for developing catalysts operatable at a lower temperature.

References

[1] B. Wang, S. Albarracín–Suazo, Y. Pagán–Torres, E. Nikolla, Advances in methane conversion processes, Catal. Today, 285 (2017) 147–158.

[2] B.L. Farrell, V.O. Igenegbai, S. Linic, A Viewpoint on Direct Methane Conversion to Ethane and Ethylene Using Oxidative Coupling on Solid Catalysts, ACS Catal., 6 (2016) 4340–4346.

[3] E.V. Kondratenko, T. Peppel, D. Seeburg, V.A. Kondratenko, N. Kalevaru, A. Martin, S. Wohlrab, Methane conversion into different hydrocarbons or oxygenates: current status and future perspectives in catalyst development and reactor operation, Catal. Sci. Technol., 7 (2017) 366–381.

[4] U. Zavyalova, M. Holena, R. Schlögl, M. Baerns, Statistical analysis of past catalytic data on oxidative methane coupling for new insights into the composition of high–performance catalysts, ChemCatChem, 3 (2011) 1935–1947.

[5] P. Wang, G. Zhao, Y. Wang, Y. Lu, $MnTiO_3$–driven low–temperature oxidative coupling of methane over TiO_2–doped Mn_2O_3–Na_2WO_4/SiO_2 catalyst, Sci. Adv., 3 (2017) e1603180.

[6] J. Sun, J.W. Thybaut, G.B. Marin, Microkinetics of methane oxidative coupling, Catal. Today, 137 (2008) 90–102.

[7] P. Schwach, X. Pan, X. Bao, Direct conversion of methane to value–added chemicals over heterogeneous catalysts: challenges and prospects, Chem. Rev., 117 (2017) 8497–8520.

[8] L. Olivier, S. Haag, H. Pennemann, C. Hofmann, C. Mirodatos, A.C. van Veen, High–temperature parallel screening of catalysts for the oxidative coupling of methane, Catal. Today, 137 (2008) 80–89.

[9] S. Arndt, T. Otremba, U. Simon, M. Yildiz, H. Schubert, R. Schomäcker, Mn–Na_2WO_4/SiO_2 as catalyst for the oxidative coupling of methane. What is really known?, Appl. Catal., A, 425–426 (2012) 53–61.

[10] M. Yildiz, Y. Aksu, U. Simon, T. Otremba, K. Kailasam, C. Göbel, F. Girgsdies, O. Görke, F. Rosowski, A. Thomas, R. Schomäcker, S. Arndt, Silica material variation for the Mn_xO_y–Na_2WO_4/SiO_2, Appl. Catal., A, 525 (2016) 168–179.

[11] M. Yildiz, U. Simon, T. Otremba, Y. Aksu, K. Kailasam, A. Thomas, R. Schomäcker, S. Arndt, Support material variation for the Mn_xO_y–Na_2WO_4/SiO_2 catalyst, Catal. Today, 228 (2014) 5–14.

[12] A. Malekzadeh, A.K. Dalai, A. Khodadadi, Y. Mortazavi, Structural features of Na_2WO_4–MO_x/SiO_2 catalysts in oxidative coupling of methane reaction, Catal. Commun., 9 (2008) 960–965.

[13] S. Ji, T. Xiao, S. Li, L. Chou, B. Zhang, C. Xu, R. Hou, A.P.E. York, M.L.H. Green, Surface WO_4 tetrahedron: the essence of the oxidative coupling of methane over M–W–Mn/SiO_2 catalysts, J. Catal., 220 (2003) 47–56.

[14] T.W. Elkins, H.E. Hagelin–Weaver, Characterization of Mn–Na_2WO_4/SiO_2 and Mn–Na_2WO_4/MgO catalysts for the oxidative coupling of methane, Appl. Catal., A, 497 (2015) 96–106.

[15] M. Yildiz, Y. Aksu, U. Simon, K. Kailasam, O. Goerke, F. Rosowski, R. Schomäcker, A. Thomas, S. Arndt, Enhanced catalytic performance of Mn_xO_y–Na_2WO_4/SiO_2 for the oxidative coupling of methane using an ordered mesoporous silica support, Chem. Commun., 50 (2014) 14440–14442.

[16] T.N. Nguyen, T.P.N. Tran, K. Takimoto, A. Thakur, S. Nishimura, J. Ohyama, I. Miyazato, L. Takahashi, J. Fujima, K. Takahashi, T. Taniike, High–Throughput Experimentation and Catalyst Informatics for Oxidative Coupling of Methane, ACS Catal., 10 (2020) 921–932.

[17] S. Hou, Y. Cao, W. Xiong, H. Liu, Y. Kou, Site requirements for the oxidative coupling of methane on SiO_2–supported Mn catalysts, Ind. Eng. Chem. Res., 45 (2006) 7077–7083.

[18] C. Karakaya, H. Zhu, C. Loebick, J.G. Weissman, R.J. Kee, A detailed reaction mechanism for oxidative coupling of methane over $Mn/Na_2WO_4/SiO_2$ catalyst for non–isothermal conditions, Catal. Today, 312 (2018) 10–22.

[19] A. Palermo, J.P.H. Vazquez, A.F. Lee, M.S. Tikhov, R.M. Lambert, Critical influence of the amorphous silica–to–cristobalite phase transition on the performance of $Mn/Na_2WO_4/SiO_2$ catalysts for the oxidative coupling of methane, J. Catal., 177 (1998) 259–266.

[20] A. Palermo, J.P.H. Vazquez, R.M. Lambert, New efficient catalysts for the oxidative coupling of methane, Catal. Lett., 68 (2000) 191–196.

[21] R.T. Yunarti, S. Gu, J.–W. Choi, J. Jae, D.J. Suh, J.–M. Ha, Oxidative coupling of methane using Mg/Ti–doped SiO_2–supported Na_2WO_4/Mn catalysts, ACS Sustain. Chem. Eng, 5 (2017) 3667–3674.

[22] J. Wang, L. Chou, B. Zhang, H. Song, J. Zhao, J. Yang, S. Li, Comparative study on oxidation of methane to ethane and ethylene over Na_2WO_4–Mn/SiO_2 catalysts prepared by different methods, J. Mol. Catal. A: Chem., 245 (2006) 272–277.
[23] A. Palermo, J.P. Holgado Vazquez, A.F. Lee, M.S. Tikhov, R.M. Lambert, Critical influence of the amorphous silica–to–cristobalite phase transition on the performance of $Mn/Na_2WO_4/SiO_2$ catalysts for the oxidative coupling of methane, J. Catal., 177 (1998) 259–266.
[24] H. Liu, D. Yang, R. Gao, L. Chen, S. Zhang, X. Wang, A novel Na_2WO_4–Mn/SiC monolithic foam catalyst with improved thermal properties for the oxidative coupling of methane, Catal. Commun., 9 (2008) 1302–1306.
[25] J. Kim, L.–H. Park, J.–M. Ha, E.D. Park, Oxidative Coupling of Methane over Mn2O3–Na_2WO_4/SiC Catalysts, Catalysts, 9 (2019) 363.
[26] N.S. Hayek, N.S. Lucas, C. Warwar Damouny, O.M. Gazit, Critical Surface Parameters for the Oxidative Coupling of Methane over the Mn–Na–W/SiO_2 Catalyst, ACS Appl. Mater. Interfaces, 9 (2017) 40404–40411.

Chapter 4

Learning catalyst design based on bias-free dataset for oxidative coupling of methane

Abstract: The discovery of synergistic multicomponent catalysts has been hardly achieved without preknowledge-driven try-and-error cycles. Here, I generated 300 M1–M2–M3/Support catalysts based on random sampling of a huge materials space, and evaluated their performance in the oxidative coupling of methane using a high-throughput screening instrument. Thus acquired catalyst big data was used to derive a guideline of combinatorial catalyst design. It was proven that the catalyst performance was determined by the performance of constituent combinations, not by the inclusion of specific elements. Novel synergistic combinations were identified, and the catalyst design was successfully generalized based on the decision tree regression analysis.

Keywords: Oxidative coupling of methane, High-throughput experimentation, Catalyst informatics, Decision tree, Catalyst design.

4.1. Introduction

The history evidences serendipity as one of the major drivers in the field of catalysis [1-4]. In particular, the design of solid catalysts often premises synergistic combinations of multiple components. A combination can be synergistic by many causes, e.g. when two components have complementary or cooperative roles in multi-step catalysis [5-10], when an auxiliary component promotes/sustains the function of the main component [11-13], when multiple entities create one specific structure on surfaces [14-18], and so on [19-22]. The plurality of causes in turn makes estimation difficult: Expected synergy in one aspect does not necessarily give practical synergy when the combination is negative in other unaccounted aspects [23]. Exploitation of synergistic combinations is essential for the design of performant solid catalysts, but they are hardly predictable. This is why serendipity in try and error still occupies an irreplaceable role. Along with the rise of materials informatics, data science approaches are extensively applied in the field of catalysis [24]. Since performance prediction of solid catalysts requests a model to learn combinatorial effects, catalyst informatics would bring breakthrough on the empirical nature of catalyst development.

Upgrading methane without mediating syngas attracts great attention due to the increasing availability of natural gas [25]. Oxidative coupling of methane (OCM) indicates the conversion of methane into C_2 products, especially in the presence of molecular oxygen. The OCM is featured with a persistent conversion-selectivity tradeoff caused by the inertness of methane with respect to the desired C_2 products [26]. Nonetheless, a wide variety of catalysts are known to improve the C_2 yield as compared to the non-catalytic free radical process. Zavyalova et al. reported a pioneering work on the application of catalyst informatics in OCM [27]. They applied the analysis of variance to 1870 data that were collected from literature. Thus identified synergistic combinations (such as Na–La, Na–Mn, and Ba–Sr) were in line with the understanding of experimentalists. More recently, an elegant meta-analysis approach

was presented by Schmack et al. [28]. Physicochemically interpretable hypotheses were translated into machine-learnable descriptors with the aid of textbook knowledge. They were evaluated on the literature dataset, and eventually gave a physicochemically interpretable model that relates the catalyst composition with the C_2 yield. The model successfully proposed the importance of combining carbonate- and oxide-forming elements. On the other hand, as was stated by the same authors, the model would be negatively affected by inconsistency of catalyst evaluation processes among literature. Anthropogenic biases present in the literature dataset would be also an important risk as a model learns such biases [29].

In Chapter 2, a high-throughput screening (HTS) instrument was successfully developed for automatic performance evaluation of 20 catalysts at a predefined set of reaction conditions in a fixed-bed configuration [30]. Here, the same HTS instrument was used to acquire a bias-free and process-consistent OCM dataset. 300 M1–M2–M3/Support catalysts were prepared, where the four components were randomly selected from a library. Their performance in OCM was evaluated at 135 conditions. The obtained dataset was analyzed with the aim to uncover hidden guidelines behind combinatorial catalyst design.

4.2. Materials and methods

4.2.1. Materials

Metal precursors used in this work were $LiNO_3$, $NaNO_3$, $Mg(NO_3)_2$, KNO_3, $Ca(NO_3)_2{\cdot}4H_2O$, $Ti(O\mathit{i}Pr)_4$, $VOSO_4{\cdot}\mathit{x}H_2O$ (x = 3–5), $Mn(NO_3)_2{\cdot}6H_2O$, $Fe(NO_3)_3{\cdot}9H_2O$, $Co(NO_3)_2{\cdot}6H_2O$, $Ni(NO_3)_2{\cdot}6H_2O$, $Cu(NO_3)_2{\cdot}3H_2O$, $Zn(NO_3)_2{\cdot}6H_2O$, $Sr(NO_3)_2$, $Y(NO_3)_3{\cdot}6H_2O$, $ZrO(NO_3)_2{\cdot}\mathit{x}H_2O$ (x = 2), $(NH_4)_6Mo_7O_{24}{\cdot}4H_2O$, $Pd(OAc)_2$, $CsNO_3$, $Ba(NO_3)_2$, $La(NO_3)_3{\cdot}6H_2O$, $Ce(NO_3)_3{\cdot}6H_2O$, $Nd(NO_3)_3{\cdot}6H_2O$, $Eu(NO_3)_3{\cdot}5H_2O$, $Tb(NO_3)_3{\cdot}5H_2O$, $Hf(OEt)_4$, and $(NH_4)_{10}H_2(W_2O_7)_6$. They were purchased from either of Sigma–Aldrich, Kanto Chemical, Wako Pure Chemical Industries, and Alfa-Aesar. The following solid powders were used as supports or as support precursors: Magnesium oxide (MgO, 5.5 m^2/g, Kanto Chemical), aluminum oxide (γ-Al_2O_3, 150 m^2/g, Sumitomo Chemical Industry), silica gel (SiO_2, 650 m^2/g, 60N, Kanto Chemical), calcium hydroxide ($Ca(OH)_2$, 3.0 m^2/g, Wako Pure Chemical Industries), titanium(IV) oxide (TiO_2, 17.4 m^2/g, anatase, Kanto Chemical), zirconium(IV) oxide (ZrO_2, 3.2 m^2/g, Kanto Chemical), barium hydroxide ($Ba(OH)_2{\cdot}8H_2O$, 1.1 m^2/g, Wako Pure Chemical Industries), lanthanum(III) oxide (La_2O_3, 8.3 m^2/g, Wako Pure Chemical Industries), and cerium(IV) oxide (CeO_2, 3.9 m^2/g, Wako Pure Chemical Industries). The specific surface area of the supports was determined by the Brunauer–Emmett–Teller (BET) method for the nitrogen adsorption isotherm at 77 K.

4.2.2. Catalyst library

The catalyst library was created by preparing 300 catalysts. Table 4.1 summarizes the composition, the best performance, and the corresponding conditions for the 300 catalysts. The catalysts were expressed in the form of M1–M2–M3/Support. The three active elements (M1–M3) were randomly selected from either of Li, Na, Mg, K, Ca, Ti, V, Mn, Fe, Co, Ni, Cu, Zn, Sr, Y, Zr, Mo, Pd, Cs, Ba, La, Ce, Nd, Eu, Tb, Hf, W, and “none”, where repetitive selection of the same element was allowed. They were combined with a support which was randomly

picked up from either of MgO, Al_2O_3, SiO_2, CaO, TiO_2, ZrO_2, BaO, La_2O_3, and CeO_2. Note that CaO and BaO were obtained from the corresponding hydroxides by calcination. Three-combinations with repetitions from 28 elements (including none) and 9 supports correspond to a total of 36,540 catalysts. Three hundreds among 36,540 might not be sufficient to find all the important trends present in the entire parametric space. However, the 300 catalysts correspond to sampling of respective elements and supports at least 20 times (Figure 4.1). Moreover, a majority of the catalysts have never been reported in literature.

The catalysts were prepared according to the method described in Chapter 2 [30]. The loading of individual elements was fixed at 0.37 mmol to a unit gram of a support. Remarkably, the loading was duplicated when the same element was doubly selected; no metal precursor was added when "none" was selected; and so on. A support powder was impregnated with a solution of selected metal precursors at 50 ℃ for 6 h. The resultant solid was vacuum dried, and subjected to calcination at 1000 ℃ under air for 3 h. Twenty catalysts were produced in one experiment with the aids of a parallel hot stirrer (Reacti-Therm, Thermo Scientific) and a centrifugal evaporator (CVE-3100, Eyela).

Table 4.1. Catalyst library. The composition, the best performance, and the corresponding conditions are shown.[a,b,c]

No	M1	M2	M3	Support	C_2 yield (%)	CH_4 conversion (%)	C_2 selectivity (%)	CH_4/O_2 (mol/mol)	Temp. (°C)	Total flow (mL/min)	P_{Ar} (atm)
1	Li	K	Mn	MgO	8.2	29.0	28.3	2	800	10	0.15
2	Li	Fe	Tb	MgO	4.7	24.7	19.1	2	850	10	0.4
3	Li	Fe	Hf	MgO	2.5	28.1	8.8	2	900	10	0.15
4	Na	Na	none	MgO	7.4	34.0	21.7	2	850	20	0.15
5	Na	Ni	Y	MgO	1.0	24.6	4.1	6	750	20	0.7
6	Na	Ce	Tb	MgO	3.8	32.1	11.9	6	900	20	0.15
7	Na	Tb	Hf	MgO	8.6	30.9	27.7	2	800	20	0.15
8	Na	Eu	Hf	MgO	16.6	35.6	46.7	2	750	10	0.15
9	Mg	Ca	Zn	MgO	2.1	24.0	8.9	4	850	15	0.15
10	Mg	Mn	none	MgO	7.9	27.1	29.0	2	850	20	0.15
11	Mg	Zn	Eu	MgO	15.5	40.9	37.9	2	700	20	0.15
12	Mg	Nd	none	MgO	9.5	35.5	26.8	2	850	20	0.7
13	Ca	Zr	La	MgO	16.1	33.8	47.6	2	750	20	0.15
14	Ti	Ni	Cs	MgO	1.6	33.2	4.8	2	800	20	0.4

15	Ti	V	Ba	MgO	8.2	37.7	21.8	2	900	15	0.7
16	V	Fe	Ni	MgO	7.6	34.3	22.0	2	800	15	0.15
17	V	Mo	Pd	MgO	0.7	26.5	2.6	6	900	15	0.7
18	V	Tb	W	MgO	6.7	33.6	19.9	2	850	15	0.15
19	Fe	Y	Nd	MgO	3.6	21.5	16.9	2	800	20	0.15
20	Fe	Zr	none	MgO	7.1	37.8	18.7	2	850	20	0.15
21	Fe	Ce	Tb	MgO	6.2	25.0	25.0	2	800	10	0.15
22	Fe	La	Hf	MgO	6.5	29.3	22.2	2	850	15	0.15
23	Co	Zn	Sr	MgO	1.0	31.0	3.2	6	850	20	0.15
24	Co	Zn	Tb	MgO	5.7	36.6	15.6	2	900	20	0.15
25	Co	Y	Hf	MgO	7.0	26.6	26.4	2	700	20	0.15
26	Ni	Y	Tb	MgO	5.6	18.3	30.7	4	900	20	0.7
27	Y	La	Ce	MgO	12.1	37.8	32.1	2	700	20	0.15
28	Mo	Cs	La	MgO	8.5	31.8	26.8	2	850	20	0.4
29	Mo	Ce	Tb	MgO	7.3	33.2	22.0	2	800	20	0.15
30	Li	Mg	Hf	Al_2O_3	3.2	40.4	7.9	2	850	15	0.15
31	Li	Ca	Mn	Al_2O_3	7.2	38.4	18.8	2	850	20	0.15
32	Li	Ti	La	Al_2O_3	15.5	37.4	41.4	2	850	15	0.7
33	Li	Fe	none	Al_2O_3	9.2	32.2	28.4	2	850	10	0.7
34	Li	Hf	none	Al_2O_3	4.9	35.2	14.0	2	900	20	0.4
35	Na	K	Hf	Al_2O_3	8.2	32.0	25.7	2	850	10	0.4
36	Na	Ti	Cu	Al_2O_3	11.5	20.7	55.9	4	850	20	0.4
37	Na	Mn	Ni	Al_2O_3	1.2	26.6	4.5	6	850	20	0.7
38	Na	Co	Ni	Al_2O_3	7.8	28.5	27.2	2	800	10	0.15
39	Na	Co	none	Al_2O_3	9.3	35.7	26.2	2	850	10	0.7
40	Na	Cu	Ce	Al_2O_3	3.2	27.4	11.5	2	900	10	0.15
41	Mg	Mn	Cs	Al_2O_3	8.6	32.8	26.2	2	900	20	0.7
42	Mg	Co	Ba	Al_2O_3	2.7	26.9	10.0	2	900	10	0.15
43	Mg	La	Nd	Al_2O_3	8.2	37.7	21.6	2	850	20	0.15
44	K	Mn	Ni	Al_2O_3	1.5	26.4	5.8	6	900	15	0.7
45	K	Co	Cs	Al_2O_3	9.3	34.2	27.4	2	850	15	0.7
46	K	Y	Hf	Al_2O_3	10.8	20.5	52.4	4	850	15	0.7
47	K	La	W	Al_2O_3	4.7	24.0	19.7	2	800	20	0.4
48	Ti	Mn	Y	Al_2O_3	10.4	32.4	32.2	2	850	20	0.15
49	Ti	Fe	Mo	Al_2O_3	9.4	36.8	25.5	2	850	20	0.4
50	Ti	Cs	La	Al_2O_3	7.6	30.7	24.9	2	800	20	0.4
51	V	Cu	Ba	Al_2O_3	1.8	37.7	4.7	2	900	20	0.15
52	Fe	Pd	Nd	Al_2O_3	11.6	20.3	57.3	4	850	20	0.15
53	Fe	Ba	none	Al_2O_3	4.9	33.0	14.7	2	850	20	0.15
54	Fe	La	W	Al_2O_3	2.7	36.3	7.5	2	850	20	0.15
55	Co	Ni	Zr	Al_2O_3	1.3	32.3	4.1	2	900	20	0.15
56	Co	Zn	Nd	Al_2O_3	10.2	36.1	28.3	2	850	20	0.4
57	Co	Y	Tb	Al_2O_3	5.9	35.8	16.5	2	800	20	0.15
58	Ni	Cu	Zr	Al_2O_3	1.6	37.8	4.2	4	750	20	0.7
59	Ni	Zn	La	Al_2O_3	1.0	25.5	3.8	6	750	10	0.7
60	Cu	Y	Ce	Al_2O_3	1.7	20.0	8.4	6	900	20	0.15
61	Zn	Pd	Cs	Al_2O_3	2.0	26.9	7.6	6	850	15	0.7
62	Sr	Pd	none	Al_2O_3	9.1	21.0	43.1	4	850	10	0.15
63	Y	Pd	Ba	Al_2O_3	9.4	33.6	27.9	2	850	20	0.4
64	Zr	Cs	La	Al_2O_3	9.3	31.2	29.7	2	850	15	0.7
65	Ba	La	W	Al_2O_3	3.5	22.5	15.6	2	800	20	0.4
66	Li	K	Co	SiO_2	10.4	30.3	34.4	2	850	10	0.7
67	Li	Fe	W	SiO_2	6.5	36.9	17.7	2	900	20	0.4
68	Li	Ni	none	SiO_2	8.1	34.9	23.3	2	850	20	0.4
69	Li	Nd	Tb	SiO_2	8.4	26.4	31.8	2	850	20	0.4
70	Li	Ni	Hf	SiO_2	11.2	33.1	33.7	2	850	20	0.4
71	Na	Sr	Mo	SiO_2	12.9	36.6	35.2	2	850	10	0.7
72	Na	Ce	Tb	SiO_2	8.9	26.8	33.3	2	850	20	0.4
73	Mg	V	Pd	SiO_2	n.d.	n.d.	n.d.	n.d.	n.d.	n.d.	n.d.
74	Mg	Cu	Sr	SiO_2	7.3	27.1	27.0	2	800	10	0.15

75	Mg	Zn	Eu	SiO_2	7.6	43.2	17.6	2	850	20	0.15
76	K	Mn	La	SiO_2	8.1	36.5	22.2	2	850	20	0.4
77	K	Zr	Tb	SiO_2	7.7	15.3	50.4	4	900	20	0.15
78	Ca	Ti	Cu	SiO_2	9.7	34.4	28.2	2	900	20	0.7
79	Ti	Sr	La	SiO_2	8.4	29.3	28.7	2	850	20	0.15
80	Ti	Mo	Nd	SiO_2	4.5	30.8	14.8	6	900	20	0.15
81	V	Pd	Nd	SiO_2	n.d.	n.d.	n.d.	n.d.	n.d.	n.d.	n.d.
82	V	Cs	Nd	SiO_2	8.0	31.1	25.8	2	850	20	0.15
83	Mn	Fe	Cu	SiO_2	7.4	34.6	21.3	2	850	20	0.15
84	Mn	Zn	Sr	SiO_2	10.4	31.8	32.7	2	900	20	0.7
85	Co	Ni	Cu	SiO_2	6.1	33.9	18.1	2	850	20	0.4
86	Co	Y	Nd	SiO_2	8.7	23.5	37.1	2	800	20	0.15
87	Ni	W	none	SiO_2	0.7	2.2	30.2	2	700	15	0.7
88	Ni	Ce	Nd	SiO_2	8.3	26.9	30.9	2	850	10	0.7
89	Cu	La	Tb	SiO_2	3.9	37.0	10.5	2	900	20	0.4
90	Cu	none	none	SiO_2	8.1	34.3	23.6	2	800	10	0.15
91	Zn	Sr	Pd	SiO_2	1.2	43.5	2.8	2	850	20	0.7
92	Zr	Cs	Cs	SiO_2	2.5	18.0	13.8	6	900	15	0.15
93	Mo	Ba	none	SiO_2	8.5	32.8	25.9	2	850	20	0.4
94	Cs	Ba	Ce	SiO_2	7.8	23.2	33.6	2	850	15	0.7
95	Li	V	Eu	CaO	13.6	36.6	37.2	2	850	20	0.7
96	Li	Co	Mo	CaO	4.8	25.4	18.9	2	750	10	0.15
97	Li	Cu	Cs	CaO	5.6	31.0	18.1	2	900	20	0.15
98	Na	Mg	Hf	CaO	14.3	33.6	42.5	2	750	15	0.4
99	Na	Ti	Ce	CaO	11.9	31.6	37.6	2	700	20	0.15
100	Na	Mn	La	CaO	6.7	33.3	20.2	2	800	20	0.15
101	Na	Cu	Hf	CaO	4.2	25.6	16.3	2	800	20	0.15
102	Mg	Co	Ce	CaO	8.0	33.5	23.9	2	800	20	0.15
103	Mg	Cu	Eu	CaO	4.6	37.7	12.2	2	900	20	0.15
104	Mg	Sr	Y	CaO	14.4	35.6	40.5	2	800	20	0.4
105	Mg	Sr	Ba	CaO	17.4	39.6	44.1	2	800	20	0.7
106	Mg	Zr	Hf	CaO	15.9	36.6	43.6	2	750	20	0.15
107	K	Sr	Y	CaO	9.9	33.2	29.8	2	700	15	0.4
108	K	Y	Eu	CaO	13.1	40.4	32.3	2	750	20	0.15
109	Ca	Mn	none	CaO	7.6	28.4	26.6	2	850	15	0.15
110	Ca	Nd	Tb	CaO	7.2	38.4	18.8	2	850	20	0.15
111	Ti	Fe	Sr	CaO	10.3	31.2	32.9	2	700	20	0.15
112	Ti	Zn	Tb	CaO	12.5	36.1	34.6	2	700	20	0.15
113	Ti	Cs	Ce	CaO	15.4	33.2	46.3	2	700	15	0.15
114	V	Pd	W	CaO	0.7	30.8	2.4	6	900	10	0.7
115	V	Ce	Hf	CaO	12.3	31.1	39.4	2	750	15	0.15
116	Mn	Tb	Hf	CaO	8.9	27.9	31.8	2	800	10	0.15
117	Mn	Fe	Hf	CaO	7.7	24.5	31.4	2	800	15	0.15
118	Fe	Y	Tb	CaO	9.4	30.4	30.8	2	750	10	0.15
119	Fe	Ba	Ce	CaO	11.6	37.6	30.9	2	750	20	0.15
120	Co	Cu	Nd	CaO	3.2	34.4	9.3	2	900	10	0.15
121	Sr	Cs	La	CaO	8.0	17.2	46.3	4	750	20	0.15
122	Sr	Pd	W	CaO	1.0	33.4	3.0	6	900	15	0.7
123	Y	Mo	Nd	CaO	13.2	40.7	32.5	2	800	20	0.4
124	Ba	Eu	none	CaO	17.0	42.8	39.6	2	750	20	0.15
125	Li	Ti	V	TiO_2	8.4	34.2	24.5	2	850	20	0.15
126	Li	Fe	Ce	TiO_2	11.6	38.2	30.3	2	900	20	0.7
127	Li	Zn	Pd	TiO_2	7.5	35.5	21.1	2	850	20	0.15
128	Na	Fe	Pd	TiO_2	2.1	33.7	6.2	2	850	20	0.15
129	Na	Co	Pd	TiO_2	n.d.	n.d.	n.d.	n.d.	n.d.	n.d.	n.d.
130	Mg	Mn	Ce	TiO_2	14.2	37.4	38.0	2	850	15	0.7
131	Mg	Sr	Tb	TiO_2	10.3	36.4	28.4	2	900	20	0.7
132	Mg	Ti	La	TiO_2	12.0	32.5	37.0	2	850	15	0.7
133	Ca	V	Y	TiO_2	8.6	29.1	29.5	2	800	20	0.4
134	Ti	Zn	La	TiO_2	10.4	28.5	36.4	2	800	20	0.4

135	Ti	Zr	Ce	TiO_2	15.2	38.4	39.6	2	800	20	0.4
136	Ti	Cs	W	TiO_2	16.6	37.8	43.8	2	750	20	0.4
137	Ti	Y	Ce	TiO_2	1.3	24.0	5.5	2	800	10	0.15
138	V	Co	La	TiO_2	8.1	30.8	26.4	2	800	10	0.15
139	V	Co	Ce	TiO_2	5.5	30.8	17.8	2	700	10	0.15
140	V	Ni	Zn	TiO_2	6.1	30.1	20.3	2	800	10	0.15
141	V	Pd	none	TiO_2	n.d.	n.d.	n.d.	n.d.	n.d.	n.d.	n.d.
142	Mn	Fe	Nd	TiO_2	9.4	30.4	31.0	2	750	20	0.4
143	Mn	Cu	Sr	TiO_2	8.2	26.6	30.7	4	850	20	0.15
144	Mn	Nd	W	TiO_2	7.9	37.0	21.4	2	900	20	0.4
145	Fe	Fe	Ni	TiO_2	n.d.	n.d.	n.d.	n.d.	n.d.	n.d.	n.d.
146	Fe	Cu	Sr	TiO_2	8.2	39.6	20.7	2	850	20	0.15
147	Fe	Zn	W	TiO_2	15.4	31.3	49.2	4	850	20	0.15
148	Fe	Sr	Mo	TiO_2	8.3	31.2	26.4	2	800	10	0.15
149	Co	Sr	Hf	TiO_2	13.7	37.3	36.8	2	800	20	0.15
150	Ni	Zn	La	TiO_2	2.1	14.9	14.3	4	750	10	0.7
151	Ni	Ce	W	TiO_2	9.2	30.4	30.3	2	750	10	0.15
152	Ni	Mo	Eu	TiO_2	4.2	25.4	16.5	2	850	20	0.7
153	Cu	Zr	Tb	TiO_2	7.4	37.8	19.6	2	850	20	0.15
154	Cu	Mo	Ce	TiO_2	15.3	38.7	39.5	2	800	20	0.4
155	Cu	La	Tb	TiO_2	10.3	32.5	31.7	2	850	20	0.4
156	Cu	Eu	Eu	TiO_2	5.9	35.8	16.5	2	800	20	0.15
157	Zn	Zn	Nd	TiO_2	11.4	19.0	59.9	4	850	20	0.15
158	Zn	Zr	Tb	TiO_2	12.9	34.4	37.6	2	850	10	0.7
159	Zn	Tb	Hf	TiO_2	11.0	30.4	36.2	2	850	15	0.7
160	Y	Cs	Ce	TiO_2	12.4	39.1	31.8	2	850	20	0.4
161	Y	Nd	Tb	TiO_2	8.7	38.4	22.6	2	850	20	0.15
162	Mo	Ba	Ce	TiO_2	15.4	41.3	37.4	2	850	10	0.7
163	Mo	Ce	Nd	TiO_2	7.0	31.9	21.9	2	900	20	0.7
164	Mo	Ce	W	TiO_2	8.7	34.4	25.4	2	850	20	0.15
165	Cs	Ba	Eu	TiO_2	13.3	39.3	33.9	2	800	20	0.15
166	La	Ce	W	TiO_2	12.5	40.4	31.0	2	850	20	0.15
167	Ce	Nd	Tb	TiO_2	10.8	34.9	31.0	2	800	15	0.4
168	Li	Ca	Ca	ZrO_2	1.3	36.4	3.7	2	850	20	0.15
169	Li	Mo	Nd	ZrO_2	16.7	38.3	43.5	2	700	20	0.4
170	Li	Ba	Nd	ZrO_2	1.1	27.9	4.1	4	900	20	0.7
171	Li	La	Eu	ZrO_2	6.3	31.3	20.1	2	800	20	0.15
172	Li	La	W	ZrO_2	13.6	40.1	34.0	2	850	20	0.7
173	Li	Co	Y	ZrO_2	2.2	26.0	8.5	2	750	10	0.15
174	Li	Tb	none	ZrO_2	6.0	36.8	16.3	2	900	20	0.15
175	Li	K	Mn	ZrO_2	10.7	38.0	28.1	2	750	15	0.15
176	Na	Ba	Nd	ZrO_2	10.5	31.2	33.8	2	750	10	0.15
177	Na	Eu	W	ZrO_2	18.2	40.8	44.6	2	850	20	0.7
178	Na	V	Mo	ZrO_2	8.2	31.5	26.1	2	800	10	0.15
179	Na	K	none	ZrO_2	6.4	38.7	16.6	2	750	20	0.15
180	Mg	V	Hf	ZrO_2	3.2	33.7	9.4	2	850	20	0.15
181	Mg	Zr	W	ZrO_2	9.6	26.8	35.9	2	850	10	0.7
182	K	Ba	Nd	ZrO_2	8.5	29.1	29.2	2	700	20	0.4
183	K	Mn	Zn	ZrO_2	6.2	36.9	16.8	2	750	20	0.15
184	K	Mn	Ce	ZrO_2	6.6	25.6	25.8	2	800	10	0.15
185	K	Pd	Hf	ZrO_2	n.d.	n.d.	n.d.	n.d.	n.d.	n.d.	n.d.
186	Ca	V	Cu	ZrO_2	7.0	26.8	26.2	2	800	10	0.15
187	Ca	Ni	Cu	ZrO_2	6.3	35.6	17.8	2	750	20	0.15
188	Ca	Sr	Zr	ZrO_2	10.4	33.6	31.1	2	700	20	0.4
189	Ca	Cu	Hf	ZrO_2	1.9	31.5	6.1	2	800	20	0.15
190	V	Mn	W	ZrO_2	7.8	34.1	23.0	2	850	20	0.15
191	Mn	Ba	none	ZrO_2	5.4	27.1	20.1	2	750	15	0.15
192	Mn	Tb	Hf	ZrO_2	1.4	46.7	3.0	2	850	10	0.7
193	Mn	Fe	Nd	ZrO_2	4.7	34.2	13.8	2	850	20	0.4
194	Fe	Cu	Zr	ZrO_2	6.1	36.2	16.9	2	850	20	0.15

195	Co	Ce	Nd	ZrO_2	1.2	25.9	4.7	6	800	15	0.7
196	Co	Sr	Ba	ZrO_2	4.9	12.3	39.7	6	900	20	0.7
197	Ni	Cs	Ba	ZrO_2	1.2	39.6	2.9	2	700	20	0.4
198	Ni	Ba	Hf	ZrO_2	1.3	22.0	6.0	6	850	15	0.4
199	Ni	Y	Eu	ZrO_2	1.0	25.9	3.9	6	800	20	0.7
200	Zn	La	Ce	ZrO_2	3.4	35.0	9.8	2	900	20	0.15
201	Y	Mo	Nd	ZrO_2	7.4	30.1	24.5	2	800	15	0.15
202	Pd	Cs	Ba	ZrO_2	n.d.	n.d.	n.d.	n.d.	n.d.	n.d.	n.d.
203	La	Eu	W	ZrO_2	4.8	36.7	13.1	2	850	20	0.4
204	Li	Mg	Zr	BaO	18.6	38.6	48.2	2	800	20	0.7
205	Li	Co	Zn	BaO	6.2	32.7	19.0	2	900	20	0.7
206	Li	Co	Nd	BaO	7.1	17.8	39.9	4	900	20	0.15
207	Li	Co	Eu	BaO	13.8	34.3	40.1	2	800	15	0.15
208	Li	Zr	Cs	BaO	16.4	36.6	44.9	2	850	20	0.7
209	Na	Ca	Mn	BaO	9.0	28.5	31.7	2	800	20	0.4
210	Na	Fe	Ce	BaO	9.3	33.0	28.2	2	850	20	0.4
211	Mg	K	Y	BaO	17.0	37.2	45.6	2	850	20	0.7
212	Mg	V	Mn	BaO	10.2	32.6	31.3	2	750	20	0.15
213	Mg	Mn	Ni	BaO	8.7	30.0	29.1	2	850	20	0.7
214	Mg	Pd	none	BaO	0.8	45.3	1.8	6	900	15	0.7
215	Mg	Ni	W	BaO	9.6	24.9	38.6	2	850	20	0.7
216	K	Ca	Zr	BaO	13.7	36.6	37.3	2	850	20	0.7
217	K	V	Mo	BaO	18.5	32.9	56.3	2	850	20	0.7
218	K	Zr	La	BaO	17.5	37.3	47.0	2	800	15	0.7
219	Ca	Mn	Mo	BaO	10.3	32.5	31.7	2	850	20	0.4
220	Ca	Y	Zr	BaO	11.0	38.3	28.6	2	800	20	0.4
221	Ca	W	none	BaO	6.2	20.9	29.7	2	800	15	0.4
222	V	Mn	Cu	BaO	9.9	34.2	29.1	2	850	15	0.15
223	V	Fe	none	BaO	13.9	29.4	47.1	4	850	20	0.15
224	V	Zr	Eu	BaO	12.9	36.2	35.6	2	900	20	0.7
225	Mn	Y	Hf	BaO	6.1	17.2	35.5	4	900	15	0.15
226	Fe	Ba	La	BaO	14.1	34.6	40.8	2	850	20	0.7
227	Co	Zn	Zr	BaO	12.4	36.2	34.4	2	900	20	0.7
228	Zn	Hf	none	BaO	16.9	36.6	46.0	2	850	20	0.7
229	Sr	Mo	none	BaO	21.2	37.0	57.4	2	850	20	0.7
230	Sr	Ba	Hf	BaO	10.6	35.9	29.6	2	850	20	0.7
231	Mo	Cs	W	BaO	20.2	43.2	46.7	2	850	20	0.7
232	Ce	Nd	Hf	BaO	15.2	35.4	43.0	2	800	20	0.15
233	Li	Fe	Ba	La_2O_3	15.2	35.5	43.0	2	700	10	0.15
234	Li	Y	Eu	La_2O_3	15.4	35.9	42.8	2	700	15	0.15
235	Li	Ba	La	La_2O_3	15.0	37.8	39.6	2	750	20	0.4
236	Li	Nd	Tb	La_2O_3	10.3	30.6	33.8	2	700	10	0.15
237	Na	Ca	none	La_2O_3	15.4	33.5	45.9	2	700	20	0.15
238	Na	Fe	Tb	La_2O_3	7.5	31.7	23.6	2	850	10	0.15
239	Na	Pd	W	La_2O_3	1.3	37.5	3.5	4	900	15	0.7
240	Mg	K	Fe	La_2O_3	11.1	19.7	56.3	4	750	20	0.15
241	Mg	Ca	Nd	La_2O_3	16.2	39.1	41.3	2	750	20	0.4
242	K	Co	Ce	La_2O_3	2.4	24.4	9.7	2	800	15	0.15
243	K	Cu	none	La_2O_3	7.5	38.4	19.6	2	850	20	0.15
244	K	none	none	La_2O_3	7.9	29.4	27.0	2	800	10	0.15
245	Ca	Mn	Sr	La_2O_3	10.6	32.0	33.2	2	700	20	0.15
246	Ca	Fe	Tb	La_2O_3	12.3	32.3	38.0	2	750	10	0.15
247	Ca	Pd	Tb	La_2O_3	n.d.	n.d.	n.d.	n.d.	n.d.	n.d.	n.d.
248	Ti	Co	Cu	La_2O_3	1.3	18.3	7.1	6	900	20	0.15
249	Ti	Co	Pd	La_2O_3	0.6	40.6	1.5	2	700	20	0.4
250	Ti	Zr	Ba	La_2O_3	4.1	33.1	12.4	2	700	20	0.15
251	Ti	Ni	Hf	La_2O_3	9.6	36.4	26.4	2	900	20	0.7
252	V	Fe	Mo	La_2O_3	7.7	34.2	22.5	2	800	20	0.15
253	V	Mo	none	La_2O_3	14.9	41.5	35.8	2	900	20	0.7
254	V	La	W	La_2O_3	14.1	34.6	40.8	2	850	20	0.7

255	V	Ce	Nd	La_2O_3	8.4	30.6	27.3	2	700	20	0.15
256	Mn	Sr	Mo	La_2O_3	10.8	29.3	36.9	2	700	15	0.15
257	Fe	Cu	Zr	La_2O_3	4.9	33.0	14.7	2	850	20	0.15
258	Fe	Nd	Tb	La_2O_3	13.4	32.3	41.5	2	700	10	0.15
259	Ni	Hf	none	La_2O_3	0.9	41.2	2.2	2	750	20	0.4
260	Cu	Mo	Pd	La_2O_3	0.5	28.2	1.8	6	900	20	0.7
261	Cu	La	W	La_2O_3	8.2	37.7	21.6	2	850	20	0.15
262	Zn	Y	none	La_2O_3	15.1	40.9	36.9	2	750	20	0.15
263	Zn	Zr	Cs	La_2O_3	12.2	38.0	32.1	2	750	20	0.15
264	Sr	Y	Ce	La_2O_3	14.8	37.1	39.9	2	700	15	0.15
265	Mo	Cs	Tb	La_2O_3	13.3	30.1	44.2	2	700	10	0.15
266	Pd	Ce	Tb	La_2O_3	1.1	30.8	3.6	6	900	10	0.7
267	Ba	Ce	Hf	La_2O_3	13.9	39.4	35.4	2	750	20	0.15
268	La	Tb	none	La_2O_3	7.8	29.9	26.2	2	750	20	0.15
269	Tb	Hf	W	La_2O_3	15.2	41.7	36.5	2	750	20	0.15
270	Na	K	V	CeO_2	6.6	34.3	19.4	2	850	20	0.15
271	Na	V	Y	CeO_2	7.3	38.3	19.1	2	850	20	0.15
272	Mg	K	none	CeO_2	8.5	28.8	29.6	2	800	10	0.15
273	Mg	Fe	none	CeO_2	7.0	27.5	25.5	2	800	10	0.15
274	Mg	Ni	Zn	CeO_2	1.3	26.7	4.9	6	800	20	0.15
275	K	Co	Sr	CeO_2	6.4	32.8	19.5	2	900	20	0.4
276	K	La	Ce	CeO_2	13.4	32.3	41.5	2	700	10	0.15
277	K	Ce	Eu	CeO_2	5.1	34.4	14.8	2	900	20	0.4
278	Ti	Ni	Ba	CeO_2	4.8	36.2	13.2	2	750	15	0.7
279	Ti	Zn	Pd	CeO_2	1.2	26.0	4.6	2	800	15	0.15
280	V	Sr	W	CeO_2	1.7	24.6	7.0	6	850	20	0.4
281	V	Zr	Nd	CeO_2	7.5	35.5	21.1	2	850	20	0.15
282	V	Pd	W	CeO_2	1.6	42.9	3.7	2	800	10	0.7
283	Mn	Ni	Zn	CeO_2	n.d.	n.d.	n.d.	n.d.	n.d.	n.d.	n.d.
284	Mn	Ni	Y	CeO_2	2.9	32.2	9.1	2	900	20	0.4
285	Mn	Sr	La	CeO_2	8.6	35.0	24.7	2	850	20	0.15
286	Mn	Y	Zr	CeO_2	6.6	26.8	24.8	2	800	10	0.15
287	Mn	Ba	La	CeO_2	8.6	34.9	24.7	2	850	20	0.15
288	Mn	none	none	CeO_2	4.9	28.7	17.1	2	800	20	0.15
289	Mn	Eu	Hf	CeO_2	6.2	35.1	17.7	2	800	20	0.15
290	Fe	Zn	La	CeO_2	3.5	24.1	14.7	2	800	10	0.15
291	Fe	Y	La	CeO_2	5.1	25.9	19.5	2	800	10	0.15
292	Ni	Sr	Nd	CeO_2	10.2	34.4	29.8	2	800	20	0.4
293	Ni	Nd	Eu	CeO_2	8.3	32.1	25.9	2	900	20	0.7
294	Zn	Pd	Ce	CeO_2	2.2	32.3	6.8	2	800	20	0.15
295	Zn	La	Nd	CeO_2	9.2	27.9	32.9	2	750	10	0.15
296	Sr	Cs	none	CeO_2	12.5	36.1	34.8	2	800	20	0.4
297	Sr	Ce	none	CeO_2	10.9	33.9	32.1	2	700	20	0.15
298	Y	Zr	Eu	CeO_2	7.2	35.6	20.2	2	850	20	0.15
299	Mo	Pd	Ba	CeO_2	0.7	33.3	2.1	2	800	15	0.4
300	Cs	Ce	Nd	CeO_2	5.9	30.7	19.1	2	800	15	0.15

[a]The catalyst composition is expressed in the form of M1–M2–M3/Support. The three active elements (M1–M3) are sorted along the atomic number.

[b]The best C_2 yield of individual catalysts is reported together with the corresponding parameters. The performance of 9 catalysts was not determined due to sintering at the calcination temperature. The corresponding cells are filled with n.d.

[c]The reaction in the absence of catalysts led to the C_2 yield of 10.2% with the corresponding CH_4 conversion of 29.7% and the C_2 selectivity of 34.3% at the temperature of 850 °C, the CH_4/O_2 ratio of 2 mol/mol, the total flow of 20 mL/min, and P_{Ar} of 0.15 atm.

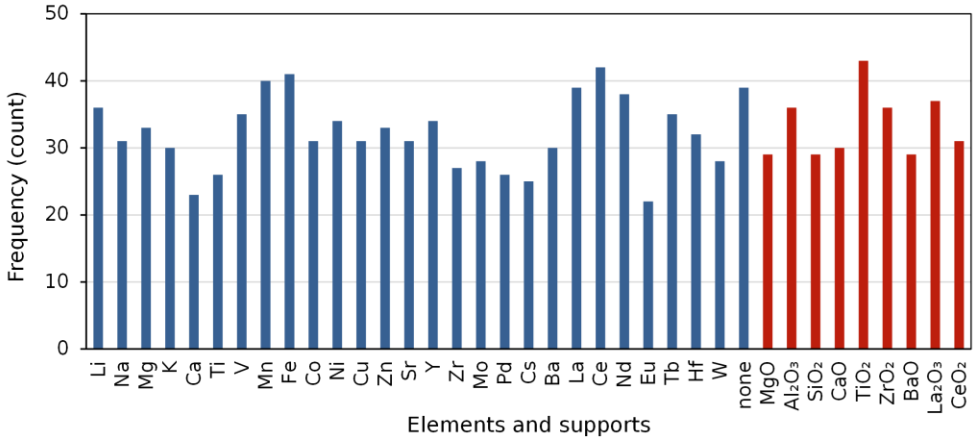

Figure 4.1. Frequency of appearance of individual elements and supports in 300 catalysts.

4.2.3. Catalyst evaluation

In Chapter 2, a HTS instrument was developed [30]. Here, a brief description of the instrument is given. A gas generator supplies a $CH_4/O_2/Ar$ mixture with the flow volume of the three gases individually controlled. The mixture is equally split into 20 reaction quartz tubes (4 mm to 2 mm of I.D.) bearing catalyst beds. The reaction tubes are symmetrically placed in a hollow electric furnace with three temperature zones (T_1–T_3 from the feed side to the effluent side), where the catalyst beds are placed at the center zone. The effluent gas from the 20 tubes is sequentially sampled by an autosampler, and transferred to a quadruple mass spectrometer (QMS, Transpector CPM 3, INFICON). Mass signals are converted into the relative pressure of individual gases based on external calibrations. Cooperation among the programmed gas generation, temperature, and autosampling enables full automation in evaluating the performance of 20 catalysts for a predetermined set of reaction conditions. The acquisition of the performance of 20 catalysts at one steady-state condition typically takes 6–7 min. Further details are found in Chapter 2 [30], where the experimental reproducibility and consistency were fully demonstrated.

The programmed sequence of reaction conditions employed in this chapter is shown in Figure 4.2. The catalyst bed height was fixed at 10 mm, assuming a gas hourly space velocity

(GHSV) as a known key descriptor in OCM [27,30]. Catalysts were first activated at 1000 °C for 160 min under O_2. Then, the temperature was stepwise decreased from 900 to 850, 800, 750, and 700 °C. At each temperature, the total flow volume (10, 15, 20 mL/min/channel, corresponding to the contact time of 0.75, 0.50, 0.38 s, respectively), the CH_4/O_2 ratio (2, 4, 6 mol/mol), and the Ar concentration (P_{Ar} = 0.15, 0.40, 0.70 atm) were stepwise varied. Combined variations in the temperature, the total flow volume, the CH_4/O_2 ratio, and P_{Ar} lead to 135 conditions per catalyst and 2700 observations for 20 catalysts in a single automated operation.

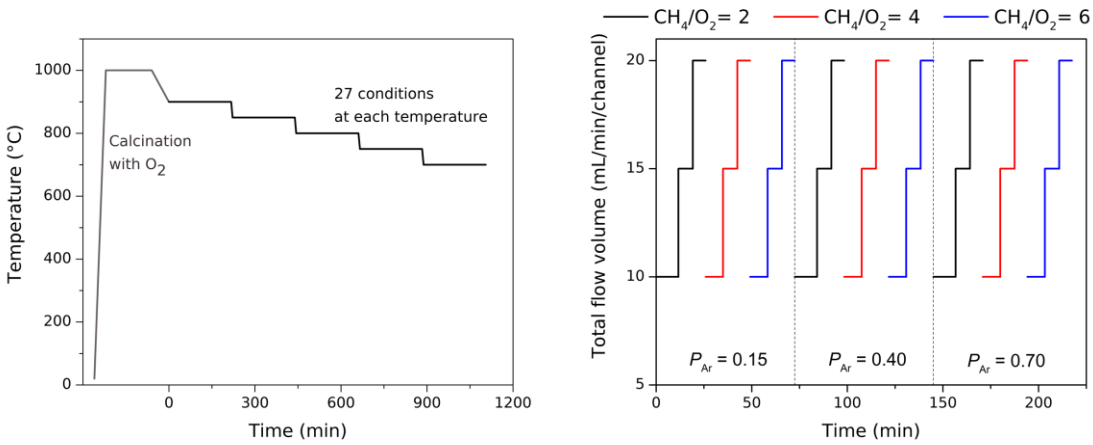

Figure 4.2. Programmed sequence of reaction conditions. Each temperature step includes a program for the gas flow.

4.2.4. Data preprocessing

The evaluation of 291 catalysts (9 catalysts could not be evaluated) at 135 conditions afforded an OCM dataset consisting of 39,285 data points. The dataset denotes the correspondence between the catalyst composition and the performance at individual reaction conditions. In cost of exploring many unreported catalysts over a wide variety of conditions, I found i) severe sintering of some catalysts (e.g. No. 202: Pd–Cs–Ba/ZrO_2) during in-line calcination at 1000 °C, and ii) carbon deposition at specific conditions. These problems resulted

in unnaturally high CH_4 conversion and/or very poor carbon balance. Such data points were safely excluded from any data analysis.

4.2.5. Data analysis

Decision tree classification was performed within the scikit-learn package of Python [31]. A decision tree is built by recursive partitioning. It starts from the root node (or called parent node) and splits into the left and right child nodes. These child nodes can then be further split and consequently, they become parent nodes of their resulting children nodes. Data is split on a feature which maximizes the information gain factor (*IG*) defined as follows,

$$IG(D_p, f) = I(D_p) - \left(\frac{N_{left}}{N_p} I(D_{left}) + \frac{N_{right}}{N_p} I(D_{right}) \right)$$

where f is a feature to perform the split. D_p, D_{left}, and D_{right} are the data of the parent node and the two child nodes, respectively. N_p, N_{left}, and N_{right} are the numbers of the samples at the parent node and the child nodes, respectively. I is defined as an imputity measure, which is used to define the homogeneity of the node. In this report, the Gini Index was used [31].

In this thesis, since our catalyst dataset is small, applying pruning methods on decision tree is not reasonable and results in derived knowledge become too general. Hence, decision tree was kept split until all leaf nodes were pure (dataset are completely split). The final conclusions will be extracted after reviewing several decision trees generated by different training set in order to avoid biases.

4.3. Results and discussions

4.3.1. Catalyst data acquisition, visualization, and interpretation

300 catalysts were generated based on random numbers. They were prepared, and evaluated using the HTS instrument. 9 catalysts (Nos. 73,81,129,141,145,185,202,247,283) were not evaluated due to severe sintering in the calcination step. The evaluation of the remaining 291 catalysts in 135 conditions afforded 39,285 data points, which are visualized using a scatter plot for the CH_4 conversion vs. the C_2 selectivity (Figure 4.3). As demonstrated in Chapter 2 [30], the scatter plot visualization for the entire dataset provides a facile description of a general behavior of catalysis. For instance, it dictates i) a conversion-selectivity tradeoff for determining the upper limit of the C_2 yield (Figure 4.3a), and ii) the temperature and the CH_4/O_2 ratio as the two most influential conditions.

Here, according to the scope of the study, I rather focus on a relationship between the composition and the OCM performance. The performance of the 291 catalysts was compared in terms of the best C_2 yield that individual catalysts gave among the 135 conditions. The comparison at one fixed set of reaction conditions was not adopted as different catalysts usually possess their own sweet spots. Thus such comparison may find catalysts which are not actually very performant but just suitable for the selected set of conditions. This is especially important when a wide variety of catalysts are tested as in the current study. Besides, the OCM is known to be process-sensitive [27,32,33]. Figure 4.4 summarizes the distribution of 291 data points corresponding to the best C_2 yield data of the 291 catalysts. The star mark represents the data point of the best C_2 yield achieved in the absence of catalysts as a reference. It is known that the OCM reaction can proceed even in the absence of catalysts via a free radical mechanism in the gas phase [10,34]. In the current case, the catalyst-free OCM gave at best ca. 10% of the C_2 yield. Considering 10% as a standard, there were catalysts which could improve the C_2 yield and those which deteriorated it by mediating combustion of CH_4 into CO_x. Here, I classified

catalysts into three cases based on the best C_2 yield: i) Positive (> 13%), ii) neutral (7–13%), and iii) negative (< 7%). The C_2 yield range of 10 ± 3% for the classification was determined firstly to be symmetric with respect to the catalyst-free C_2 yield of 10%, secondly to be sufficiently larger than the experimental error of below 1% [30], and lastly to have a sufficient number of catalysts in each of the three cases. The number of positive, neutral, and negative catalysts was 51, 134, and 106, respectively. In Figure 4.4a, it is seen that the best C_2 yield of the 291 catalysts is distributed in the range of 0–21%. Their average (8.3%) was found to be lower than 10% as the standard, while a relatively large number of catalysts were classified to be positive even though they were randomly picked up. The latter observation plausibly reflects the fact that the library contains a relatively large number of basic elements and supports (to be basic is one of known requirements for OCM catalysts [27,28]. When the distribution of the data points is seen in terms of the CH_4 conversion and C_2 selectivity (Figure 4.4b,c), it is clear that the selectivity was the reason of differentiating the best C_2 yield of the catalysts. As for the distribution in the reaction conditions, almost all the positive catalysts attained the best C_2 yield at the CH_4/O_2 ratio of 2 (Figure 4.4d). The percentage of positive catalysts increased along with the decrease of the reaction temperature (Figure 4.4e), while there was no noticeable trends for the total flow (cf. contact time) and P_{Ar} (cf. CH_4 concentration) (Figure 4.4f,g). In summary, the distribution analysis suggests that positive catalysts are such those which can retain high C_2 selectivity at a high O_2 concentration and/or can maintain the conversion at a low temperature.

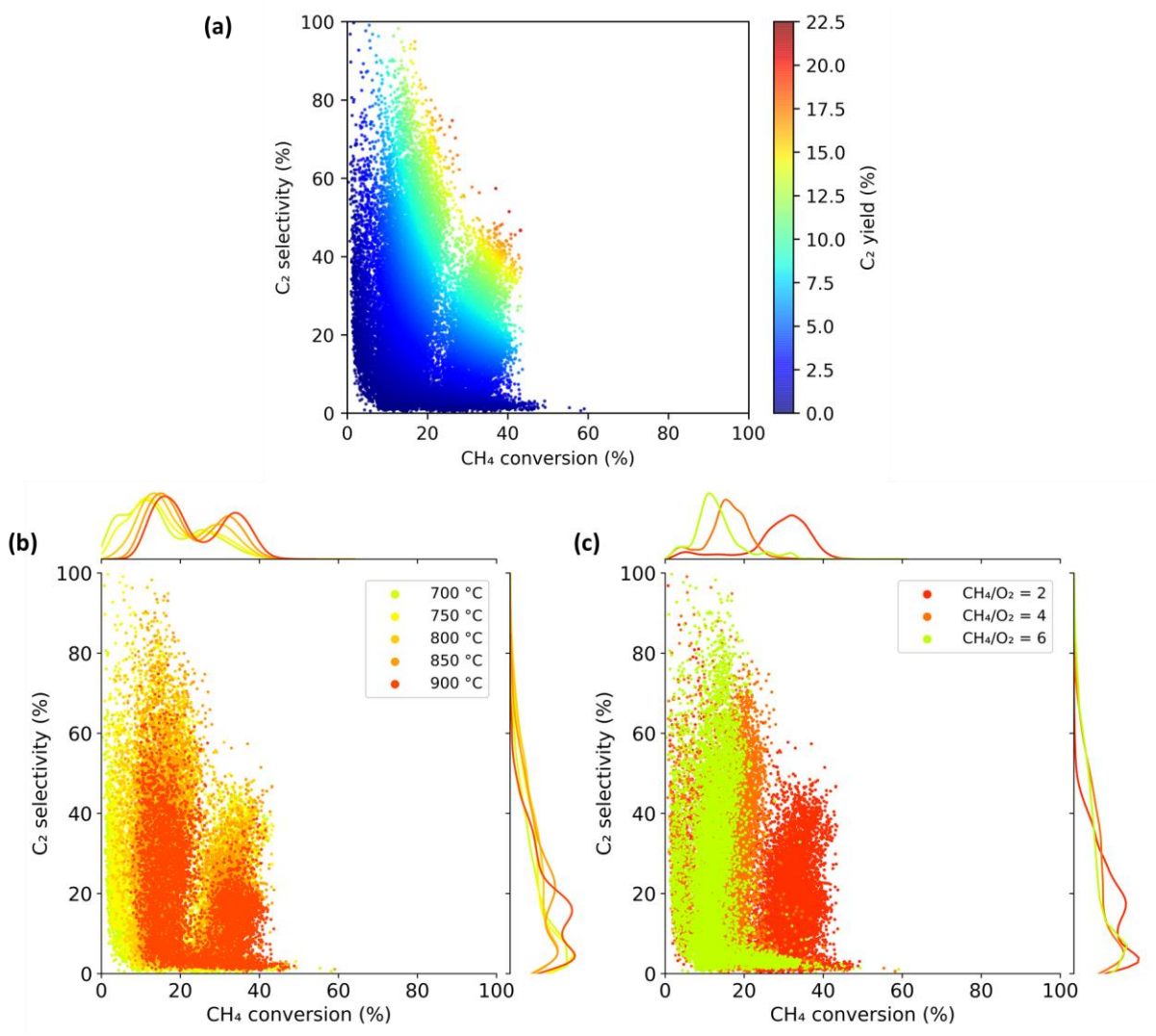

Figure 4.3. Visualization of the entire OCM dataset for 291 catalysts based on scatter plots: (a) CH_4 conversion vs. C_2 selectivity with the C_2 yield indicated by the color. The distribution of data points in terms of (b) the temperature and (c) the CH_4/O_2 ratio.

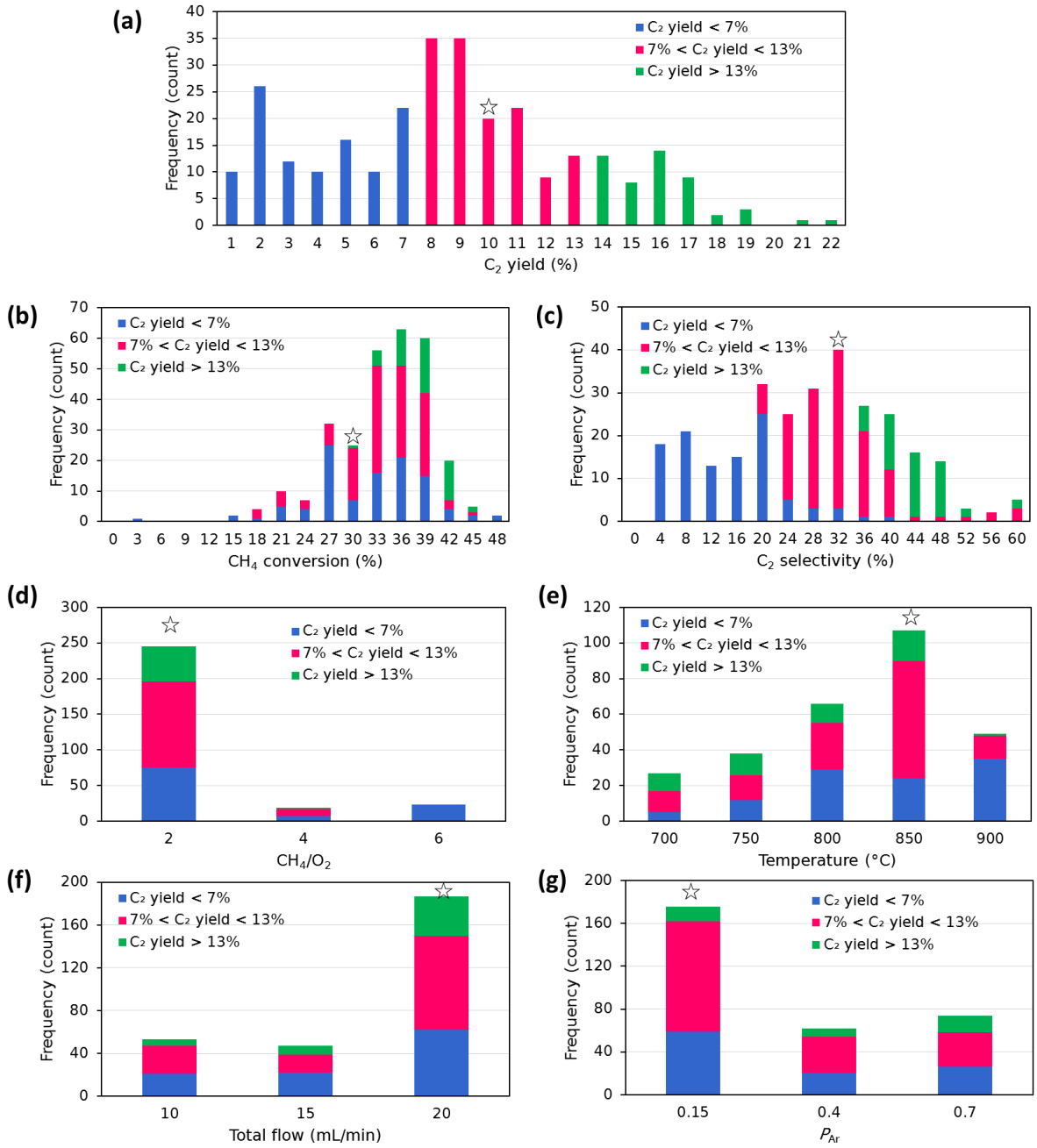

Figure 4.4. Data distributions corresponding to the best C_2 yield for 291 catalysts: (a) C_2 yield, (b) CH_4 conversion, (c) C_2 selectivity, (d) CH_4/O_2 ratio, (e) temperature, (f) total flow, and (g) partial pressure of Ar (atm). The colors reflect the C_2 yield. The star corresponds to the data point taken without catalysts.

Figure 4.5 shows the same scatter plots with those of Figure 4.3 using only the best C_2 yield data points, where the corresponding catalyst names are written as long as the space

allows. One can glance at elements and supports which frequently appear in positive and negative catalysts. For example, positive catalysts are often associated with the presence of Sr, Mg, Mo, and BaO, while negative catalysts often accompany Cu, Pd, Ce, Al_2O_3, etc. However, one also notices that the inclusion of specific components does not necessarily leads to positive or negative catalysts. For example, Ce appears in some of positive catalysts, and Mo is occasionally included in negative catalysts. This fact suggests that the performance is not determined by the presence of one specific component, but combination effects are important. When the scatter plot is colored based on the important reaction conditions, further information can be extracted. Most of positive catalysts attained the best C_2 yield at the CH_4/O_2 ratio of 2 (as was mentioned in Figure 4.4d). A higher CH_4/O_2 ratio appeared only when the catalysts were scarcely selective or not sufficiently selective at a lower CH_4/O_2 ratio (Figure 4.5b). A high C_2 yield was rarely obtained at 900 °C, as few catalysts can retain the selectivity at such a harsh condition (Figure 4.5c). Positive catalysts with group 6 elements tended to give the best C_2 yield at 850 °C. In particular, two entries, Sr–Mo–none/BaO and K–V–Mo/BaO, exhibited very high C_2 selectivity at 850 °C. Some of positive catalysts exhibited the best performance at 700 °C, the employed lowest temperature. As known in literature [35,36], these catalysts mostly contained rare-earth elements such as Ce and La_2O_3. The random exploration identified 5 catalysts whose best C_2 yield exceeds 18%, which were Na–Eu–W/ZrO_2, Li–Mg–Zr/BaO, K–V–Mo/BaO, Sr–Mo–none/BaO, Mo–Cs–W/BaO. These catalysts were never reported in literature.

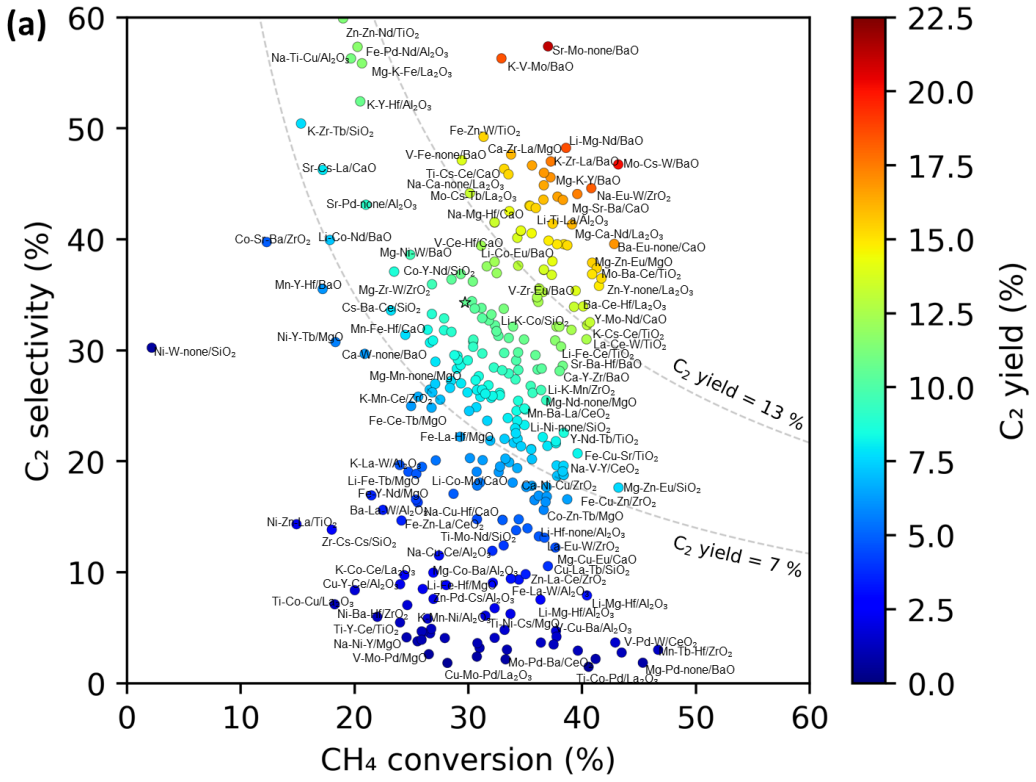
(a)
C₂ selectivity (%)
CH₄ conversion (%)
C₂ yield (%)
C₂ yield = 13 %
C₂ yield = 7 %
0
10
20
30
40
50
60
0.0
2.5
5.0
7.5
10.0
12.5
15.0
17.5
20.0
22.5

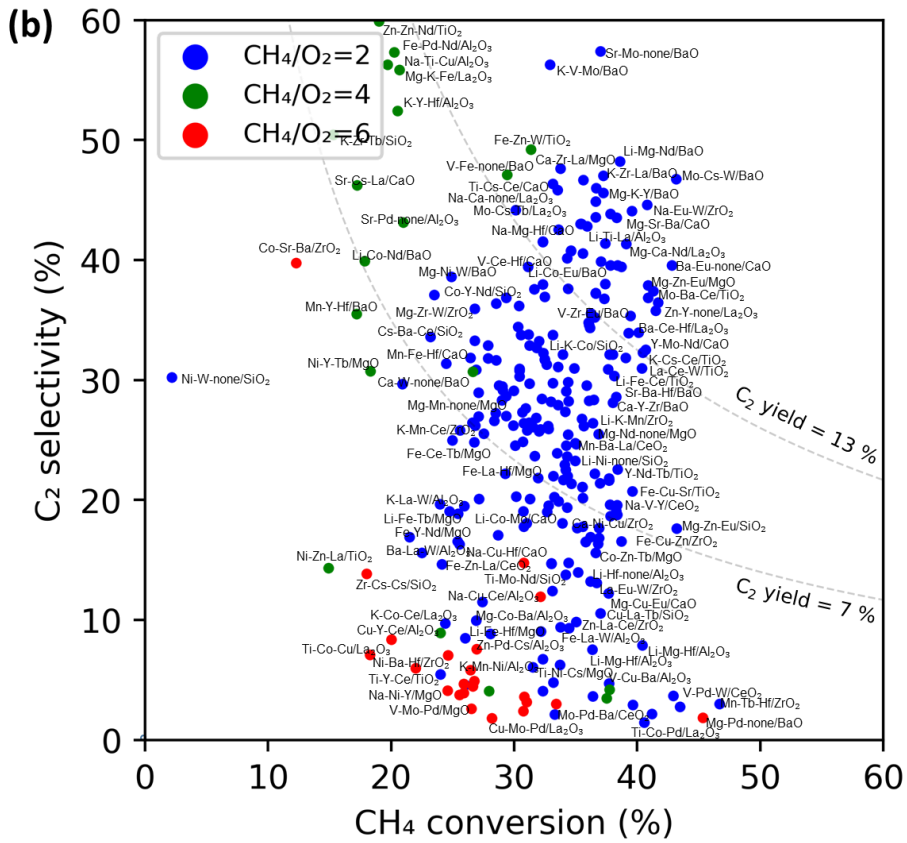
(b)
CH₄/O₂=2
CH₄/O₂=4
CH₄/O₂=6
C₂ selectivity (%)
CH₄ conversion (%)
C₂ yield = 13 %
C₂ yield = 7 %
0
10
20
30
40
50
60

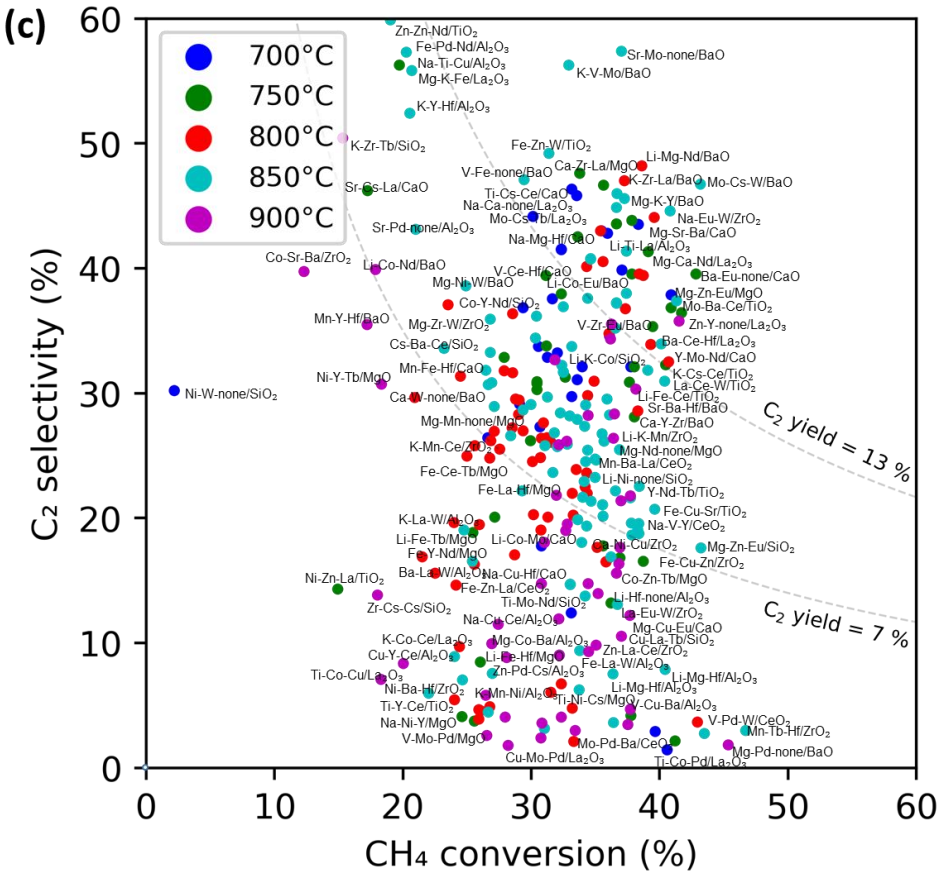

Figure 4.5. Scatter plots of the best C_2 yield data points for 291 catalysts. (a) The C_2 yield is indicated in the color axis. The distribution of data points in terms of (b) the CH_4/O_2 ratio and (c) the temperature. The star corresponds to the data point taken without catalysts.

Figure 4.6 shows the frequency of appearance of individual elements and supports in positive and negative catalysts. In the whole catalysts, individual components were relatively evenly sampled (see Figure 4.1). However, when analyzed in relation to their performance, some biased are seen in the frequency. Out of 51 positive catalysts, 21 catalysts used oxides of group 2 elements (CaO and BaO) as the support, and the other 13 used La_2O_3. As for the active elements (M1–M3), Li > (Mg, Mo, Ce, Eu) > (Ba, La, Hf) appeared relatively frequently. In an earlier publication by Zavyalova et al., it was reported that performant OCM catalysts in literature frequently contained Li > Mg > Na > Ca > La > Ba > Sr as active elements [27]. Indeed, Figure 4.6a finds Li and Mg as specifically positive elements, but not for the other

elements. The origin of this discrepancy would be explained as follows: Previous studies explored catalysts mainly in a way to develop serendipitously identified seeds, while the present study made exploration without preknowledge. For example, Na and Sr are elements which are included in Mn–Na_2WO_4/SiO_2 and La–Sr/CaO as the two most famous OCM catalysts, but they were not frequently observed in my positive catalysts. This fact suggests that these two elements strictly choose combinations, otherwise I was unlucky. Among the 106 negative catalysts, redox-active and/or acidic supports such as Al_2O_3, ZrO_2, and CeO_2 were frequently observed. For active elements, mid to late transition metal elements from groups 7–12 were found as popular choice, while they rarely appeared in the positive catalysts. The reason to regard Mn of Mn–Na_2WO_4/SiO_2 as a negative element must be similarly explained.

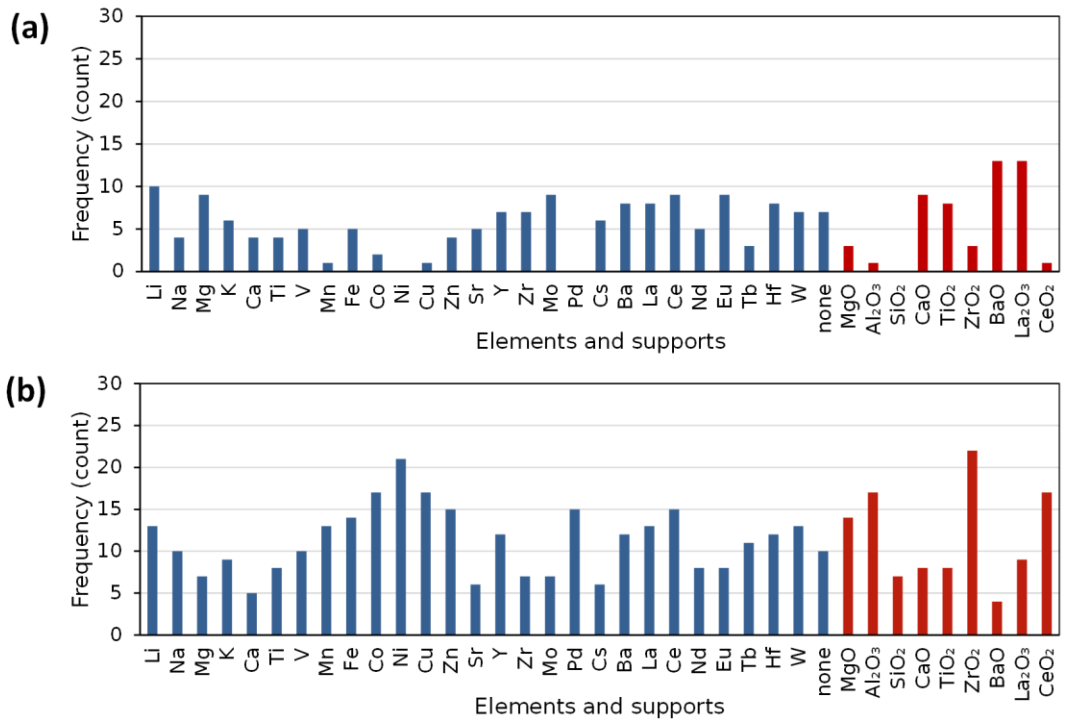

Figure 4.6. Frequency of appearance of individual elements and supports in (a) positive catalysts (C_2 yield > 13%) and (b) negative catalysts (C_2 yield < 7%).

The data analysis for the individual components suggested the importance of combinations in designing good OCM catalysts. For example, Li, which is known as the most

positive element in literature [24,27,37], frequently appeared not only in the positive catalysts but also in the negative ones (Figure 4.6). Figure 4.7 shows the average performance of individual elements and supports, which was derived by averaging the best C_2 yields of catalysts which contained specified components. The huge standard deviations indicate that the performance of individual components was quite sensitive to the remaining three components in the ternary system. According to these considerations, I next analyzed the performance of binary combinations. The best C_2 yields were averaged over catalysts which contained a specific binary combination (A*B), and this value was compared with the averages of the best C_2 yields of catalysts which contained only either of the components (A or B). The 291 catalysts are far from being sufficient to cover a huge number of potential combinations present in the original library, and many combinations were not included in any of the 291 catalysts. Here, the analysis was made for combinations whose frequency of appearance reached at least twice. Figure 4.8 shows the best and worst 20 binary combinations. It is obvious that the best and worst combinations were composed by specific elements and supports: BaO > (Zr, Cs) > (Mo, Ba) for the best side, and Pd >> Ni > W for the worst side. Further, when one categorizes different elements and supports (the cationic elements of oxides) based on the groups in the periodic table, rules of making positive and negative binary combinations become clear. The best 20 combinations were mostly explained by the combination of a 1A or 2A element with an element of either 2A, 4A, 6A, or lanthanoid series. The combinations between 1A, 2A, and lanthanoid series elements evoke well-known Li/MgO, La–Sr/CaO, CeO_2–La_2O_3 [27,34,38], while the combinations between basic elements (1A, 2A) and early transition metal elements (3A, 4A, 6A) evoke similarly well-known Na_2WO_4. However, our observations were totally different from those of the known catalysts in terms of the choice of elements: e.g. (Cs/BaO, K/BaO) vs. Li/MgO, and (Cs–W, Cs–W, Mo–BaO) vs. Na–W. The findings of these novel combinations would not have been achieved without the truly multidimensional exploration of

a huge materials space. Another advantage of such exploration is at the generalization of results towards a catalyst design concept: The combinations between basic elements (1A, 2A) and early transition metal elements (3A, 4A, 6A) suggest that d^0 metallic salts are effective for OCM. For the worst combinations, 80% of the combinations contained 9A or 10A elements. These elements strongly depress the performance of positive elements (1A, 2A, 4A, and lanthanoid series).

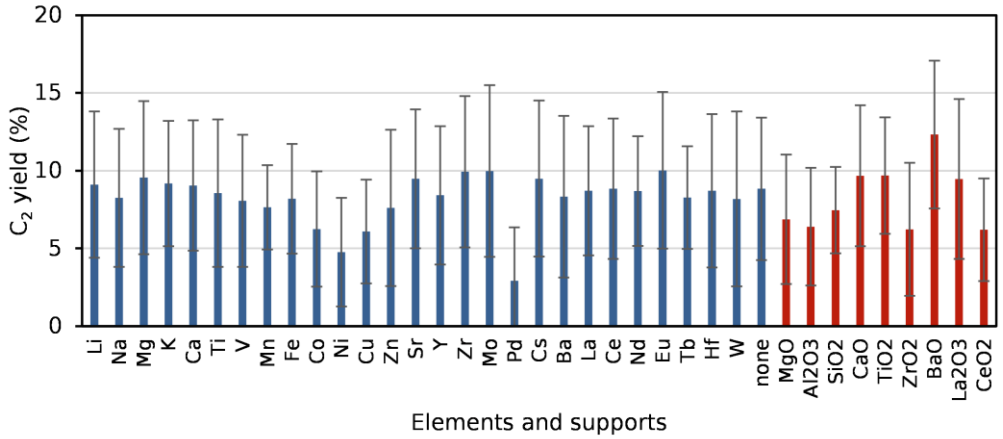

Figure 4.7. Performance of individual elements and supports. The best C_2 yields were averaged among catalysts containing a specific element or support.

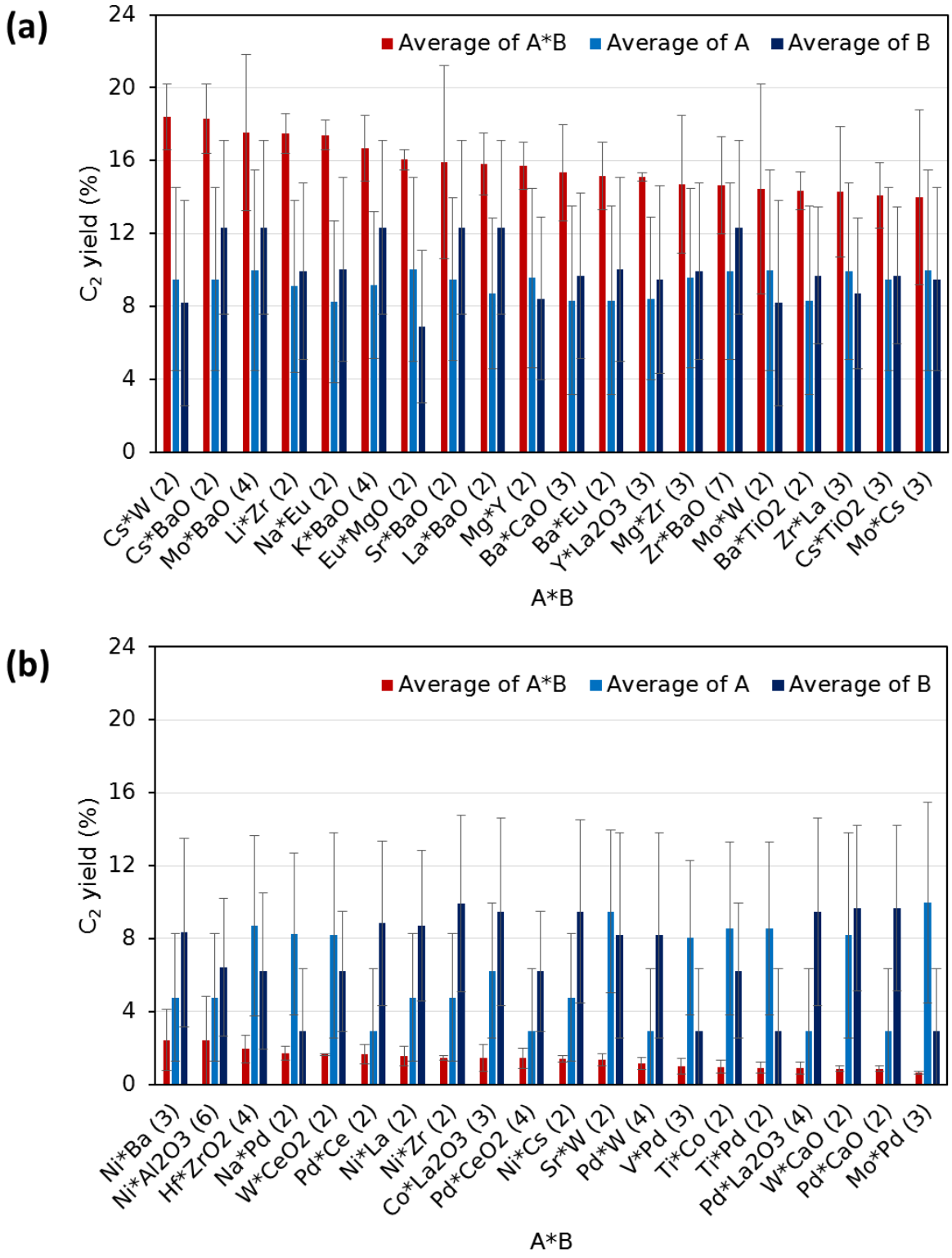

Figure 4.8. (a) Best and (b) worst 20 binary combinations. The best C_2 yields were averaged among catalysts containing a specific combination (A*B), and those containing either of the components (A or B). The numbers in the parentheses correspond to the frequency of

appearance of specific combinations in 291 catalysts. Note that the large error bars came from the fact that the performance was largely influenced by the choice of the other two components in the ternary system, and had nothing to do with the experimental error (below ±1%).

Figure 4.9 compares the average C_2 yield of a specific binary combination (A*B) with a synergy factor of the corresponding combination, which corresponds to the average C_2 yield of A*B normalized by the average C_2 yield of catalysts containing either of A and B. The synergy factor compares how performant a combination is with respect to the individual usage of its constituents. The highly linear correlation most clearly evidences the significance of choosing synergistic combinations in the design of performant OCM catalysts.

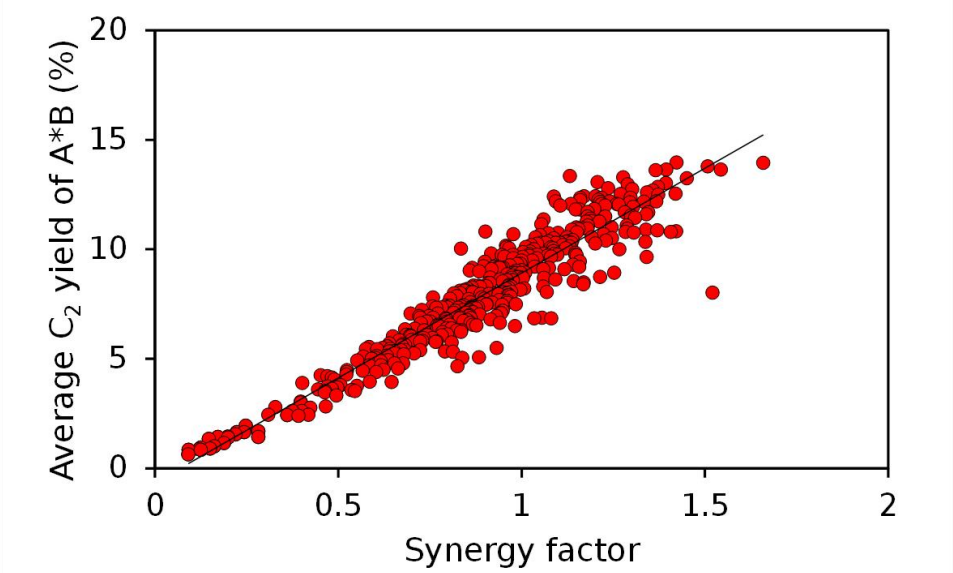

Figure 4.9. Relationship between the performance of catalysts and the presence of synergestic combinations. The average C_2 yield of catalysts with a specific combination (A*B) is compared with a synergy factor. The synergy factor is defined by the ratio of the average C_2 yield for catalysts with A*B with respect to that for catalysts with either of A and B.

4.3.2. Decision tree classification

The results in 4.3.1 figured out two important ideas that the OCM performance of catalysts could be represented by combinations and that there were generalizable combination

rules based on the elemental groups. Here, in order to derive a general model being directly useful for the design of new catalysts, I made the decision tree classification. The classification was rendered in a way that the C_2 yield of the catalysts was divided into two classes: 0–13% (Class 1: not positive), and higher than 13 % (Class 2: positive). Then, my target was to deduce the rules and heuristics that can better classify the catalysts into the two classes.

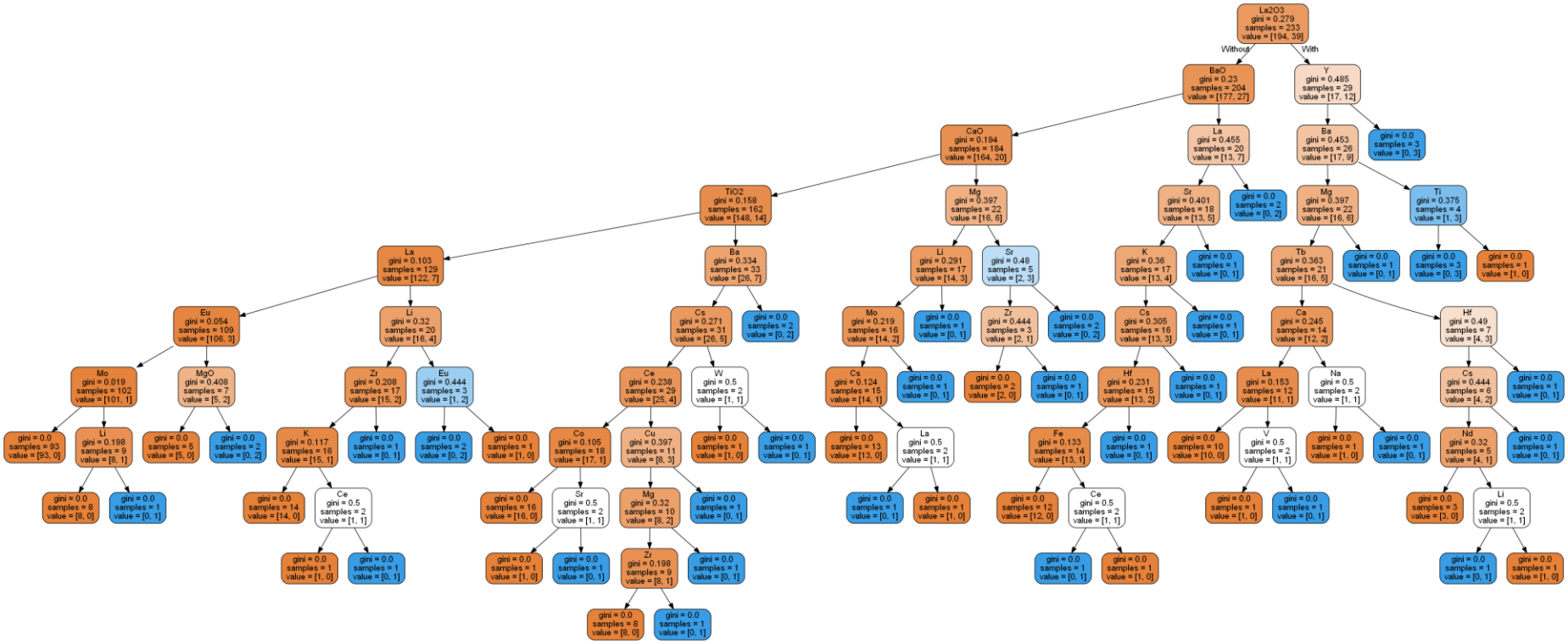

Figure 4.10. Decision tree generated from 233 catalysts which were randomly selected from the 291 catalysts where catalyst descriptors are the presence/absence of specific elements in the composition. The number in square brackets indicates the number of catalysts in class 1 and 2 in each node. Left of a node indicates without/absence of an element, while right of a node indicates with/presence of an element.

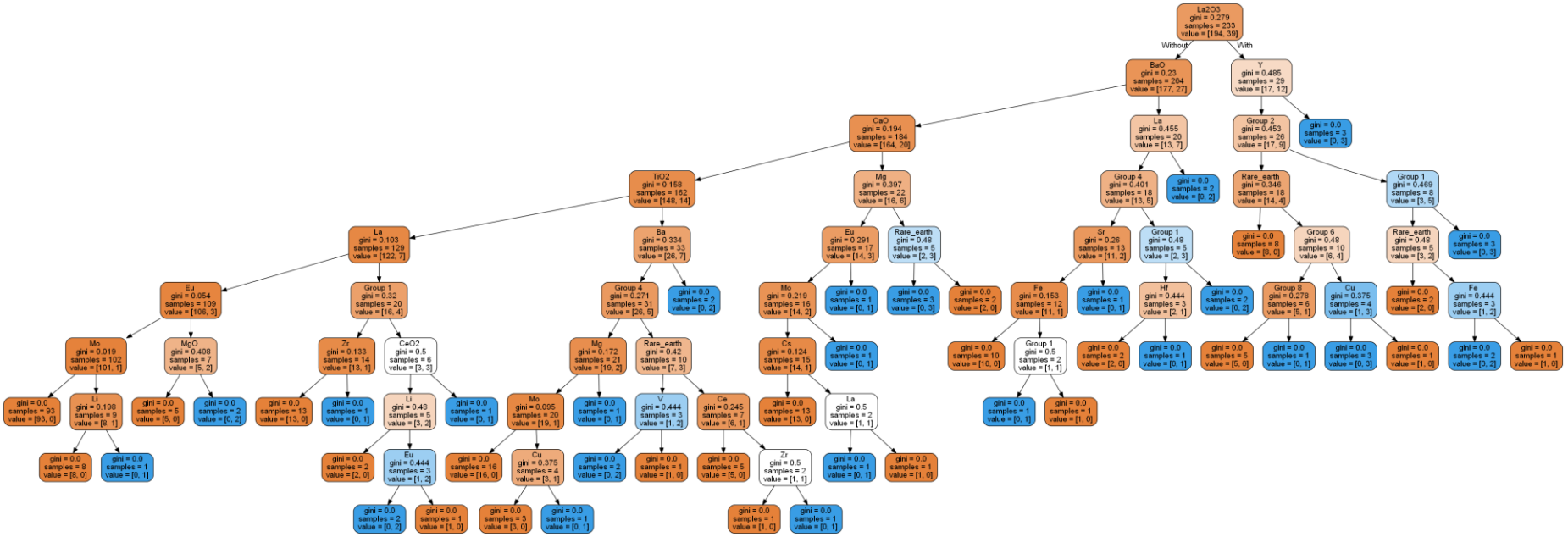

Figure 4.11. Decision tree generated from 233 catalysts which were randomly selected from the 291 catalysts where catalyst descriptors are the presence/absence of specific elements in the composition and their group (1-12) in periodic table. The number in square brackets indicates the number of catalysts in class 1 and 2 in each node. Left of a node indicates without/absence of an element, while right of a node indicates with/presence of an element.

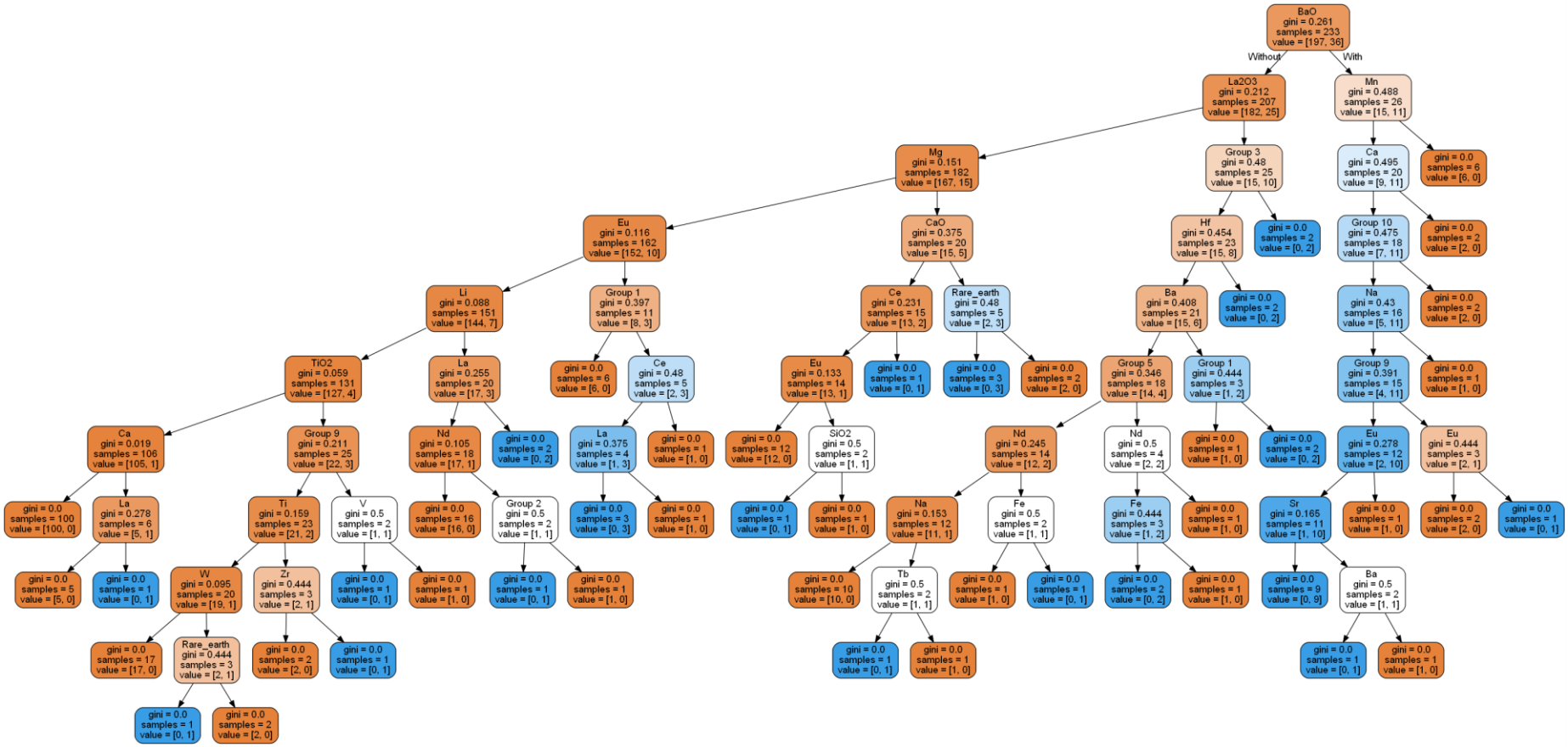
BaO
gini = 0.261
samples = 233
value = [197, 36]
Without
With
La2O3
gini = 0.212
samples = 207
value = [182, 25]
Mn
gini = 0.488
samples = 26
value = [15, 11]
Mg
gini = 0.151
samples = 182
value = [167, 15]
Group 3
gini = 0.48
samples = 25
value = [15, 10]
Ca
gini = 0.495
samples = 20
value = [9, 11]
gini = 0.0
samples = 6
value = [6, 0]
Eu
gini = 0.116
samples = 162
value = [152, 10]
CaO
gini = 0.375
samples = 20
value = [15, 5]
Hf
gini = 0.454
samples = 23
value = [15, 8]
gini = 0.0
samples = 2
value = [0, 2]
Group 10
gini = 0.475
samples = 18
value = [7, 11]
gini = 0.0
samples = 2
value = [2, 0]
Li
gini = 0.088
samples = 151
value = [144, 7]
Group 1
gini = 0.397
samples = 11
value = [8, 3]
Ce
gini = 0.231
samples = 15
value = [13, 2]
Rare_earth
gini = 0.48
samples = 5
value = [2, 3]
Ba
gini = 0.408
samples = 21
value = [15, 6]
gini = 0.0
samples = 2
value = [0, 2]
Na
gini = 0.43
samples = 16
value = [5, 11]
gini = 0.0
samples = 2
value = [2, 0]
TiO2
gini = 0.059
samples = 131
value = [127, 4]
La
gini = 0.255
samples = 20
value = [17, 3]
gini = 0.0
samples = 6
value = [6, 0]
Ce
gini = 0.48
samples = 5
value = [2, 3]
Eu
gini = 0.133
samples = 14
value = [13, 1]
gini = 0.0
samples = 1
value = [0, 1]
gini = 0.0
samples = 3
value = [0, 3]
gini = 0.0
samples = 2
value = [2, 0]
Group 5
gini = 0.346
samples = 18
value = [14, 4]
Group 1
gini = 0.444
samples = 3
value = [1, 2]
Group 9
gini = 0.391
samples = 15
value = [4, 11]
gini = 0.0
samples = 1
value = [1, 0]
Ca
gini = 0.019
samples = 106
value = [105, 1]
Group 9
gini = 0.211
samples = 25
value = [22, 3]
Nd
gini = 0.105
samples = 18
value = [17, 1]
gini = 0.0
samples = 2
value = [0, 2]
La
gini = 0.375
samples = 4
value = [1, 3]
gini = 0.0
samples = 1
value = [1, 0]
gini = 0.0
samples = 12
value = [12, 0]
SiO2
gini = 0.5
samples = 2
value = [1, 1]
Nd
gini = 0.245
samples = 14
value = [12, 2]
Nd
gini = 0.5
samples = 4
value = [2, 2]
gini = 0.0
samples = 1
value = [1, 0]
gini = 0.0
samples = 2
value = [0, 2]
Eu
gini = 0.278
samples = 12
value = [2, 10]
Eu
gini = 0.444
samples = 3
value = [2, 1]
gini = 0.0
samples = 100
value = [100, 0]
La
gini = 0.278
samples = 6
value = [5, 1]
Ti
gini = 0.159
samples = 23
value = [21, 2]
V
gini = 0.5
samples = 2
value = [1, 1]
gini = 0.0
samples = 16
value = [16, 0]
Group 2
gini = 0.5
samples = 2
value = [1, 1]
gini = 0.0
samples = 3
value = [0, 3]
gini = 0.0
samples = 1
value = [1, 0]
gini = 0.0
samples = 1
value = [0, 1]
gini = 0.0
samples = 1
value = [1, 0]
Na
gini = 0.153
samples = 12
value = [11, 1]
Fe
gini = 0.5
samples = 2
value = [1, 1]
Fe
gini = 0.444
samples = 3
value = [1, 2]
gini = 0.0
samples = 1
value = [1, 0]
Sr
gini = 0.165
samples = 11
value = [1, 10]
gini = 0.0
samples = 1
value = [1, 0]
gini = 0.0
samples = 2
value = [2, 0]
gini = 0.0
samples = 1
value = [0, 1]
gini = 0.0
samples = 5
value = [5, 0]
gini = 0.0
samples = 1
value = [0, 1]
W
gini = 0.095
samples = 20
value = [19, 1]
Zr
gini = 0.444
samples = 3
value = [2, 1]
gini = 0.0
samples = 1
value = [0, 1]
gini = 0.0
samples = 1
value = [1, 0]
gini = 0.0
samples = 1
value = [0, 1]
gini = 0.0
samples = 1
value = [1, 0]
gini = 0.0
samples = 10
value = [10, 0]
Tb
gini = 0.5
samples = 2
value = [1, 1]
gini = 0.0
samples = 1
value = [1, 0]
gini = 0.0
samples = 1
value = [0, 1]
gini = 0.0
samples = 2
value = [0, 2]
gini = 0.0
samples = 1
value = [1, 0]
gini = 0.0
samples = 9
value = [0, 9]
Ba
gini = 0.5
samples = 2
value = [1, 1]
gini = 0.0
samples = 17
value = [17, 0]
Rare_earth
gini = 0.444
samples = 3
value = [2, 1]
gini = 0.0
samples = 2
value = [2, 0]
gini = 0.0
samples = 1
value = [0, 1]
gini = 0.0
samples = 1
value = [0, 1]
gini = 0.0
samples = 2
value = [2, 0]
gini = 0.0
samples = 1
value = [0, 1]
gini = 0.0
samples = 1
value = [1, 0]

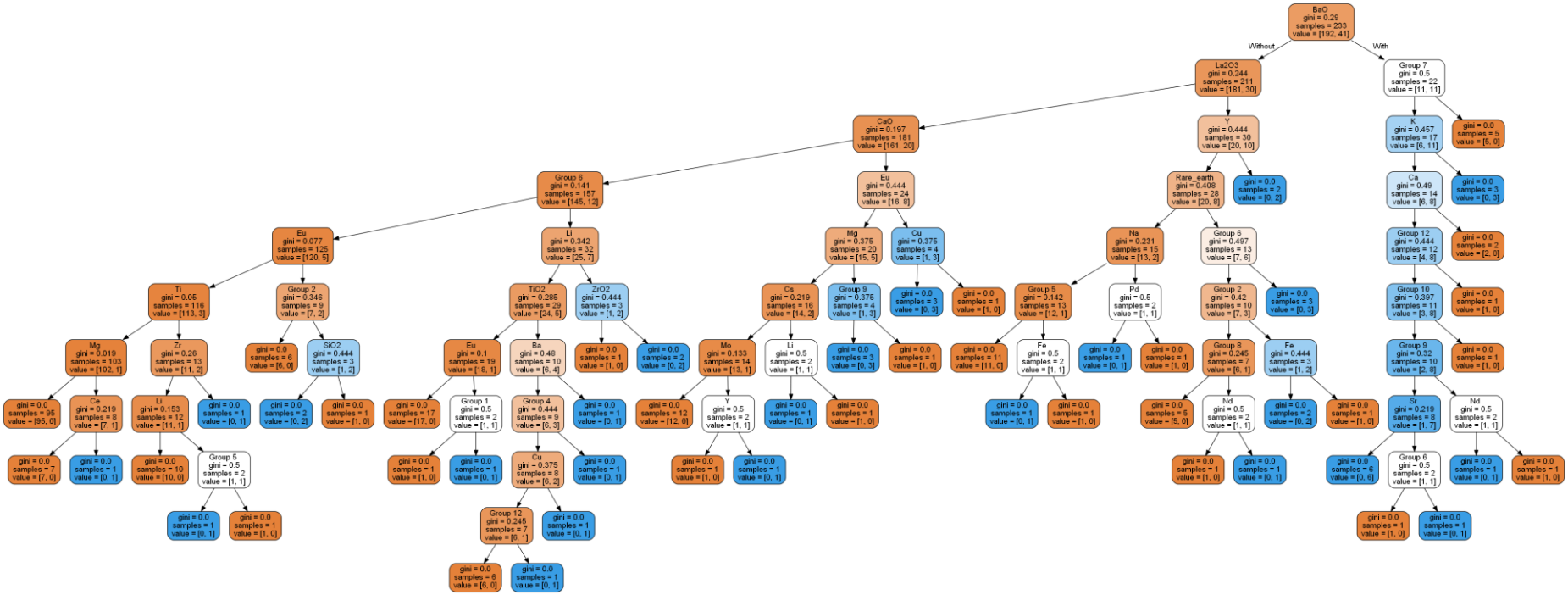

Figure 4.12. Decision tree generated from 233 catalysts which randomly selected from 291 catalysts with the same descriptors with Figure 4.11.

Left of a node indicates without/absence of an element, while right of a node indicates with/presence of an element.

The test set consisted of 20 % catalysts which were randomly selected from the 291 catalysts. In a typical procedure, catalyst descriptors like elements were labeled as a Boolean value for representing the absence/presence of specific elements in the composition. A full decision tree was created until all the leaves nodes were pure. Figure 4.10 showed the results of the decision tree with the accuracy of the train and test set equals to 1.00 and 0.74, which can derive some useful information. Decision tree suggested that supports (La_2O_3, BaO, CaO, TiO_2) were generally good support for OCM system (contributed to 32/39 cases of positive catalysts); if not, positive catalysts should contain at least one element which is rare-earth metal. In addition, by seeing the decision tree architecture, it can be seen the high occurrence of binary combination among group 1, 2, and rare earth metals such as La_2O_3-Ba, La_2O_3*Tb, BaO*K, CaO*Mg, La*Li, or MgO*Eu. The combination of among 1A, 2A, and rare earth metals could be confirmed by the literature which were reported elsewhere [27,36,39]. The presence of combination of group 6*group 1 for positive catalysts were also observed as Mo*Li and W*Cs (similar to to Na*W in Mn-Na-W/SiO_2) in the decision tree. Nevertheless, decision tree could propose only a few ternary positive combinations (such as La_2O_3*Tb*Hf, CaO*Mg*Sr). The reason of the limited knowledge extraction might come from the limited amount of samples compared to total possible sample which covers huge parametric space and the presence descriptors are currently not sufficient to describe the catalyst performance.

In order to overcome this shortcoming, using more effective descriptors is one of the ways to generalize the catalyst rules. It is known that elements belong in the similar group in periodic table exhibited the similar catalyst activity. Therefore, groups of M1-M3 elements were utilized as descriptor besides the absence/presence of

elements. The new decision tree was illustrated in the Figure 4.11. Figure 4.11 showed the decision tree with the same train and test data with the Figure 4.10, where the accuracy of train and test set could be achieved at 1.00 and 0.78, meaning that all the leave nodes are pure. By considering the detail of the tree structure, it could be seen that the tree structure is basically kept where positive catalysts should contain one these of supports (La_2O_3, CaO, BaO or TiO_2) or at least one rare-earth element in active components. Beside the similar between two tree models, it was interesting that the new decision tree showed shallower depth. The shallower tree depth while kept all the leave nodes are pure were the results of sophisticated descriptors. Some positive ternary descriptors could be found such as La_2O_3*group 2*group 1, La_2O_3*group 2*rare earth, La_2O_3*Rare earth*group 6, and TiO_2*group 4*rare earth. To validate the results which are derivated from decision tree in Figure 4.11, several decision trees were plotted in the Figure 4.12 with different training set to confirm the new findings. It is known that results from decision tree are sensitive to the choice of training set. By refer different decision tree results, such sensitive and unstable results could be avoid before reaching the final conclusion.

In literature, the decision tree has been utilized mainly for predicting the outcome of catalysis at different reaction conditions (temperature, contact time, reactant composition) and elemental composition (% mol) of only specific catalyst system by using literature data [40-43]. Hence, the application of machine learning model such as decision tree was applied for optimizing the performance of a specific type of catalyst, not for the dealing the. The reason is this problem may come from i) the limited sample numbers in literature data, ii) the bias sampling of literature between different catalyst systems, which results in the difficulty in correlating the catalyst performance and catalyst descriptors. As a natural consequence of random sampling, my dataset covers

a variety of catalyst compositions without anthropogenic biases. Such a dataset was proven to be useful in directly extracting knowledge of catalyst design through machine learning.

4.4. Conclusions

Synergistic combinations among multiple components are the key for designing performant solid catalysts. However, they are hard to be generalized, which is why the history of catalyst developments largely relied on an empirical try-and-error methodology and serendipitous findings therein. In this study, I attempted to derive a generalized guideline of catalyst design through: i) generation of 300 M1–M2–M3/Support catalysts based on random sampling of a huge materials space, ii) systematic evaluation of their performance in the oxidative coupling of methane (OCM) using a high-throughput screening (HTS) instrument, and iii) analysis of thus obtained catalyst big data. Major findings are summarized below.

- The analysis of the data distribution suggested that performant catalysts are able to retain high C_2 selectivity at a higher O_2 concentration and/or to activate CH_4 at a lower temperature.

- Among the evaluated 291 catalysts, 51 and 106 catalysts were classified into positive and negative catalysts, which noticeably improved and deteriorated the C_2 yield with respect to the non-catalytic free radical process. The positive and negative catalysts individually contained specific elements and supports at relatively high frequency. Among these, several elements had not been regarded as positive in literature. Novel performant catalysts were thus identified.

- It was evidenced that the catalyst performance was determined by the performance of constituent combinations, rather than the inclusion of specific elements or supports. It was also found that synergistic and antagonistic combinations individually contained combinations between specific elements and supports. The

rules of such combinations could be described based on the groups in the periodic table. This suggested general effectiveness of d^0 metallic salts.

- A guideline of combinatorial catalyst design was described based on the decision tree classification analysis. Positive catalyst should contains at one support among these support (La_2O_3, BaO, CaO, TiO_2), or contain at least one rare-earth element. Some positive ternary combination: La_2O_3*group 2*group 1, La_2O_3*group 2*rare earth, La_2O_3*Rare earth*group 6, and TiO_2*group 4*rare earth

- To the end, this study successfully demonstrated the power of bias-free catalyst big data in finding novel catalysts as well as a catalyst design guideline. It is also important to state the essentiality of high-throughput experimentation and data science approaches for implementing such a demanding study in a realistic timeframe. By equipping all the essential techniques of the study, truly non-empirical catalyst developments could be realized.

4.5. References

[1] E.-J. Ras, G. Rothenberg, Heterogeneous catalyst discovery using 21st century tools: a tutorial, RSC Adv., 4 (2014) 5963-5974.

[2] W.A. Herrmann, 100 years of metal carbonyls: a serendipitous chemical discovery of major scientific and industrial impact, J. Organomet. Chem., 383 (1990) 21-44.

[3] V. Busico, R. Pellecchia, F. Cutillo, R. Cipullo, High - Throughput Screening in Olefin - Polymerization Catalysis: From Serendipitous Discovery Towards Rational Understanding, Macromol. Rapid Commun., 30 (2009) 1697-1708.

[4] J.M. Venegas, W.P. McDermott, I. Hermans, Serendipity in catalysis research: boron-based materials for alkane oxidative dehydrogenation, Acc. Chem. Res., 51 (2018) 2556-2564.

[5] S. Huh, H.T. Chen, J.W. Wiench, M. Pruski, V.S.Y. Lin, Cooperative catalysis by general acid and base bifunctionalized mesoporous silica nanospheres, Angew. Chem., 117 (2005) 1860-1864.

[6] P. Chandra, A.M. Jonas, A.E. Fernandes, Spatial coordination of cooperativity in silica-supported Cu/TEMPO/Imidazole catalytic triad, ACS Catal., 8 (2018) 6006-6011.

[7] J.M. Notestein, A. Katz, Enhancing heterogeneous catalysis through cooperative hybrid organic–inorganic interfaces, Chem. Eur. J., 12 (2006) 3954-3965.

[8] A. Thakur, R. Baba, T. Wada, P. Chammingkwan, T. Taniike, Cooperative Catalysis by Multiple Active Centers of a Half-Titanocene Catalyst Integrated in Polymer Random Coils, ACS Catal., 9 (2019) 3648-3656.

[9] J.W. Thybaut, J. Sun, L. Olivier, A.C. Van Veen, C. Mirodatos, G.B. Marin, Catalyst design based on microkinetic models: Oxidative coupling of methane, Catal. Today, 159 (2011) 29-36.

[10] J. Sun, J.W. Thybaut, G.B. Marin, Microkinetics of methane oxidative coupling, Catal. Today, 137 (2008) 90-102.

[11] T. Kobayashi, T. Yamada, K. Kayano, Effect of basic metal additives on NOx reduction property of Pd-based three-way catalyst, Appl. Catal., B, 30 (2001) 287-292.

[12] C.-H. Tsai, H.-T. Chen, S.M. Althaus, K. Mao, T. Kobayashi, M. Pruski, V.S.Y. Lin, Rational catalyst design: a multifunctional mesoporous silica catalyst for shifting the reaction equilibrium by removal of byproduct, ACS Catal., 1 (2011) 729-732.

[13] T.P.N. Tran, A. Thakur, D.X. Trinh, A.T.N. Dao, T. Taniike, Design of Pd@ Graphene oxide framework nanocatalyst with improved activity and recyclability in Suzuki-Miyaura cross-coupling reaction, Appl. Catal., A, 549 (2018) 60-67.

[14] G. Kumar, E. Nikolla, S. Linic, J.W. Medlin, M.J. Janik, Multicomponent catalysts: limitations and prospects, ACS Catal., 8 (2018) 3202-3208.

[15] T. Taniike, M. Terano, Coadsorption model for first-principle description of roles of donors in heterogeneous Ziegler–Natta propylene polymerization, J. Catal., 293 (2012) 39-50.

[16] J.M. Thomas, Design, synthesis, and in situ characterization of new solid catalysts, Angew. Chem. Int. Ed., 38 (1999) 3588-3628.

[17] G.P. Szijjártó, Z. Pászti, I. Sajó, A. Erdőhelyi, G. Radnóczi, A. Tompos, Nature of the active sites in Ni/MgAl2O4-based catalysts designed for steam reforming of ethanol, J. Catal., 305 (2013) 290-306.

[18] J.C. Vedrine, Revisiting active sites in heterogeneous catalysis: Their structure and their dynamic behaviour, Appl. Catal., A, 474 (2014) 40-50.

[19] T. Taniike, T. Funako, M. Terano, Multilateral characterization for industrial Ziegler–Natta catalysts toward elucidation of structure–performance relationship, J. Catal., 311 (2014) 33-40.

[20] A. Thakur, T. Hamamoto, T. Ikeda, P. Chammingkwan, T. Wada, T. Taniike, Microwave-assisted polycondensation for screening of organically-modified TiO2/SiO2 catalysts, Appl. Catal., A, (2020) 117508.

[21] C.H. Wu, C. Liu, D. Su, H.L. Xin, H.-T. Fang, B. Eren, S. Zhang, C.B. Murray, M.B. Salmeron, Bimetallic synergy in cobalt–palladium nanocatalysts for CO oxidation, Nat. Catal., 2 (2019) 78-85.

[22] D.S. Mannel, M.S. Ahmed, T.W. Root, S.S. Stahl, Discovery of multicomponent heterogeneous catalysts via admixture screening: PdBiTe catalysts for aerobic oxidative esterification of primary alcohols, J. Am. Chem. Soc., 139 (2017) 1690-1698.

[23] G. P Szijjarto, A. Tompos, K. Héberger, J. L Margitfalvi, Synergism between constituents of multicomponent catalysts designed for ethanol steam reforming using partial least squares regression and artificial neural networks, Comb. Chem. High Throughput Screen., 15 (2012) 105-113.

[24] K. Takahashi, L. Takahashi, I. Miyazato, J. Fujima, Y. Tanaka, T. Uno, H. Satoh, K. Ohno, M. Nishida, K. Hirai, J. Ohyama, T.N. Nguyen, S. Nishimura, T. Taniike, The rise of catalyst informatics: Towards catalyst genomics, ChemCatChem, 11 (2019) 1146-1152.

[25] A. Galadima, O. Muraza, Revisiting the oxidative coupling of methane to ethylene in the golden period of shale gas: A review, J. Ind. Eng. Chem., 37 (2016) 1-13.

[26] B. Wang, S. Albarracín-Suazo, Y. Pagán-Torres, E. Nikolla, Advances in methane conversion processes, Catal. Today, 285 (2017) 147-158.

[27] U. Zavyalova, M. Holena, R. Schlögl, M. Baerns, Statistical analysis of past catalytic data on oxidative methane coupling for new insights into the composition of high-performance catalysts, ChemCatChem, 3 (2011) 1935-1947.

[28] R. Schmack, A. Friedrich, E.V. Kondratenko, J. Polte, A. Werwatz, R. Kraehnert, A meta-analysis of catalytic literature data reveals property-performance correlations for the OCM reaction, Nat. Commun., 10 (2019) 1-10.

[29] X. Jia, A. Lynch, Y. Huang, M. Danielson, I. Lang'at, A. Milder, A.E. Ruby, H. Wang, S.A. Friedler, A.J. Norquist, J. Schrier, Anthropogenic biases in chemical reaction data hinder exploratory inorganic synthesis, Nature, 573 (2019) 251-255.

[30] T.N. Nguyen, T.P.N. Tran, K. Takimoto, A. Thakur, S. Nishimura, J. Ohyama, I. Miyazato, L. Takahashi, J. Fujima, K. Takahashi, T. Taniike, High-Throughput Experimentation and Catalyst Informatics for Oxidative Coupling of Methane, ACS Catal., 10 (2020) 921-932.

[31] F. Pedregosa, G. Varoquaux, A. Gramfort, V. Michel, B. Thirion, O. Grisel, M. Blondel, P. Prettenhofer, R. Weiss, V. Dubourg, J. Vanderplas, A. Passos, D. Cournapeau, M. Brucher, M. Perrot, É. Duchesnay, Scikit-learn: Machine Learning in Python, J. Mach. Learn. Res., (2011) 2825−2830.

[32] C. Karakaya, H. Zhu, C. Loebick, J.G. Weissman, R.J. Kee, A detailed reaction mechanism for oxidative coupling of methane over $Mn/Na_2WO_4/SiO_2$ catalyst for non-isothermal conditions, Catal. Today, 312 (2018) 10-22.

[33] E.V. Kondratenko, M. Schlüter, M. Baerns, D. Linke, M. Holena, Developing catalytic materials for the oxidative coupling of methane through statistical analysis of literature data, Catal. Sci. Technol., 5 (2015) 1668-1677.

[34] V.I. Alexiadis, M. Chaar, A. van Veen, M. Muhler, J.W. Thybaut, G.B. Marin, Quantitative screening of an extended oxidative coupling of methane catalyst library, Appl. Catal., B, 199 (2016) 252-259.

[35] W. Liang, S. Sarsani, D. West, A. Mamedov, I. Lengyel, H. Perez, J. Lowrey, Performance improvement for a fixed-bed reactor with layered loading catalysts of different catalytic properties for oxidative coupling of methane, Catal. Today, 299 (2018) 60-66.

[36] D. Noon, B. Zohour, S. Senkan, Oxidative coupling of methane with La_2O_3–CeO_2 nanofiber fabrics: A reaction engineering study, J. Nat. Gas. Sci. Eng., 18 (2014) 406-411.

[37] E.V. Kondratenko, T. Peppel, D. Seeburg, V.A. Kondratenko, N. Kalevaru, A. Martin, S. Wohlrab, Methane conversion into different hydrocarbons or oxygenates: current status and future perspectives in catalyst development and reactor operation, Catal. Sci. Technol., 7 (2017) 366-381.

[38] L. Olivier, S. Haag, H. Pennemann, C. Hofmann, C. Mirodatos, A.C. van Veen, High-temperature parallel screening of catalysts for the oxidative coupling of methane, Catal. Today, 137 (2008) 80-89.

[39] B.L. Farrell, V.O. Igenegbai, S. Linic, A Viewpoint on Direct Methane Conversion to Ethane and Ethylene Using Oxidative Coupling on Solid Catalysts, ACS Catal., 6 (2016) 4340-4346.

[40] T. Williams, K. McCullough, J.A. Lauterbach, Enabling Catalyst Discovery through Machine Learning and High-Throughput Experimentation, Chem. Mater., 32 (2020) 157-165.

[41] Ç. Odabaşı, M.E. Günay, R. Yıldırım, Knowledge extraction for water gas shift reaction over noble metal catalysts from publications in the literature between 2002 and 2012, Int. J. Hydrog. Energy, 39 (2014) 5733-5746.

[42] M.E. Günay, R. Yildirim, Knowledge extraction from catalysis of the past: a case of selective CO oxidation over noble metal catalysts between 2000 and 2012, ChemCatChem, 5 (2013) 1395-1406.

[43] M.E. Günay, R. Yildirim, Modeling preferential CO oxidation over promoted Au/Al2O3 catalysts using decision trees and modular neural networks, Chem. Eng. Res. Des., 91 (2013) 874-882.

Chapter 5

General conclusion

Materials informatics is an emerging area of study, which utilizes data-driven approaches with the expectation to bring irreversible changes in the research and development of materials science. Even though many successful demonstrations of materials informatics have been recorded, the lack of a proper dataset is seen as the bottleneck of the implementation and breakthrough. While the literature data have been accumulated and ready to use, they suffer from an insufficient scale, non-uniformity, and anthropogenic biases towards good data with the burial of poor data. Moreover, materials properties such as catalyst performance are highly sensitive to process conditions, which can be varied from one literature to another literature. Therefore, efforts to establish a uniform and sufficient dataset have to be put in the first priority.

In **Chapter 2**, I reported an attempt of applying high-throughput experimentation towards the generation of catalyst big data for their usage in catalyst informatics using oxidative coupling of methane (OCM) as an example. I have successfully developed a high-throughput screening (HTS) instrument that automatically acquires 4320 data points for 20 separated catalysts per run in a process-consistent manner. From our obtained dataset, several visualization tools and machine learning techniques were applied to successfully extract knowledge from the obtained dataset. It was found that the OCM reaction is generally sensitive to the process conditions, and catalyst design has a great impact on the process dependence. In particular, the modification of Si-based support affects the performance of Mn-Na_2WO_4 in terms of the low-temperature activation of CH_4 and the selectivity tolerance against high O_2 concentration.

In order to explore the origin of the low-temperature CH_4 activation by the modification of Si-based supports, in **Chapter 3**, a series of Si-based supports differing

in the pore size, structure, and composition were employed to immobilize the Mn-Na-W active phase. The HTS instrument was utilized to evaluate the catalytic performance under various reaction conditions. It was found that supports of high Si contents were good supports in general, while specifically at low temperature, mesoporous Si-based supports appeared to be most effective. By a series of characterization, it was elucidated that a high Si content is advantageous in forming a cristobalite phase, which is known to stabilize tetrahedral WO_4^- active species, and the presence of mesopores is important for uniform dispersion of the active phase.

In **Chapter 4**, I demonstrated bias-free exploration of new OCM catalysts with the aid of random sampling from a huge materials space, HTS, and statistical analysis. Here, 300 M1-M2-M3/support catalysts were prepared and evaluated. Based on statistical analysis, I successfully identified individual elements and their binary combinations which are positive for the OCM performance. The results covered not only with the known catalysts obtained in the past three decades but also suggested new interactions which have never been reported.

I believe that the research works carried out in this thesis have clearly delivered the advantages of high-throughput experimentation and catalysts informatics for catalyst development. The same concept is widely applicable to many catalyst systems. Therefore, as a perspective, in the future, I would like to apply this new concept to other reaction to strengthen this concept. In this light, my thesis is expected to provide a new direction in the research and development of catalysts.

List of Publications and Other Achievements

Thanh Nhat Nguyen

A) PUBLICATION

1) **Thanh Nhat Nguyen**, Thuy Tran Phuong Nhat, Ken Takimoto, Ashutosh Thakur, Shun Nishimura, Junya Ohyama, Itsuki Miyazato, Lauren Takahashi, Jun Fujima, Keisuke Takahashi, Toshiaki Taniike, High-throughput experimentation and catalyst informatics for oxidative coupling of methane, ACS Catalysis, 2020, 10, 921–932.

2) Keisuke Takahashi, Lauren Takahashi, Itsuki Miyazato, Jun Fujima, Yuzuru Tanaka, Takeaki Uno, Hiroko Satoh, Koichi Ohno, Mayumi Nishida, Kenji Hirai, Junya Ohyama, **Thanh Nhat Nguyen**, Shun Nishimura, Toshiaki Taniike, The Rise of Catalyst Informatics: Towards Catalyst Genomics, ChemCatChem, 2019, 11, 1146–1152.

3) Thuy Phuong Nhat Tran, Ashutosh Thakur, **Thanh Nhat Nguyen**, Priyank Mohan, Toru Wada, Patchanee Chammingkwan, Toshiaki Taniike, Understanding chemiluminescence in catalytic oxidation of CO and hydrocarbons, *Catalysis Today*, 2020, doi.org/10.1016/j.cattod.2020.02.034

B) INTERNATIONAL CONFERENCE

1) Understanding the Thermal Degradation of Biobased Polyimide Derived from 4-Aminocinnamic Acid Photodimer, **Thanh Nhat Nguyen**, Tatsuo Kaneko, Toshiaki Taniike, Chemistry Conference for Young Scientists 2020 (CHEMCYS2020), Blankenberge, Belgium, Feb. 19-21, 2020, poster presentation.

2) High-Throughput Experimentation and Catalyst Informatics in Oxidative Coupling of Methane, **Thanh Nhat Nguyen**, Thuy Phuong Nhat Tran, Ashutosh Thakur, Shun Nishimura, Keisuke Takahashi, Toshiaki Taniike, Chemistry Conference for Young Scientists 2020 (CHEMCYS2020), Blankenberge, Belgium, Feb. 19-21, 2020, oral presentation.

2) High-Throughput Experimentation in Oxidative Coupling of Methane, **Thanh Nhat Nguyen**, Thuy Phuong Nhat Tran, Ashutosh Thakur, Shun Nishimura, Keisuke Takahashi, Toshiaki Taniike, The 8th Asia Pacific Congress on Catalysis (APCAT-8), Bangkok, Thailand, Aug. 4-7, 2019, poster presentation.

4) Thermal degradation and stabilization of bio-based polyimide, **Thanh Nhat Nguyen**, Anh Thi Ngoc Dao, Tatsuo Kaneko, Toshiaki Taniike, 10th International Conference of Modification, Degradation and Stabilization of Polymers (MoDeSt 2018), Tokyo, Japan, Sept. 2-6, 2018, poster presentation.

C) DOMESTIC CONFERENCE

1) Thermal degradation mechanism of bio-based polyimide derived from 4-aminocinnamic acid photodimer, **Thanh Nhat Nguyen**, Tatsuo Kaneko, Toshiaki Taniike, 令和元年度 エクセントコア「天然マテリアル」研究拠点シンポジウム, 第１１回サクラン研究会年次大会, 能美, 2019 年 10 月 25 日, ポスター

2) Insights into the thermo-oxidative degradation of bio-based polyimide derived from 4-aminocinnamic acid photodimer, **Thanh Nhat Nguyen**, Tatsuo Kaneko, Toshiaki Taniike, 第 8 回 JACI/GSC シンポジウム, 東京, 2019 年 6 月 24-25 日, ポスター.

3) Thermal degradation and stabilization of biobased polyimide from 4‐aminocinnamic acid photodimer, **Thanh Nhat Nguyen**, Tatsuo Kaneko, Toshiaki Taniike 平成 29 年度 日本化学会近畿支部 北陸地区講演会と研究発表会, 能美, 2017 年 12 月 1 日, ポスター

D) AWARD

Best Poster Presentation Award, "Understanding the Thermal Degradation of Biobased Polyimide Derived from 4-Aminocinnamic Acid Photodimer", **Thanh Nhat Nguyen**, Chemistry Conference for Young Scientists 2020 (CHEMCYS2020), Blankenberge, Belgium, **2/2020.**